

MECHANOCHEMICAL ACTIVATION OF SYNTHETIC NANOSIZED
2-D LAYERED MATERIALS: PREPARATION AND
CHARACTERIZATION

by

Abbas Fahami, B.S., M.S.

A thesis submitted to the Graduate Council of
Texas State University in partial fulfillment
of the requirements for the degree of
Doctor of Philosophy
with a Major in Materials Science, Engineering, and Commercialization
May 2017

Committee Members:

Gary W. Beall, Chair

Christopher P. Rhodes

Clois E. Powell

William Chittenden

Bahram Asiabanpour

COPYRIGHT

by

Abbas Fahami

2017

FAIR USE AND AUTHOR'S PERMISSION STATEMENT

Fair Use

This work is protected by the Copyright Laws of the United States (Public Law 94-553, section 107). Consistent with fair use as defined in the Copyright Laws, brief quotations from this material are allowed with proper acknowledgement. Use of this material for financial gain without the author's express written permission is not allowed.

Duplication Permission

As the copyright holder of this work I, Abbas Fahami, authorize duplication of this work, in whole or in part, for educational or scholarly purposes only.

DEDICATION

To my mentor, for his support and guidance along the way. To my parents, who love me unconditionally and consistently stressed the importance of education. To my amazing wife, who has been so supportive and has been my backbone throughout the journey, I cannot thank her enough.

ACKNOWLEDGEMENTS

I would like to express my deep appreciation to Dr. Gary W. Beall, the major professor and committee chairman, for his help, encouragement, unwavering support and invaluable guidance throughout the research. I would also like to acknowledge the precious help and assistance from Dr. Clois Powell, Dr. Christopher Rhodes, Dr. Bahram Asiabanpour, and Dr. William Chittenden as members of my committee.

TABLE OF CONTENTS

	Page
ACKNOWLEDGEMENTS	v
LIST OF TABLES	x
LIST OF FIGURES	xi
LIST OF ABBREVIATIONS.....	xv
ABSTRACT.....	xvi
CHAPTER	
1. INTRODUCTION	1
1.1.1. Anionic Clays.....	1
1.1.2. Cationic Clays.....	5
1.1.3. Mechanochemistry process.....	7
1.1.4. Outline.....	8
1.2. Characterization techniques.....	10
1.2.1. Phase analysis	10
1.2.2. Morphological characterization	10
1.2.3. Thermogravimetric analysis.....	10
2. HYDROTALCITE.....	11
2.1. Carbonate intercalated hydrotalcite	11
2.1.1. Materials and Experimental procedure	11
2.1.2. Results and discussions.....	12
2.1.2.1. XRD analysis	12
2.1.2.2. Microscopic Observation	14
2.1.3. Conclusions.....	17
2.2. Chloride intercalated hydrotalcite.....	19
2.2.1. Materials and Experimental procedure	19
2.2.2. Results and discussions.....	21
2.2.2.1. XRD analysis	21

2.2.2.2. Structural features	23
2.2.2.3. FT-IR analysis.....	26
2.2.2.4. Morphological characterization	27
2.2.2.5. Thermogravimetric analysis.....	29
2.2.3. Conclusions.....	30
2.3. Chloride intercalated hydrotalcite: mechanochemistry vs. hydrothermal	32
2.3.1. Materials and experimental procedure.....	32
2.3.1.1. Mechanochemistry method.....	32
2.3.1.2. Hydrothermal method	33
2.3.2. Result and discussion.....	34
2.3.2.1. XRD analysis	34
2.3.2.2. Morphological characterization	43
2.3.3. Conclusions.....	45
2.4. Sulfate intercalated hydrotalcite	46
2.4.1. Materials and experimental procedure.....	46
2.4.2. Result and discussion.....	47
2.4.2.1. XRD analysis	47
2.4.2.2. FT-IR analysis.....	49
2.4.2.3. Morphological characterization	50
2.4.2.4. Thermogravimetric analysis.....	51
2.4.3. Conclusions.....	52
3. HYDROCALUMITE.....	54
3.1. Experimental procedure.....	54
3.2. Result and discussion.....	57
3.2.1. XRD analysis	57
3.2.1.1. Effect of milling time.....	57
3.2.1.2. Effect of ion substitution.....	58
3.2.1.3. Rietveld Refinement	61
3.2.2. FTIR analysis	64
3.2.2.1. Effect of milling time.....	64
3.2.2.2. Effect of ion substitution.....	66
3.2.3. Morphological characterization	67
3.2.4. Thermogravimetric analysis.....	69
3.3. Conclusions.....	71

4. TALC	72
4.1. Experimental procedure	72
4.2. Result and Discussion	73
4.2.1. XRD analysis	73
4.2.2. FTIR analysis	76
4.2.3. Morphological characterization	79
4.2.4. Thermogravimetric analysis.....	83
4.3. Conclusions.....	85
5. PYROPHYLLITE – HALOYSITE	86
5.1. Experimental procedure	86
5.2. Result and Discussion	87
5.2.1. XRD analysis	87
5.2.2. FTIR analysis	89
5.2.3. Morphological characterization	90
5.2.4. Thermogravimetric analysis.....	94
5.3. Conclusions.....	95
6. MONTMORILLONITE	97
6.1. Experimental procedure	97
6.2. Result and Discussion	98
6.2.1. XRD analysis	98
6.2.2. FTIR analysis	101
6.2.3. Morphological characterization	102
6.2.4. Thermogravimetric analysis.....	105
6.3. Conclusions.....	107
7. HECTORITE	108
7.1. Experimental procedure	108
7.2. Result and Discussion	109
7.2.1. XRD analysis	109
7.2.2. FTIR analysis	111
7.2.3. Morphological characterization	112
7.2.4. Thermogravimetric analysis.....	116
7.3. Conclusions.....	118

8. SUMMARY	119
8.1. Future work	120
APPENDIX SECTION.....	121
REFERENCES	127

LIST OF TABLES

Table	Page
1. Chemical composition of Mg-Al-Cl-LDH obtained from XRF and EDS	29
2. Details of solution components.....	34
3. <i>R</i> factors obtained from the Rietveld refinement of Ca-Al-LDH	63

LIST OF FIGURES

Figures	Page
1. A representation of the Hydrotalcite structure.....	2
2. A representation of the Hydrocalumite structure.....	3
3. A representation of the Montmorillonite structure	6
4. A schematic view of the preparation of clays nanopowders.....	9
5. (a) XRD patterns of reaction 1 milled at different milling time, and (b) the patterns of reaction 2 milled at different milling time	13
6. Interlayer spacing of Mg-Al-CO ₃ -LDH prepared from reaction 1 (a) and 2 (b) as a function of milling time	14
7. (a) FESEM images of 180 min milled Mg-Al-CO ₃ -LDH obtained from reaction 1 (R1), and (b) 60 min milled sample from reaction 2 (R2)	16
8. (a) TEM images of 180 min milled Mg-Al-CO ₃ -LDH prepared from reaction 1 (R1), and (b) 60 min milled sample from reaction 2 (R2)	16
9. (a) EDS spectra of 180 min milled Mg-Al-CO ₃ -LDH obtained from reaction 1 (R1), and (b) 60 min milled sample from reaction 2 (R2)	17
10. XRD profiles of samples as function of milling time before (a) and after (b) washing with deionized water followed by drying	22
11. XRD patterns along with the magnified region between $2\theta = 7^\circ$ to 25° of Mg-Al-CO ₃ -LDH and Mg-Al-Cl-LDH samples milled for 5h.....	23
12. (a) crystallite size, lattice strain, and (b) crystallinity degree of samples (Mg-Al-Cl-LDH) as a variation of milling time.....	24
13. (a) Interlayer spacing, (c) lattice constants, and (d) unit cell volume of specimens (Mg-Al-Cl-LDH) as a function of milling time.....	25
14. FT-IR spectra of specimens (Mg-Al-Cl-LDH) as a variation of milling time.....	27

15. Morphological features of 5h milled sample (Mg-Al-Cl-LDH): (a) low, (b) high magnification FE–SEM images and (c) TEM image.....	28
16. EDS and elemental mapping analysis of 5h milled sample (Mg-Al-Cl-LDH).....	29
17. DTGA of 5h milled sample (Mg-Al-Cl-LDH) as a function of temperature	30
18. XRD profiles of samples as a function of ion contents degree (X) prepared by Hydrothermal (a) and Mechanochemistry methods (b)	35
19. XRD profiles along with the magnified regions between $2\theta = 7^{\circ}$ – 25° for samples prepared by Hydrothermal (a) and Mechanochemistry methods (b)	36
20. Crystallite size, and lattice strain of samples prepared by Hydrothermal (a) and Mechanochemistry methods (b) as a variation of different ion contents (X)	38
21. FWHM of milled (M) and hydrothermally (H) treated samples at three different ion contents (X): (a) X=0.18, (b) X=0.3, and (c) X=0.42.....	39
22. Crystallinity degree of samples prepared by Hydrothermal (H), and Mechanochemistry (M) methods as a variation of ion contents (X)	40
23. lattice constants of hydrothermal specimens (a), mechanochemical samples (b), and Unit cell volume of specimens (c) prepared by Hydrothermal (H), and Mechanochemistry (M) methods as a variation of ion contents (X)	41
24. Interlayer spacing of specimens prepared by Hydrothermal (H), and Mechanochemistry (M) methods as a function of ion contents degree(X).....	42
25. (a,b) FESEM and (c) TEM images of hydrothermal sample (H2), (d,e) FESEM and (f) TEM images of milled sample (M2).....	42
26. EDS spectra of (a) hydrothermal sample (H2), and (b) milled sample (M2)	44
27. (a) XRD patterns, (b) interlayer spacing, (c) lattice parameters and (d) the unit cell volume of the milled samples as a function of milling time (30-900 min).....	48
28. FT-IR spectra of milled specimens (Mg-Al-SO ₄ -LDH) as a variation of milling time; (a) 30, (b) 60, (c) 300, (d) 600, and (e) 900 min.....	50

29. Morphological features of 60 min milled sample (Mg-Al-SO ₄ -LDH): (a) FE–SEM image & EDS spectrum and (b) TEM image.....	51
30. DTGA of 60 min milled sample as a function of temperature	52
31. XRD patterns of specimens (Ca-Al-LDH) milled at different milling time (30=S1, 60=S2, 180=S3, and 300=S4).....	56
32. The magnified 3D XRD profiles ($2\theta = 5-35$) of samples (S1, S2, S3, and S4).....	57
33. The interlayer spacing of specimens (Ca-Al-LDH) milled at different milling time (S1, S2, S3, and S4)	58
34. XRD patterns of Ca-Al-LDH with various ion substitutions (S1=0.1, S2=0.15, S3=0.2, S4=0.25, S5=0.3, S6=0.35, and S7=0.4).....	59
35. The interlayer spacing of Ca-Al-LDH as function of ion substitutions.....	61
36. Rietveld refinement plots of Ca-Al-LDH as function of ion substitutions.....	62
37. The refined lattice constants (a) and unit cell volumes (b) of Ca-Al-LDH as a variation of ion substitution	64
38. FT-IR spectra of milled specimens (S1, S2, S3, and S4).....	65
39. FT-IR spectra of Ca-Al-LDH as variation of ion substitutions (S11=0.1, S22=0.15, S33=0.2, S44=0.25, S55=0.3, S66=0.35, and S77=0.4).....	66
40. Morphological features and chemical composition of 60 min milled sample (Ca-Al-LDH): (a) FE–SEM, (b) TEM images	68
41. The elemental mapping analysis of 60 min milled sample (Ca-Al-LDH).....	69
42. DTGA of 60 min milled sample (Ca-Al-LDH) as a function of temperature	70
43. XRD patterns of the 10h milled mixtures with (wet) and without water (dry).....	74
44. XRD patterns of the mixtures as a function of milling time: T1 (0.5h), T2 (1h), T3 (5h), and T4 (10h).....	75

45. XRD patterns of the different milled powders followed by autoclave treatment mixtures at 260°C for 12h: T11 (0.5h), T22 (1h), T33 (5h), and T44 (10h)	75
46. The FT-IR spectra of samples as a variation of milling time (T1:1h, T2:5h, and T3:10h).....	78
47. FTIR spectra of the different milled powders followed by autoclave treatment mixtures at 260°C for 12h: T11 (0.5h), T22 (1h), T33 (5h), and T44 (10h)	79
48. FESEM image of sample milled for 5h	80
49. FESEM images of talc produced after 5h milling and subsequent autoclave treatment at 260°C for 12h (T33).....	81
50. TEM micrograph of talc prepared after 5h milling and following autoclave treatment at 260°C for 12h (T33).....	82
51. EDS spectrum of talc produced after 5h milling and following autoclave treatment at 260°C for 12h (T33)	83
52. DTGA graph of 5h milled sample followed by autoclave treatment at 260°C for 12h (T33)	84
53. XRD patterns: Pyrophyllite; MC (K1), autoclave assisted MC (K3), Halosite; MC (K2), autoclave assisted MC (K4)	88
54. FTIR spectra of PP (K3) and HS (K4) samples milled for 5h followed by autoclave treatment for 24h at 260 °C.....	89
55. FESEM images of K3 milled for 5h and autoclave treated for 24h at 260°C	91
56. TEM image of K3 milled for 5h and autoclave treated for 24h at 260°C	92
57. FESEM images of K4 milled for 5h and autoclave treated for 24h at 260°C	93
58. TEM image of K4 milled for 5h and autoclave treated for 24h at 260°C	93
59. DTGA of K3 milled for 5h followed by autoclave treatment for 24h at 260 °C.....	94
60. DTGA of K4 milled for 5h followed by autoclave treatment for 24h at 260 °C.....	95

61. XRD patterns of the mixtures grounded for two milling times (5 and 10h).....	99
62. XRD patterns of autoclaved powders as a variation of time: 24h (M1), 48h (M2), 72h (M30), and 96h (M4)	100
63. FTIR spectra of MMT milled for 10h followed by autoclave treatment at 260° for different times: 24h (M1), 48h (M2), 72h (M30), and 96h (M4)	101
64. FESEM images of MMT (M3) produced after 10h milling and subsequent autoclave treatment at 260°C for 72h.....	103
65. TEM images of MMT (M3) prepared after 10h milling and subsequent autoclave treatment at 260°C for 72h.....	104
66. EDS spectrum of MMT (M3) produced after 10h milling and subsequent autoclave treatment at 260°C for 72h.....	105
67. DTGA curve of sample milled for 10h and followed by autoclave treatment for 72h at 260 °C (M33)	106
68. XRD profiles of the mixtures grounded for two milling times: (H1:5h, and H2:10h), and the autoclaved samples as a function of time: (24h:H3, and 48h:H4)	110
69. FTIR spectra of powders milled for 10h (H2), and subsequent autoclave treatment on the milled sample for two different times (H3:24h, and H4:48h).....	112
70. FESEM images of HEC (H4) prepared after 10h milling and subsequent autoclave treatment for 48h.....	113
71. TEM image of HEC prepared after 10h milling and subsequent autoclave treatment for 48h (H4)	114
72. EDS spectrum of HEC prepared after 10h milling and subsequent autoclave treatment for 48h (H4)	115
73. DTGA curve of sample milled for 10h (H2)	116
74. DTGA graph of sample milled for 10h followed by subsequent autoclave treatment for 48h (H4)	117

LIST OF ABBREVIATIONS

Abbreviation	Description
HT	Hydrotalcite
HC	Hydrocalumite
PP	Pyrophyllite
HS	Halosite
KAO	Kaolinite
MMT	Montmorillonite
HEC	Hectorite
LDH	layered double hydroxides
MC	Mechanochemistry
MA	Mechanical Alloying
HTI	Hydrothermal
XRD	X-ray diffraction
FT-IR	Fourier Transform Infrared spectroscopy
FESEM	Field emission scanning electron microscopy
EDS	Energy dispersive spectroscopy
EMA	Elemental mapping analysis
TEM	Transmission electron microscopy
XRF	X-ray fluorescence
DTGA	Differential thermogravimetric analysis

ABSTRACT

The clay materials provide a 2-D lamellar structure with a myriad of applications in medicine, water treatment, catalysis, and biochemistry. They are utilized for the development of organic and/or inorganic-clay nanocomposites due to high cation exchange capacity, swelling behaviour, adsorption and large surface area. The surface can be chemically and physically modified to suit technological needs. Various ionic clay minerals such as Hydrotalcite (HT: $Mg_{1-x}Al_x(OH)_2Cl_x$), Hydrocalumite (HC: $Ca_{1-x}Al_x(OH)_2Cl_x$), Talc ($Mg_3Si_4O_{10}(OH)_2$), Pyrophyllite (PP: $Al_2Si_4O_{10}(OH)_2$), Halloysite (HS: $Al_2Si_2O_5(OH)_4$), Montmorillonite (MMT: $Al_{2-x}Mg_xSi_4O_{10}(OH)_2Na_x$), and Hectorite (HEC: $Mg_{3-x}Li_xSi_4O_{10}(OH)_2Na_x$) can be synthesized utilizing hydrothermal procedures. This synthesis method is tedious, time consuming, expensive, energy-intensive, and dangerous due to the high temperatures and pressures required. In the synthesis of clay minerals precursor compounds are dissolved in water and precipitated as amorphous gels. Subsequent hydrothermal treatment produces the desired clay mineral. This process involves bond breaking by the solvent and then reformation through hydrothermal treatment. The hypothesis in this project is based on breaking the bonding of reagents and reforming a new clay material through a facile solid state method rather than through solvents. The ultimate objective of this research is synthesis of these materials via mechanochemical means, study structural features, morphological characterization, and thermal behavior of products as a function of synthesis conditions (e.g. the effect of ion substitution and synthesis parameters on the porosity and textural characteristics of

synthetic clays). Mechanochemistry is the combination of mechanical and chemical phenomena which is complex and different from thermal or photochemical mechanisms. In this project, we successfully prepared anionic clays (e.g. HT, and HC), non-ionic (e.g. Talc and PP), and cationic clays (e.g. MMT, and HEC) through the mechanochemistry method. The subsequent autoclaving process on the non-ionic and cationic samples were studied. The structural features and morphological characteristics of milled samples were analyzed and characterized by X-ray diffraction (XRD), Fourier Transform Infrared spectroscopy (FT-IR), field emission scanning electron microscopy (FESEM), energy dispersive spectroscopy (EDS), elemental mapping analysis, transmission electron microscopy (TEM), X-ray fluorescence (XRF), and differential thermogravimetric analysis (DTGA). The results presented in this dissertation provided a plethora of new information that challenge old dogmas. One of the main contributions of this study was to demonstrate, for the first time, that many smectite clays can be synthesized via a one step, wet mechanochemistry process.

1. INTRODUCTION

Clay minerals with a 2-D lamellar structure are categorized by two main ionic lamellar solids as a function of ion exchange properties: the anionic clays (e.g. HT and HC) and cationic clays (e.g. MMT, and HEC). These materials are composed of charged layers and charge compensating ions within the interlayer or gallery region [1]. Clays like Talc, Kaolinite, Serpentine, Chlorite, Pyrophyllite, and Illite are considered as non-ionic clays due to the lack of ion exchange capacity.

1.1.1. Anionic Clays

The anionic clays or layered double hydroxides (LDH) with general formula of $[M_{(1-x)}^{2+}M_x^{3+}(OH)_2]^{x+}[A_{x/n}^{n-}].mH_2O$ contain positively charged layers, which are the result of the isomorphous substitution of M^{2+} ions by M^{3+} ions [2]. The dominant divalent cations, M^{2+} , are Mg^{2+} , Ca^{2+} , Mn^{2+} , Fe^{2+} , Ni^{2+} , Cu^{2+} and Zn^{2+} , and the dominant trivalent cations, M^{3+} , are Al^{3+} , Mn^{3+} , Fe^{3+} , Co^{3+} and Ni^{3+} . The most common intercalated anions are CO_3^{2-} , Cl^- , SO_4^{2-} , OH^- or NO_3^- , together with water molecules, occupy the interlayer space [3]. Fig. 1 shows a representation of the hydrotalcite structure. Synthetic ionic clays with the HT structure have a combination of Mg^{2+} or Al^{3+} cations, and CO_3^{2-} anion such as the $Mg_{0.8}Al_{0.2}(OH)_2(CO_3)_{0.1}$. Other forms of HT are known as chloride form ($Mg_{0.8}Al_{0.2}(OH)_2(Cl)_{0.2}$), and sulfate form ($Mg_{0.8}Al_{0.2}(OH)_2(SO_4)_{0.1}$). The carbonate ion due to a higher affinity in the HT interlayer, is easily trapped in LDH as soon as it is exposed to air and moisture. This form of HT is utilized as CO_2 absorbents, ion exchangers, fire retardants, and base catalysts [4].

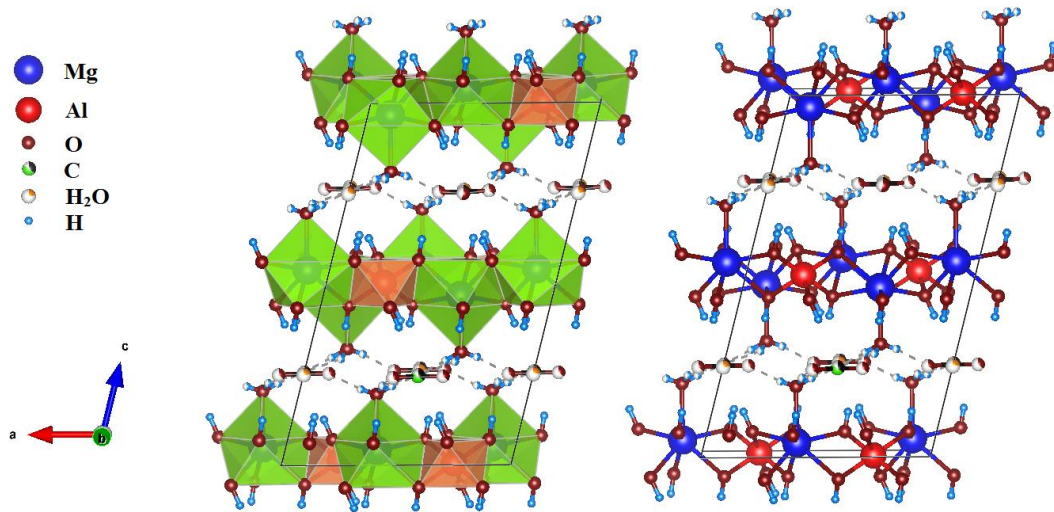


Fig. 1 A representation of the Hydrotalcite structure

Hydrocalumite (HC) are anionic clays with the chemical formula of $\text{Ca}_{1-x}\text{Al}_x(\text{OH})_2 \text{A}^{n-}_x$, where A^{n-} represents the charge balancing anions such as CO_3^{2-} , Cl^- , SO_4^{2-} , OH^- , $\text{Al}(\text{OH})_4^-$ or NO_3^- [2]. HC also belong to the family of layered double hydroxides (LDH) different from Hydrotalcites. Their main layer has well-ordered Ca/Al distribution in the hydroxide layers due to the large cationic radius of Ca^{2+} in comparison to Mg^{2+} . The water and anions are placed in the interlayer spaces (see Fig. 2) [5]. Some anions are preferentially intercalated with LDH. They may be used for targeted anion removal in for environmental protection [6]. The carbonate ion because of its high affinity is preferably the intercalated anion in HC structure, which is easily trapped in LDH [7]. The presence of the carbonate in the interlayer region significantly affects the chemical reactivity of the LDH. Yoon et al. [8] reported that calcined layered double hydroxide is an effective absorbent for chloride ions in cement. Linares et al. [9] demonstrated that carbonated hydrocalumite can be used as an antacid using a synthetic gastric juice.

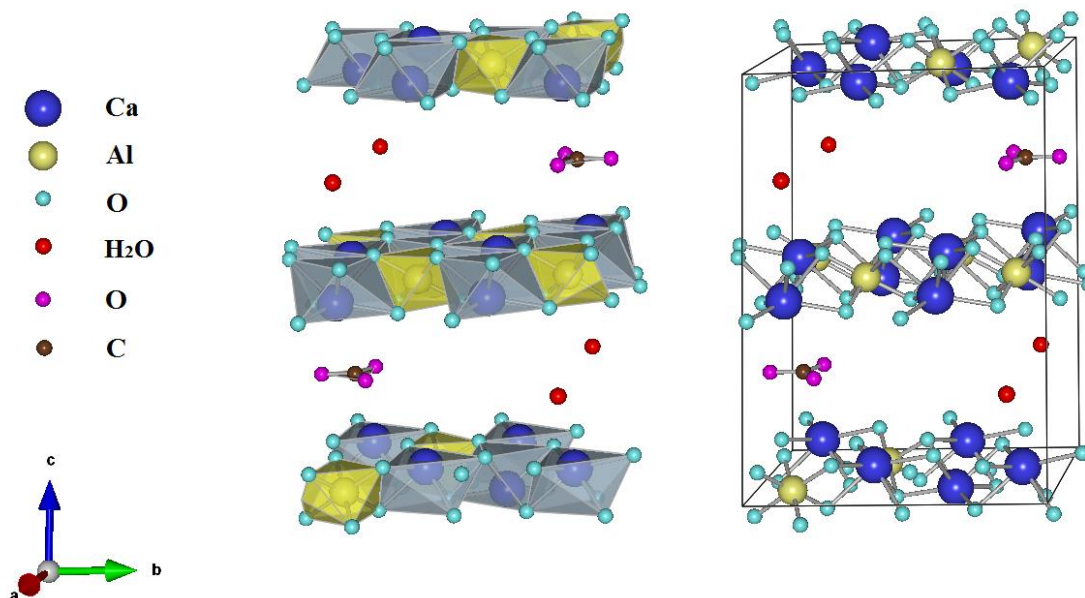


Fig. 2 A representation of the Hydrocalumite structure.

HC has industrial and environmental applications for mopping up of oil from oil-water mixtures [10], the removal of environmental hazards in acid mine drainage [11], and the disposal of radioactive wastes [12]. Chloride intercalated HC efficiently removes nitrate from water because chloride in HC can be easily exchanged for nitrate. Chloride HC can form other types of Ca-Al-LDH [13].

Many different chemical methods have been employed for the fabrication of anionic clays. These methods include co-precipitation at different pHs for the removal of heavy metal [14], hydrolysis [15], sol-gel [16], Microwave-assisted structure reconstruction which help the crystalline growth of HC [17], hydrothermal [18], and sonication [19]. Mechanochemistry (MC) is a solvent-free process that has attracted special attention as a method to prepare commercially nanostructured materials with proper structural characteristics due to its simplicity and versatility. The information regarding the preparation of clay materials through this process is limited [20]. MC is a

broadly used process in which mechanical force is used to achieve chemical processing and transformations [21]. In MC process, melting is not necessarily occurring. A homogenous product with nanostructural features is produced from blended reagents mixture [22, 23]. In terms of environmental and topochemical viewpoints, the reactions between solid reactants without a solvent are essential. Large amounts of solutions can be eliminated. Noxious gases emissions and the release of wastewater can be avoided with the solvent-free MC method [24]. The mass production of LDH with MC processing is promising.

A limited number of experiments have been reported involving the intercalation of different anions into the interlayer LDH via MC method. Isupov *et al.* [25] reported the formation of Mg-Al-LDHs by mixing magnesium hydroxide with aluminum nitrate, sulfate, and chloride with a high-energy ball mill. Khusnutdinov *et al.* [26] obtained the hydroxycarbonate form of HT with a mechanical Alloying (MA) process. The synthesis of Zn-Al-LDHs through grinding followed by autoclaving the solid precursors at 150 °C for 1 day was investigated by Chitrakar *et al.* [27]. New LDHs such as Li-Al [28], and Ca-Sn [29] LDH were prepared by the MA method. Ferencz *et al.* [30] prepared Ca-Al-CO₃-LDH using calcium hydroxide and aluminum hydroxide by a two-step MA process with some impurities (15.6 wt.% Katoite) in the final product. Note that Ca-Al-LDH was initially formed as a metastable compound in cement and converted to cubic Katoite (Ca₃Al₂(OH)₁₂) as a stable calcium aluminate hydrate during concrete curing [31]. Qu *et al.* [32] was also reported two steps mechanochemically induced Ca-Al-CO₃-LDH. Their initial results demonstrated that the milling of hydroxides gave Katoite but no LDH phase. Calcium chloride and calcium carbonate were added to their mixture. The addition

of a third phase to Ca and Al hydroxides allowed the easy formation of stable Ca–Al–LDH phases.

1.1.2. Cationic Clays

The cationic clays such as MMT and HEC form an important group of the phyllosilicate family (layered structures) of clay minerals. They are composed of polymeric sheets of SiO₄ tetrahedra linked to sheets of (Al, Mg, Fe) (O, OH)₆ octahedra [33]. The charge deficit of the negatively charged layers is compensated by interlamellar cations that are usually hydrated [34]. These clays are ubiquitous in soils, sediments, and widespread in nature. They are difficult to synthesized [35]. The high specific surfaces, and ion-exchange properties results in a wide range of industrial applications in ceramics, nanocomposites, medicine, catalysis, and biochemistry [33]. The cationic clays are used to develop polymer-clay nanocomposites that are chemically and physically modified to suit practical technological needs. The characteristics of clay make it ideal for the delivery of genes to a target cell for gene therapy [36]. They stable, non-toxic nature, and tightly adsorb and protect biomolecules from enzyme and photocatabolic degradation. MMT and Hectorite are essential for the development of new therapeutic techniques for the healthcare sector [37].

Natural MMT has average porous size (nanoporous) of about 15 Å (1.5 nm) [38]. In the crystal structure of MMT, some of the atoms of Al are replaced by Mg, lithium (Li) or iron (Fe) by isomorphic substitution. The negative charge on the surface of the sheet layer is offset by exchangeable metal cations residing in the interlayer space, such

as sodium (Na), and calcium (Ca) [37]. A representation of the MMT structure is presented in Fig. 3.

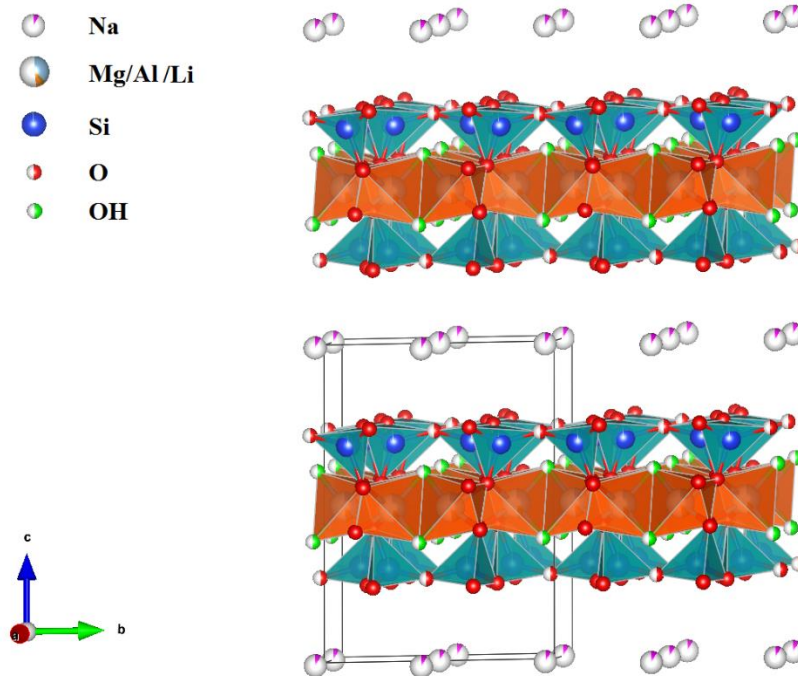


Fig. 3 A representation of the Montmorillonite structure

The basic structural unit of hectorite has two tetrahedral SiO_2 layers that sandwich and condensed to a central magnesium oxide octahedral layer. Cation exchange capacity arises from isomorphous substitutions of Li^{+1} for Mg^{+2} in the octahedral layer. Synthetic hectorite (Laponite) has high viscosity and transparency in water with all the benefits mentioned for cationic clays [39].

In natural clays, moderate amounts of cations (e.g., Fe, Ni, Mn) can occupy the octahedral sites. Small amounts of Al, Cr and Ti may replace for Si [40]. The presence of foreign ions (i.e., Fe, Ni, Al, etc.) in natural clays in inconsistent amounts may inhibit the performance of these minerals. The synthesis and characterization of synthetic cationic

clays is an important subject [41]. Variables such as composition, purity, reproducibility, and specifically designed features can be controlled without using natural clay specimens [33]. Questions related to formation and stability are best answered by a study of synthetic, fully characterized, single-phase specimens.

Scientists demonstrated that various clay minerals (e.g. Talc [41], MMT [42], and Hectorite [43]) can be synthesized utilizing hydrothermal process. Synthetic MMT requires temperatures, in the 300–400 °C range. Autogenous pressure conditions to afford the best purity and crystallinity in reasonable timeframes. Hectorite forms at low temperatures and pressures in nature. It is amenable to crystallization under much less rigorous conditions [39]. Hydrothermal processing is tedious, expensive, energy-intensive, and dangerous due to the high temperatures and pressures required.

1.1.3. Mechanochemistry process

Mechanochemistry (MC) is the ball milling of powders with different compositions that results in changes in the structure or microstructure. This method is a broadly used method in which mechanical force is utilized to achieve transformations and chemical processing. Melting is not necessarily occurring in this process and a homogenous product with nanostructural features is produced from grounded precursors mixture [23]. The mechanism for MC of clay materials involve first forming a lamellar structure, that on continued milling, become finer and finer, and finally alloying occurs via diffusion. In some cases, amorphization mechanism is predominant which involves the transformation from the crystalline to the amorphous state in single component materials. The amorphization by MC might also affected by the defects produced by the

deformation of ball milling [44]. It has been demonstrated that the defects introduced into the crystalline materials by the deformation of ball milling rise the Gibbs free energy of the crystalline state to that of the amorphous state, thus promoting the transformation.

1.1.4. Outline

The present dissertation describes the synthesis of anionic clays like HT and HC with different degrees of anion substitution via mechanochemical activation procedures. Various forms of HT and HC with chloride, nitrate, and sulfate counter ions are expected to be better anionic clays for industrial and environmental applications when compared to the carbonate form.

The second objective of this project is the synthesis of non-ionic and cationic clays via mechanochemical processing. A study of synthesis conditions on the structural characterization is included. To the best of our knowledge, this is first synthesis of cationic clay minerals through the MC method. The first step was to prepare Talc and PP, which have similar layered structures with MMT, and HC, respectively. Next, the preparation of MMT and HEC was conducted via MC processing. Autoclaving was employed to obtain high crystalline smectite clays. [Fig. 4](#) displays a schematic view of the preparation of anionic, non-ionic, and cationic clays nanopowders in this research. These 2-D layered materials have significant potential for environmental and industrial applications.

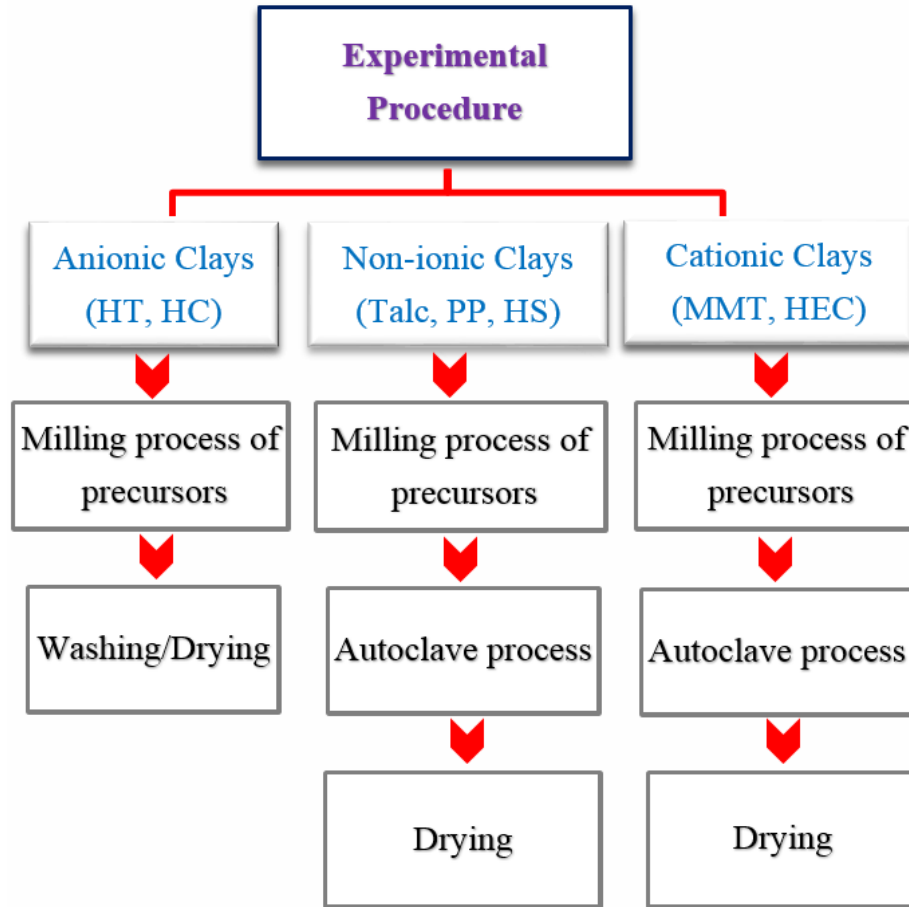


Fig. 4 A schematic view of the preparation of clays nanopowders.

1.2. Characterization techniques

1.2.1. Phase analysis

Phase identification was carried out on a Bruker D8 Advance ECO using $Cu-K_{\alpha}$ radiation ($\lambda \approx 1.54\text{\AA}$). The patterns were scanned in different ranges mostly from 5 to 80 degrees 2θ with a step size of 0.03 degrees. The XRD profiles were compared to standards compiled by the Joint Committee on Powder Diffraction and Standards (JCPDS). The functional groups and structural changes of the samples were carried out by Fourier transform infrared spectroscopy (FT-IR, Bruker Tensor 27, USA). All spectra were recorded at ambient temperature in the range $4000\text{--}400\text{ cm}^{-1}$.

1.2.2. Morphological characterization

The morphological features of the milled specimens were characterized using FESEM (FEI Helios Nanolab 400 SEM). A more detailed morphological analysis was also executed using TEM (JEOL JEM 1200 EXII) that operated at the acceleration voltage of 120 kV. EDS and elemental mapping analysis attached to the FESEM was used to determine the elemental composition and distribution of components. The elemental analysis of powders was determined using the Supermini 200 (Rigaku) X-ray fluorescence (XRF) analyzer.

1.2.3. Thermogravimetric analysis

Thermal analysis was performed with a TGA (TA Q50 Thermogravimetric Analyzer) in an argon atmosphere at a rate of $10^{\circ}\text{C}/\text{min}$ from room temperature to 800°C .

2. HYDROTALCITE

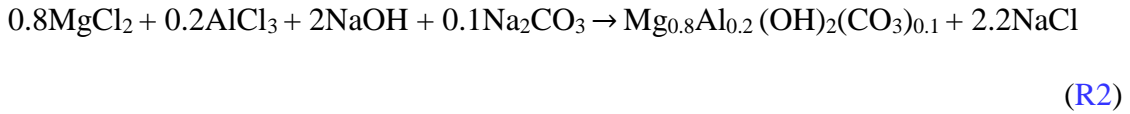
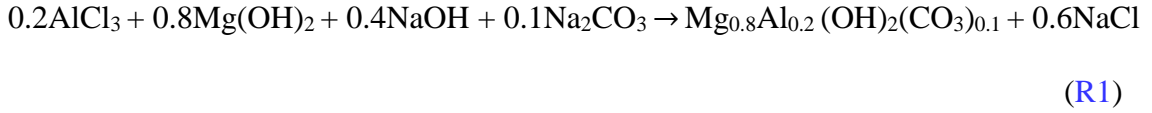
2.1. Carbonate intercalated hydrotalcite

Carbonate intercalated Mg-Al layered double hydroxides (Mg-Al-CO₃-LDH) were successfully produced by the MC process using different starting raw chemicals. Two distinct chemical reactions were activated at different milling times. The samples were characterized by XRD, FESEM, EDS, and TEM. The structural characteristics of Mg-Al-CO₃-LDH were affected strongly by milling time. Based on the XRD data, the formation of pure HT was strongly influenced by the chemical composition of raw materials. Electron microscopic observations determined that the final product had a platelet-like structure with an average particle size of 20-100 nm. The synthesis of Mg-Al-CO₃-LDH is a cost-effective solid-state method owing to simplicity and reproducibility. This is a promising candidate for use in catalyst industries.

2.1.1. Materials and Experimental procedure

Magnesium hydroxide (99%, Sigma-Aldrich), Magnesium chloride (99%, ACROS), Sodium carbonate (99%, Sigma-Aldrich), Aluminum chloride (99 %, ACROS), and Sodium hydroxide pellets (97%, ACROS) were purchased and milled using high energy ball mill (8000M Mixer/Mill) under air atmosphere. The mechanochemical activation was done in a hardened chromium steel vials (vol. 65 ml) using steel balls (13 mm in diameter) for 14, 30, 60, 180, 300, 600 min. The weight ratio of ball-to-powder (BPR) and vibrational speeds were 10:1 and 1750 RPM, respectively. To investigate the effect of chemical composition of raw materials on the mechanically

induced HT and purity of final products, two distinct chemical reactions were utilized as follows:



The mole ratio of magnesium to aluminum was equal 4, and the substitution degree of CO_3^{2-} was chosen equal 0.1. The mechanically activated powders were washed three times with deionized water (20 ml) on a paper filter, and then were dried under oven at 80°C for 1h.

2.1.2. Results and discussions

2.1.2.1. XRD analysis

Fig. 5 presents XRD patterns of reaction 1 (R1) and reaction 2 (R2) samples milled at different milling times, which have been compared with standard diffraction patterns. Hydrotalcite is indicated by the lettered peaks (HT). Based on Fig. 5a, the main products of 60 min milling run were Brucite and HT. The mechanochemical reaction to produce HT was not completed in this time frame. Brucite completely vanishes with increasing of milling time to 180 min. A pure phase composition of carbonated intercalated HT was formed. This trend continued up to 300 min when a partial trace of Periclase (MgO) appeared. HT decomposed slightly as the milling time increased. The intensity of main peaks for the 180 min milled sample decreased gradually as the milling

time increased. The proper crystalline structure was formed at 180 min milling time.

Mechanically induced Mg-Al-CO₃-LDH synthesis was affected by milling time (60-300 min).

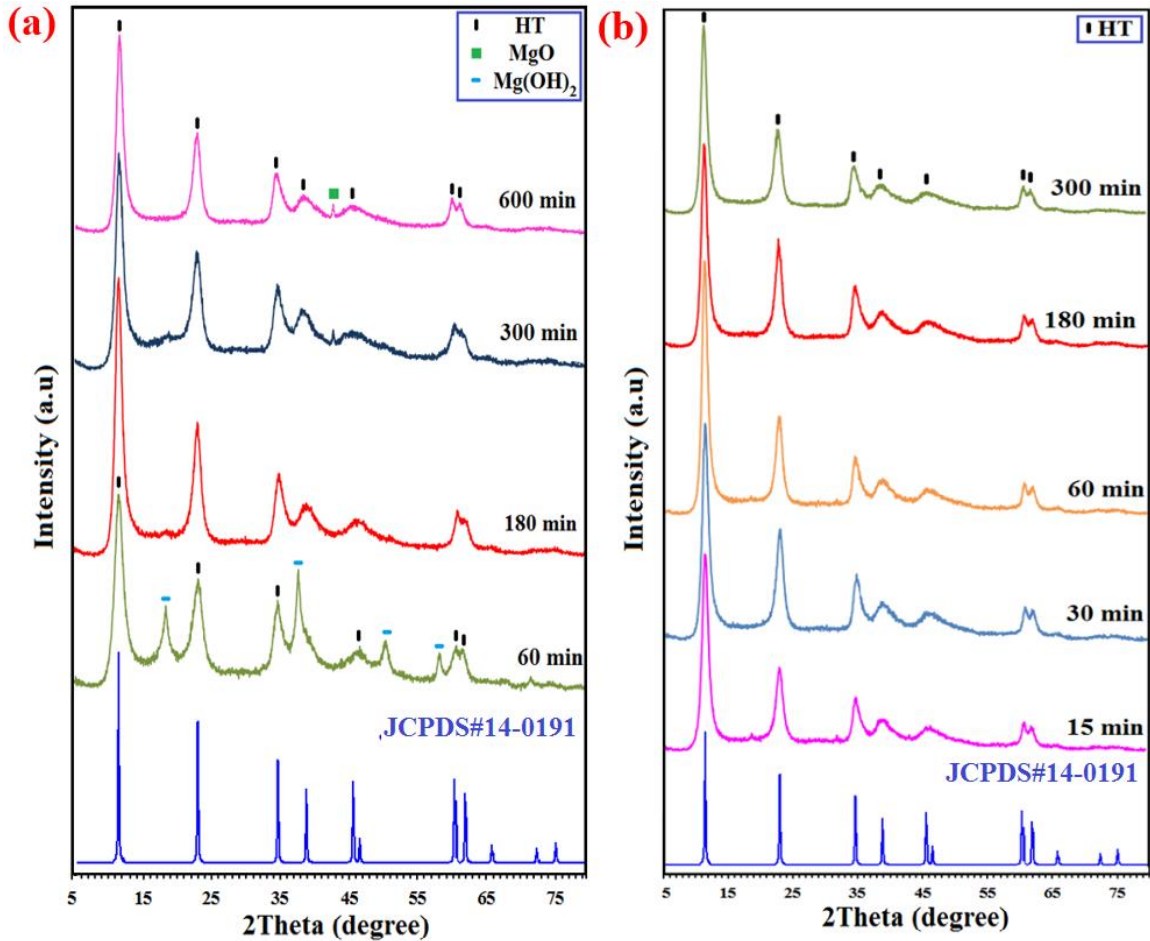


Fig 5. (a) XRD patterns of reaction 1 milled at different milling time, and (b) the patterns of reaction 2 milled at different milling time.

The XRD profiles of reaction 2 (R2) specimens milled at different milling times (15, 60, 180 and 300 min) are displayed in Fig. 5b. From these profiles, all the main peaks belonged to the characteristic peaks of HT (JCPDS#14-0191). There is a close structural similarity among different milling times. The pure product was formed at lower milling time (15 min). The intensity of main peaks increased by increasing milling times from 15 min to 60 min, and decreased with increasing milling time up to 300 min. The major

diffraction peaks and the crystalline order of the HT phase decreased. The phase identification of the milled samples between the two reactions is almost the same. Pure product of reaction 2 (R2) was obtained at lower milling time without any trace of impurities. Fig. 6 shows a plot of basal plane d -spacing as a function of different milling times for R1 and R2. The interlayer spacing (d) can be determined by averaging the basal peaks according to the equation (I) [45]:

$$d = \frac{1}{n} (d_{(003)} + 2d_{(006)} + \dots + nd_{(00n)}) \quad (\text{I})$$

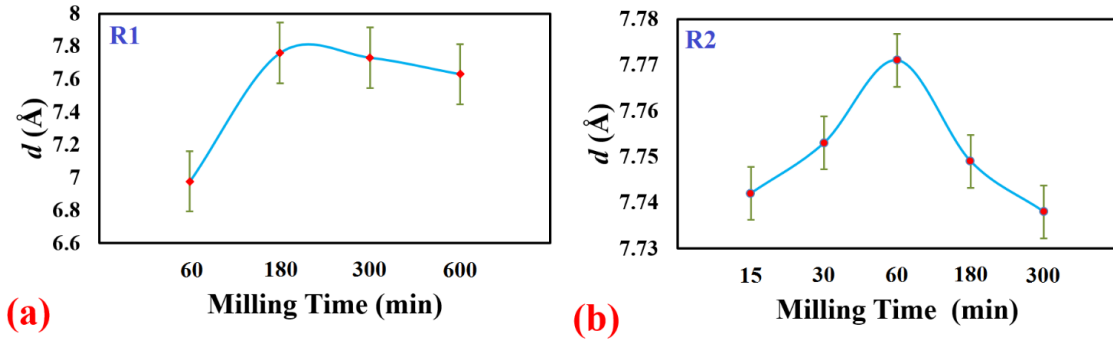


Fig. 6 Interlayer spacing of Mg-Al-CO₃-LDH prepared from reaction 1 (a) and 2 (b) as a function of milling time.

The results demonstrated that the interlayer spacing of HT structure is strongly influenced by milling time. It declined from 7.759 Å to 7.63 Å for R1 samples (180- 600 min). These values also decreased from 7.771 Å to 7.738 Å for R2 specimens (60-300 min). The reduction of interlayer spacing as a function of higher milling time is the shrinkage of the basal space because of the removal of water. This basal spacing is sensitive to the type of anion in the gallery.

2.1.2.2. Microscopic Observation

The FESEM images of 180 and 60 min milled samples from reactions (1) and (2) are shown in Fig. 7. This figure demonstrates the tendency for agglomeration of

mechanically induced nanopowders. Large agglomerates developed due to the moisture absorption of reactions (1) and (2) during the milling process and their large surface to volume ratio (Fig. 7a and b). Higher magnification of the SEM images indicates that each large agglomerate was composed of fine particles. The enlarged FESEM image of 180 min milled specimen in Fig. 7a exhibits the detailed morphologies of HT nanopowders (R1). They have a compact, homogeneous and well-crystallized nanostructure. Precise examination at higher magnification of 60 min milled sample (R2) illustrates that each agglomerate is comprised of many fine rounded particles with platelet morphology (Fig. 7b). Solid state diffusion dominates the coalescence of solid-like particles in milled samples [46].

Detailed microstructure information of HT nanopowders was characterized by TEM in Fig. 8. From TEM images, 180 (Fig. 8a) and 60 min (Fig. 8b) milled samples agglomerate which is in agreement with SEM observations. The TEM image of the milled samples were comprised of rounded platelet-like particles with an average size of about 50 nm.

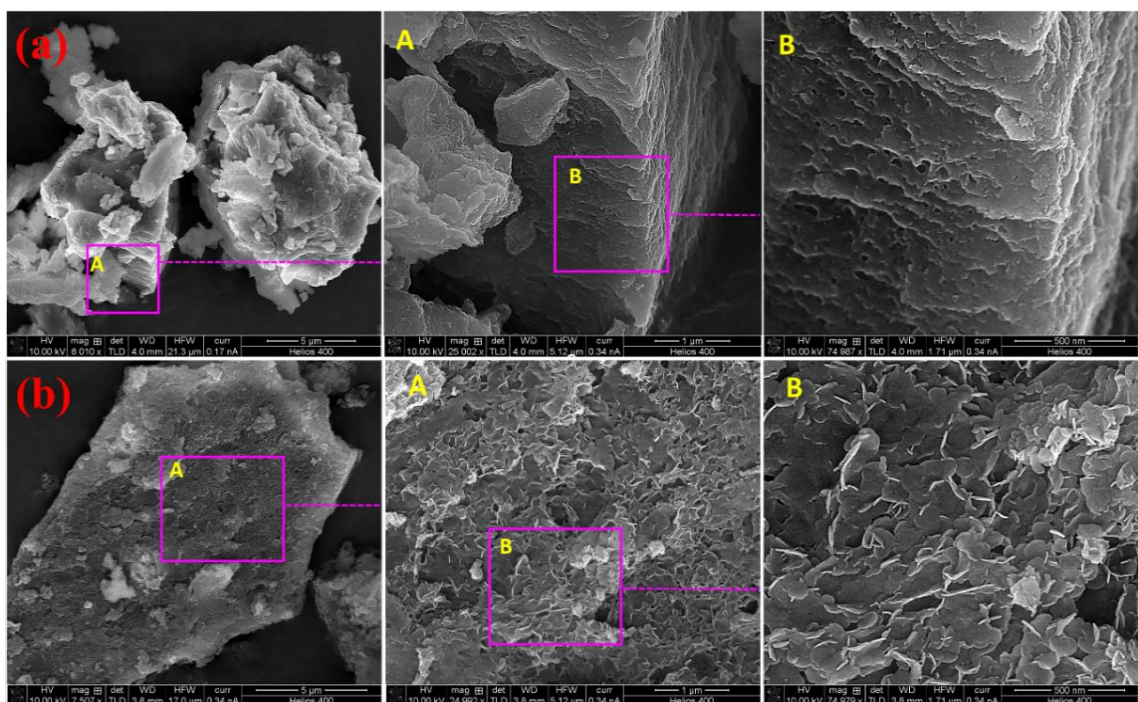


Fig. 7 (a) FESEM images of 180 min milled Mg-Al-CO₃-LDH obtained from reaction 1 (R1), and (b) 60 min milled sample from reaction 2 (R2).

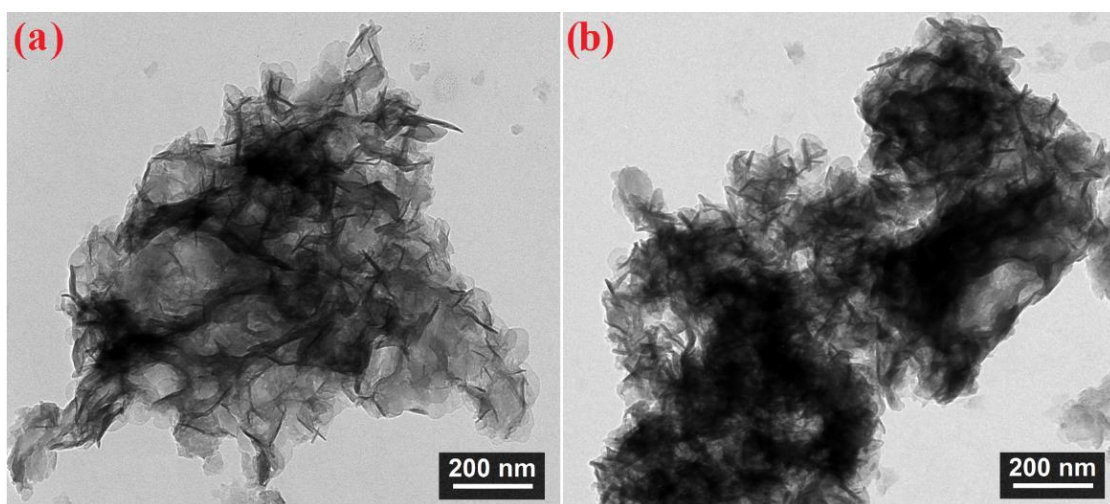


Fig. 8 (a) TEM images of 180 min milled Mg-Al-CO₃-LDH prepared from reaction 1 (R1), and (b) 60 min milled sample from reaction 2 (R2).

The EDS analysis of 180 (R1) and 60 min milled samples (R2) are presented in Fig. 9. The EDS analysis was recorded from three different points on 180 min (R1) milled (Fig. 9a) and 60 min (R2) milled samples (Fig. 9b). Based on the EDS profiles, the main

elements of both specimens were oxygen, magnesium, aluminum, and carbon. Contamination from the wear of vials and balls was absent. The average amount of magnesium and aluminum present for 180 min sample (R1) was calculated to be 29.86 and 9.28 mass %, respectively. The values for the 60 min milled sample (R2) was 28.59 and 8.35 mass %, respectively. The mole ratio of magnesium to aluminum was 3.22, and 3.42 for 180 and 60 min, respectively. This was a little lower than the theoretical mole ratio (3.6). The similarity of the recorded data over three different points on both samples indicates a homogenous microstructure.

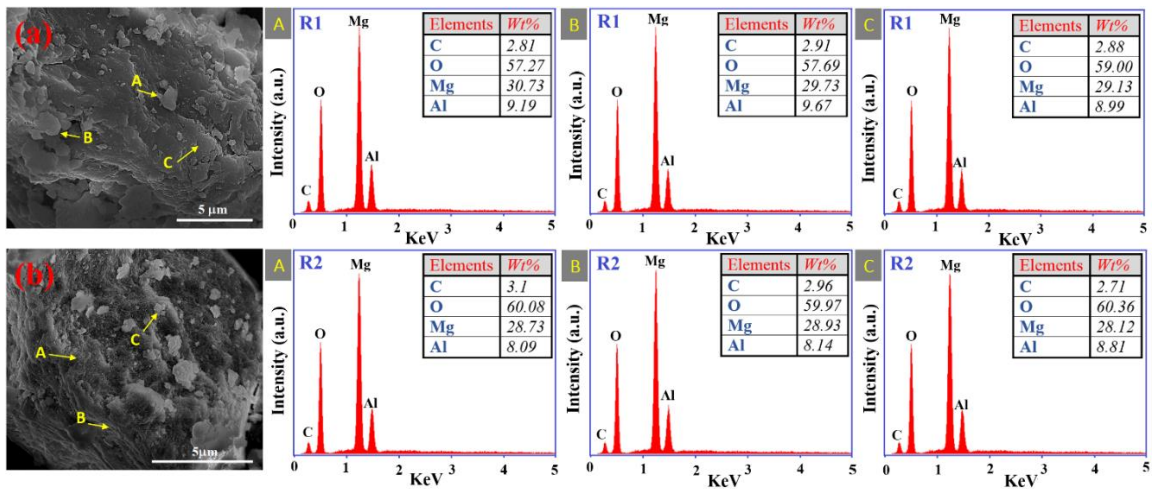


Fig. 9 (a) EDS spectra of 180 min milled Mg-Al-CO₃-LDH obtained from reaction 1 (R1), and (b) 60 min milled sample from reaction 2 (R2).

2.1.3. Conclusions

In this section, Mg-Al-CO₃-LDH was successfully synthesized through the MC method. Two reactions yielded a product with very similar structural characteristics. Results demonstrated that the formation and structural features of Mg-Al-CO₃-LDH were influenced significantly by milling time and the chemical composition of raw materials. Based on the phase analysis, the formation of HT from reaction 2 (R2) was obtained at

lower milling time when compared with reaction 1 (R1). The outcomes indicated that the phase purity of mechanically induced HT was affected by the chemical composition of raw materials. Reaction 2 (R2) is preferred to reaction 1 (R1) to produce carbonate intercalated HT with higher phase purity. By increasing milling time, the unit cell volume and interlayer spacing of products obtained from both reactions decreased. Electron microscopic evaluations showed the agglomeration of platelet-like structures of Mg-Al-CO₃-LDH samples with mean particle size of around 50 nm.

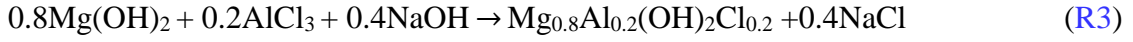
2.2. Chloride intercalated hydrotalcite

In this section, Chlorine intercalated Mg-Al layered double hydroxides (Mg-Al-Cl-LDH) with a chemical formula $Mg_{0.8}Al_{0.2}(OH)_2Cl_{0.2}$ were successfully produced by the one step mechanochemistry method. Subsequent water washing followed by aging at 80 °C for 1h finished the synthesis. The samples were characterized by XRD, FT-IR, FESEM, EDS, elemental mapping analysis, TEM, and DTGA. Results revealed that the structural characteristics of Mg-Al-Cl-LDH were affected by milling time. Based on the phase analyses, the product with high purity was obtained at 5h milling. The interlayer spacing of LDH was influenced by milling time. Electron microscopic observations indicated that the final product had hexagonal platelet structure with a lateral dimension of 20-100 nm. The synthesis of $Mg_{0.8}Al_{0.2}(OH)_2Cl_{0.2}$ via mechanochemistry based on simplicity and versatility can be a promising candidate for use in catalyst carriers, drug delivery, and gene delivery.

2.2.1. Materials and Experimental procedure

Magnesium hydroxide (95%, Sigma-Aldrich), Aluminum chloride (99 %, ACROS), and Sodium hydroxide pellets (97%, ACROS) were purchased and used as received. To synthesize $Mg_{0.8}Al_{0.2}(OH)_2Cl_{0.2}$, the desired amounts (2 g) of $Mg(OH)_2$, $AlCl_3$, and NaOH were milled at different milling times (1, 3, 5, 10, 15, and 20h) in a high energy ball mill using hardened chromium steel vials under air atmosphere. The weight ratio of ball-to-powder (BPR) was 10:1. The mole ratio of magnesium to aluminum was equal 4. The powders were washed three times with deionized water (20

ml) on a paper filter, and dried in a lab oven at 80°C for 1h. The target composition was based on the following reaction (R3):



The XRD patterns were scanned from 5 to 80 degrees 2θ at an interval step size of 0.03 degrees, and compared to standards compiled by the Joint Committee on Powder Diffraction and Standards (JCPDS): card #14-0191 for Hydrotalcite, #44-1482 for Brucite and #05-0628 for Halite. The crystallite size and lattice strain of the products were calculated by the Williamson-Hall equation (II) [19]:

$$B\cos\theta = 0.9\lambda/D + \eta\sin\theta \quad (\text{II})$$

where λ is the X-ray wavelength (0.154056 nm), D is the crystallite size, η is the internal micro-strain, θ is the Bragg angle ($^\circ$), and B is the peak width (in radians). The values of η and D were obtained by plotting $B\cos\theta$ versus $\sin\theta$, where η represents the slope and $0.9\lambda/D$ the intercept of the line. Based on equation (II), the crystallinity degree (X_c) was obtained by taking the sum total of relative intensities of individual characteristic peaks:

$$X_c = \text{SUM}(I_1:I_n)_{HT} / \text{SUM}(I_1:I_n)_{Standards} \times 100 \quad (\text{III})$$

where $I_1:I_n$ is the total of relative intensities of characteristic peaks of HT for both the synthesized powders and standard.

The lattice parameters (a , and c) can be determined for (003) and (110) Miller's planes from the following relation (IV):

$$\frac{1}{d^2} = \frac{4}{3} \frac{h^2+hk+k^2}{a^2} + \frac{l^2}{c^2} \quad (\text{IV})$$

where h , k , and l are the Miller indices. The unit cell volume (V) of the samples was also calculated using the following equation [20]:

$$V = (a^2c)\sin 60^\circ \quad (\text{V})$$

2.2.2. Results and discussions

2.2.2.1. XRD analysis

The x-ray diffraction patterns for all different milling time runs (1-20h) before and after washing and drying can be seen in Fig 10. Based on Fig. 10a, the main products of mechanical activation were sodium chloride, Brucite and HT for all the samples. The presence of Brucite after 1h milling indicates mechanochemical reaction was not complete. It almost disappeared with increasing of milling time up to 5h. Fig. 10b shows the XRD profiles of the samples after washing and drying at 80°C for 1h. The X-ray profile of the 1h milled sample exhibits the most intense peaks of Brucite and HT. The peaks corresponding to the sodium chloride vanished entirely. This trend continued for the 3h milled specimen with considerable changes in intensity of peaks. The intensity of HT peaks increased, and Brucite declined. The milling time was not sufficient to have pure HT formation. Brucite remained in this sample. The XRD pattern of the 5h milled sample resulted in a pure phase composition of HT. An increase in the milling time up to 20h led to further sharpening of the major diffraction peaks and growth in crystalline order of the HT phase with a trace of Periclase (MgO). This confirms that HT decomposed slightly as the milling time increased.

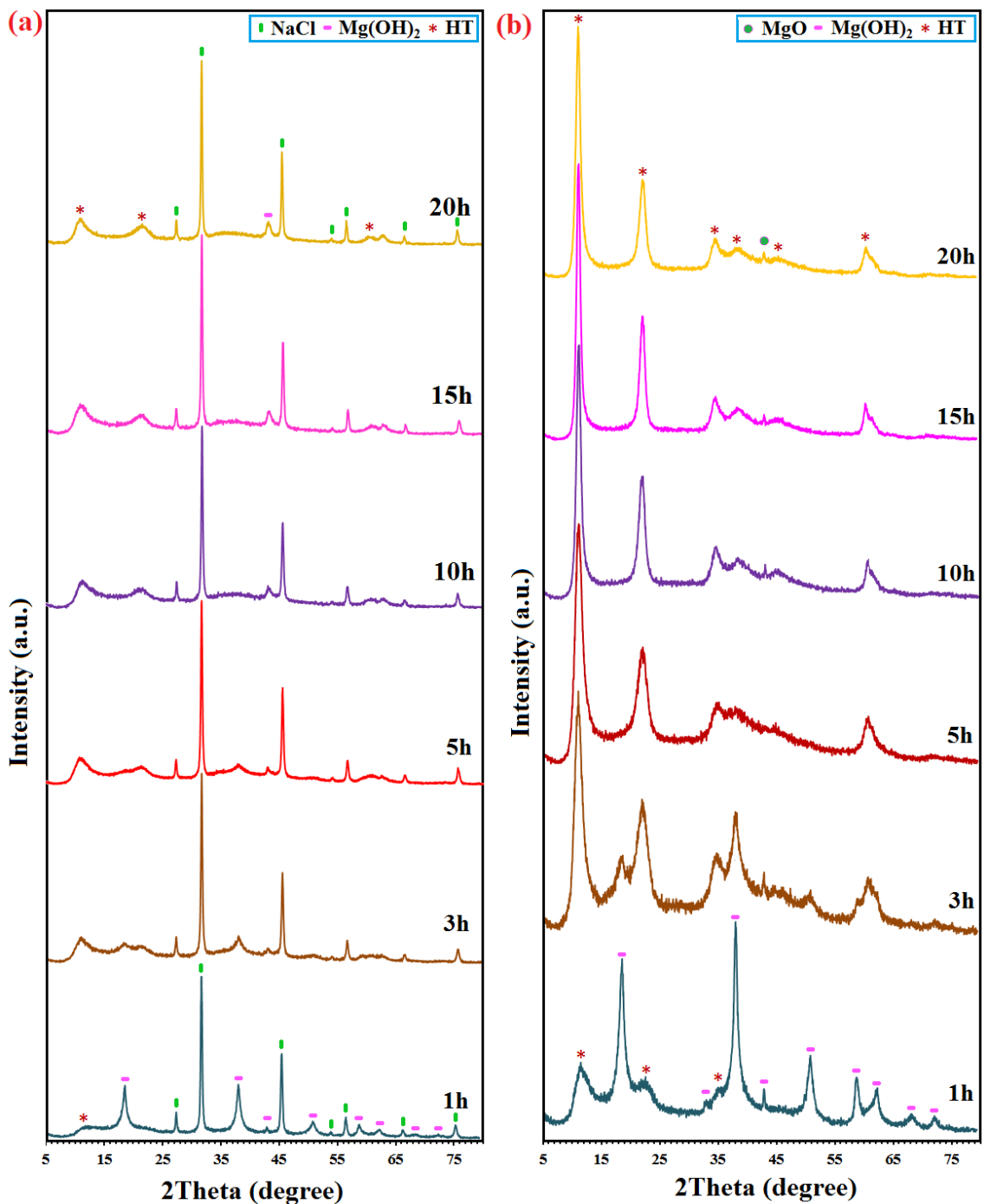


Fig. 10 XRD profiles of samples as function of milling time before (a) and after (b) washing with deionized water followed by drying.

All sharp peaks corresponding to chloride intercalated HT were shifted gradually toward higher d spacing owing to presence of chlorine ions instead of carbonate ions (see Fig. 11). The XRD patterns along with the magnified region between $2\theta = 7^\circ$ to 25° of

carbonate intercalated LDH (Mg-Al-CO₃-LDH) and Mg-Al-Cl-LDH samples milled for 5h were compared in Fig. 11. Mg-Al-Cl-LDH with proper crystallinity was successfully formed. The diffraction patterns resembled the carbonated form of HT.

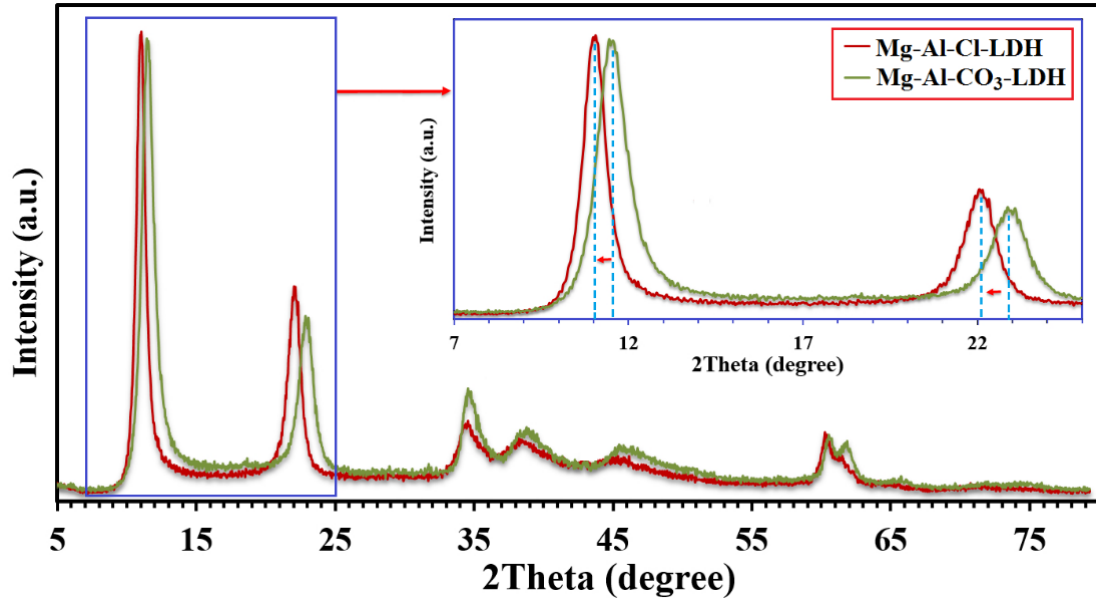


Fig. 11 XRD patterns along with the magnified region between $2\theta = 7^\circ$ to 25° of Mg-Al-CO₃-LDH and Mg-Al-Cl-LDH samples milled for 5h.

2.2.2.2. Structural features

The crystallite size (D), lattice strain (η), and crystallinity degree (X_c) of products as a function of milling time are shown in Fig. 12. In Fig. 12a, the crystallite size of specimens was obtained in the range of 5 ± 0.4 to 24 ± 0.5 nm (1-20h). The growth of crystallite size is affected by milling time so that there was an upward trend from 1h to 15h milled specimens and downward after 20h milling. The lattice strain of the samples declined from 0.0691 ± 0.0001 to 0.0007 ± 0.0001 as a function of milling time. The crystallinity of milled nanopowders is displayed in Fig 12b. The crystallinity of milled

samples increased significantly by approximately 43% with increasing milling time (1-15h). It declined for 20h milled powders to $40\pm 2\%$.

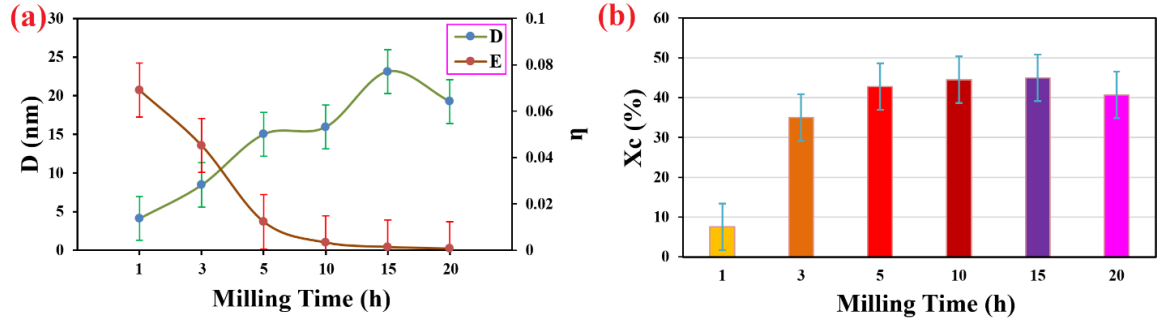


Fig. 12 (a) crystallite size, lattice strain, and (b) crystallinity degree of samples (Mg-Al-Cl-LDH) as a variation of milling time.

Fig. 13 illustrates the interlayer spacing (d), lattice constants (a , and c) and unit cell volume of the milled powders as a function of milling time. The basal spacing between layers of $Mg_{0.8}Al_{0.2}(OH)_2Cl_{0.2}$ as a function of milling time is displayed in Fig. 13a. The data demonstrated that the interlayer spacing of the Brucite structure is influenced by milling time. It increased from 7.737 ± 0.001 to 8.005 ± 0.002 (1-15h) and decreased to 7.937 ± 0.001 for the 20h milled sample. The reduction of interlayer spacing in higher milling time (20h) is due to the removal of water. This basal spacing is very sensitive to the type of anion in the gallery. Fig. 13b and c present the lattice constants and unit cell volume of milled nanopowders as a function of milling time. Based on the standard data of HT (JCPDF#14-0191), a -axis values were 3.07\AA , and c -axis values were 23.23\AA , respectively. As

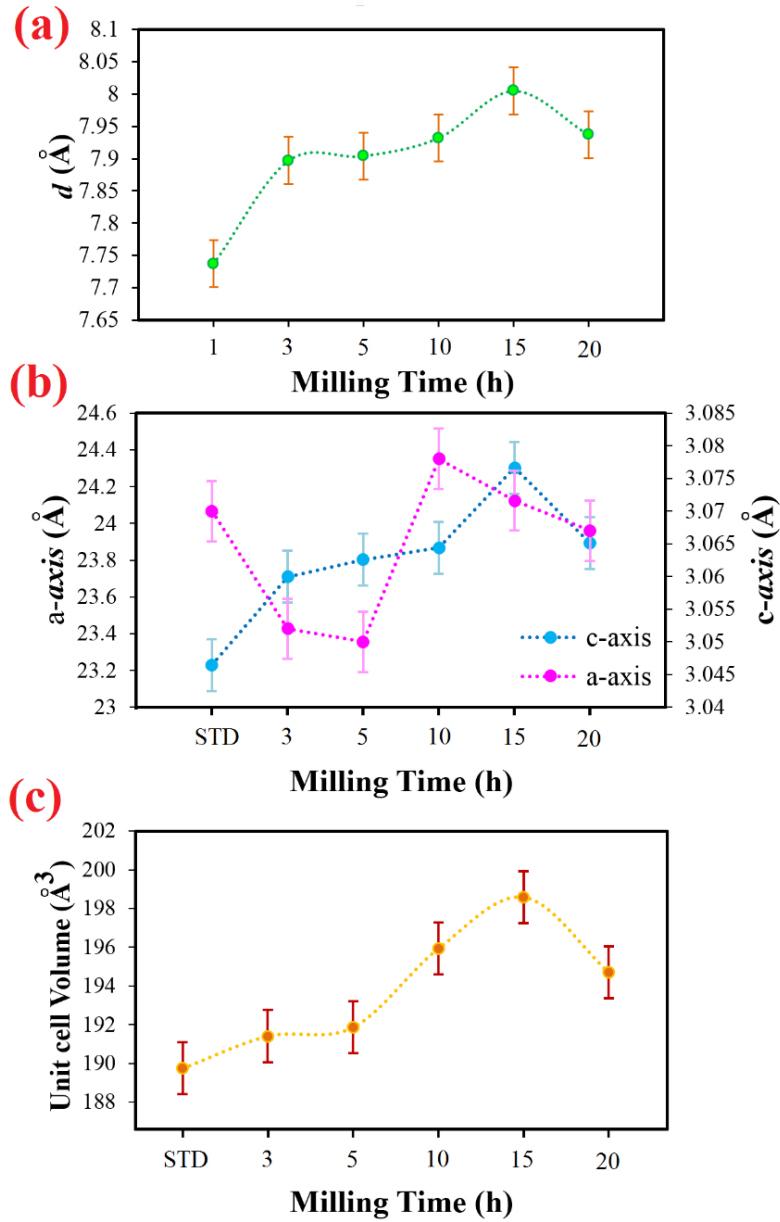


Fig. 13 (a) Interlayer spacing, (c) lattice constants, and (d) unit cell volume of specimens (Mg-Al-Cl-LDH) as a function of milling time.

Compared with the data obtained from equation IV, the a -axis and c -axis values were different. An overall upward trend for milled samples as milling time increased (1-15h) except for the 20h milled specimen. Chloride intercalated LDH led to small changes in the a -axis and c -axis as compared with HT. According to Fig. 13c, unit cell volumes of

the milled powders increased considerably from 191.3 ± 0.01 to $198.57 \pm 0.02 \text{ \AA}^3$ as milling time increased (1-15h) and declined to $194.63 \pm 0.02 \text{ \AA}^3$ for the 20h milled sample. The disparities in the values of unit cell volume resulted from increases in the c constant rather than from the a parameter. This could be related to the structural changes of $\text{Mg}_{0.8}\text{Al}_{0.2}(\text{OH})_2\text{Cl}_{0.2}$ during the milling process. The structural features of the mechanothesized Mg-Al-Cl-LDH were a function of the milling time.

2.2.2.3. FT-IR analysis

The FT-IR spectra of $\text{Mg}_{0.8}\text{Al}_{0.2}(\text{OH})_2\text{Cl}_{0.2}$ powders as a function of milling time are recorded in Fig. 14. The spectrum of the initial reactants for 1h milling contains a narrow intensive band corresponding to the stretching vibrations of Brucite (3700 cm^{-1}), a broad Hydroxyl band (ν_2) at 3463 cm^{-1} (owing to crystallization and adsorbed water), a weak water band (δ) at 1636 cm^{-1} (due to the bending vibrations of water), and two bands at 556 and 448 cm^{-1} (due to Mg-O vibrations and Mg-O-H bending) [5]. The absorption bands at 1384 (ν_3), 863 (ν_2), and 668 cm^{-1} (ν_4) indicates the stretching vibration of CO_3^{2-} , which is owing to the absorption of CO_2 from the air [24]. With increasing milling time up to 3h, a sharp drop in the intensity of the Brucite band (3700 cm^{-1}) is observed demonstrating the reaction of magnesium hydroxide with the other components. This band is completely vanished for longer milling time (5- 20h). This supports to the results obtained from XRD data. The intensity of the CO_3^{2-} band at 1384 cm^{-1} (ν_3), begins to decrease at 5h milling sample as the amount of Brucite decreases. It increases again for longer times (10-20h). Periclase appeared in those sample due to the partially decomposition of HT. The results are agreement with XRD profiles.

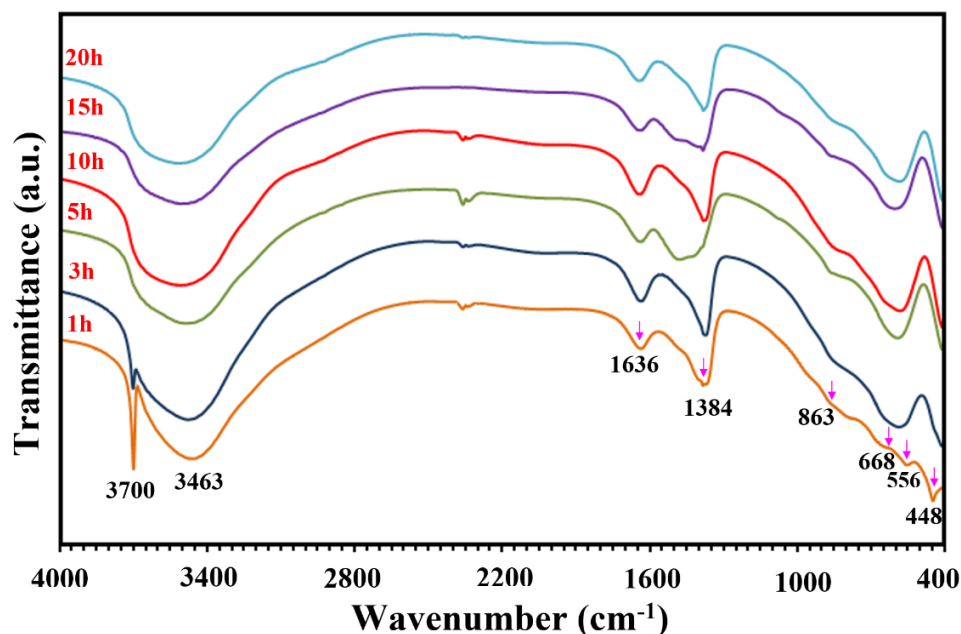


Fig. 14 FT-IR spectra of specimens (Mg-Al-Cl-LDH) as a variation of milling time.

2.2.2.4. Morphological characterization

Fig. 15 shows FE-SEM and TEM micrographs of the 5h milled sample. At low magnification of this sample (Fig. 15a), the milled sample had a high tendency to agglomerate owing to the large surface area of the powders [25]. In mechanochemical activation, two particles share common crystallographic orientation as two adjacent particles collide. Two particles blend into others to produce agglomeration [26]. The product with a platelet structure containing smaller particles is shown in higher magnification of FESEM figure (Fig. 15b). Fig. 15c displays a typical TEM image of 5h milled specimen. The particles were shaped hexagonally with a lateral dimension of 20-100 nm. The hexagonal platelet particles containing small nanoparticles with different lateral dimensions were overlapped. The lateral dimension from TEM images is almost equivalent to the data calculated from XRD data. The morphology obtained by this method is similar to results obtained through co-precipitation and hydrothermal methods

[47, 48, 49]. MC is a facile and cost effective process for massive production of Mg-Al-CI-LDH with appropriate morphological features.

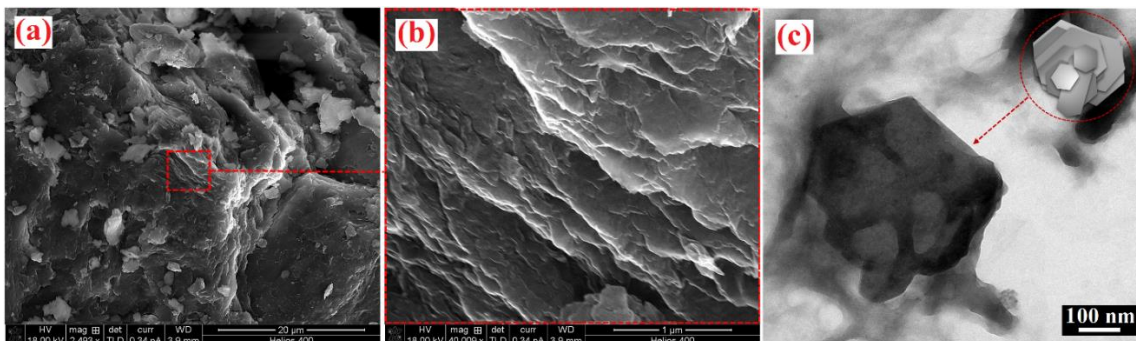


Fig. 15 Morphological features of 5h milled sample (Mg-Al-CI-LDH): (a) low, (b) high magnification FE-SEM images and (c) TEM image.

Fig. 16 exhibits EDS spectrum and the elemental mapping analysis of the 5h milled sample. The chemical composition of Mg-Al-CI-LDH as an average of three different prepared samples is presented in Table 1. The total amount of magnesium and aluminum present on Mg-Al-CI-LDH was estimated to be 30.15 and 8.5 mass %, respectively. The mole ratio of magnesium to aluminum was 3.93, which was a little lower than the standard mole ratio. The main components of the sample were oxygen, magnesium, aluminum, carbon, and chlorine. Sodium chloride was the only by-product of milled sample, which was removed by washing. No other contaminants were detected. Fe contamination resulting from the wearing of the steel vials and balls was not detected. Elemental mapping analysis of the powders showed an appropriate distribution of elements. This confirmed the formation of homogenous microstructures during milling. Due to the high volume fraction of magnesium and oxygen in this specimen, those elements dominated parts of the sample. The chemical composition of Mg-Al-CI-LDH milled for 5h was determined by XRF and listed in Table 1. The result of XRF illustrates that the composition and structure of chlorine incorporated Hydrotalcites was very stable.

These findings are in good agreement with the standard and the results from the EDS measurement.

Table 1 Chemical composition of Mg-Al-Cl-LDH obtained from XRF and EDS.

Technique	Mg mass (%)	Al mass (%)	Cl mass (%)	Mg/Al (molar ratio)
EDS	30.15	8.5	10.5	3.93
XRF	32.71	9	10.65	4.03

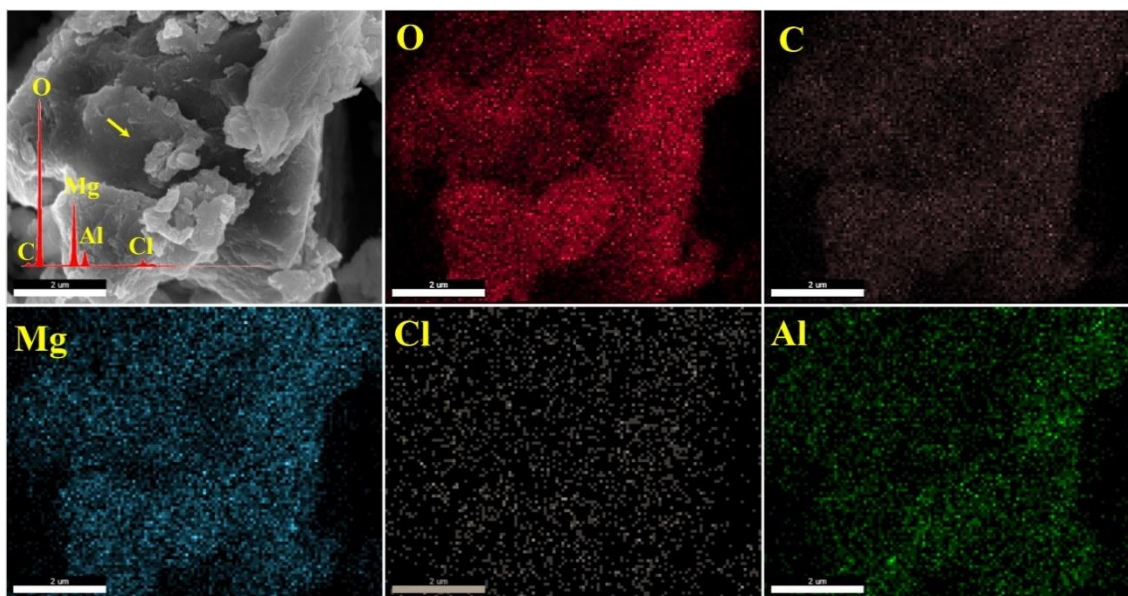


Fig. 16 EDS and elemental mapping analysis of 5h milled sample (Mg-Al-Cl-LDH).

2.2.2.5. Thermogravimetric analysis

Fig. 17 gives an overlay of the differential thermogravimetric analysis (DTGA) for 5h milled sample $\text{Mg}_{0.8}\text{Al}_{0.2}(\text{OH})_2\text{Cl}_{0.2}$. The mass loss occurred at several stages in the DTGA curve. The first mass loss of about 6% occurred at 40–80°C which may be the

elimination of physically bound absorbed water and/or the dissociation some of hydrated reactants which were formed during milling or washing. The Second from 80°C to approximately 220°C, corresponding to a mass loss of 10.77% associated to the interlamellar water loss. The final decomposition phase from 220°C to 510°C with a mass loss of 25.6% attributed to the dihydroxylation of the LDH lamellae. From 510°C, there is a constant residual mass attributed to the formation of the magnesium and aluminum mixed oxide, corresponding to ~ 45% of the initial mass.

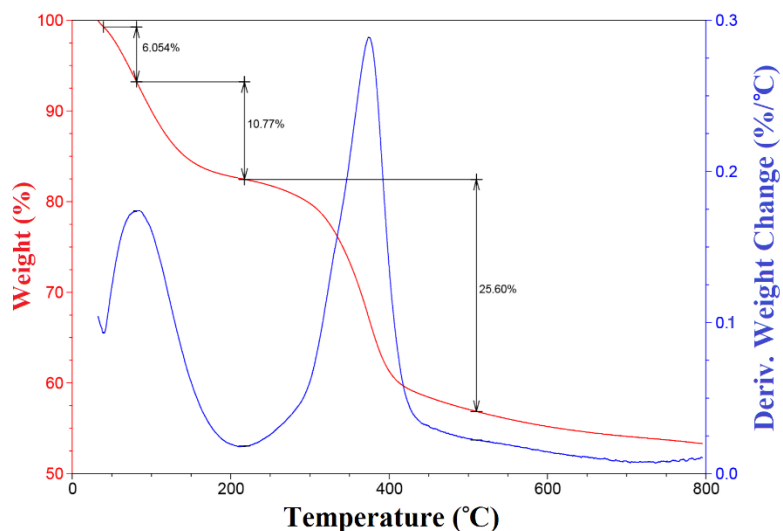


Fig. 17 DTGA of 5h milled sample (Mg-Al-Cl-LDH) as a function of temperature.

2.2.3. Conclusions

A facile and more productive method was developed to prepare $\text{Mg}_{0.8}\text{Al}_{0.2}(\text{OH})_2\text{Cl}_{0.2}$ by mechanochemistry method. The method produced mineral with similar characteristics to that obtained by co-precipitation and hydrothermal processes. Results demonstrated that the formation and structural features of Mg-Al-Cl-LDH were influenced significantly by milling time. The crystallite size, crystallinity, interlayer spacing and unit cell volume rose nonlinearly as milling time increased from 1 to 15h and

declined for longer milling time (20h). The lattice strain of the powders decreased gradually. The XRD and FTIR spectra confirmed that pure $\text{Mg}_{0.8}\text{Al}_{0.2}(\text{OH})_2\text{Cl}_{0.2}$ was obtained at 5h milling without any trace of Brucite. Microscopic observations showed a hexagonal platelet structure containing small particles with a lateral dimension of 20-100 nm. No other chemically stable contaminants were detected from XRF, and EDS. The DTGA data for the Mg-Al-Cl- LDH indicates three mass loss events during the thermal decomposition of the LDH. The mechanothesized $\text{Mg}_{0.8}\text{Al}_{0.2}(\text{OH})_2\text{Cl}_{0.2}$ has the appropriate structural and morphological features of LDH. It is suitable for target delivery especially for gene delivery.

2.3. Chloride intercalated hydrotalcite: mechanochemistry vs. hydrothermal

The chloride intercalated Mg-Al layered double hydroxides (Mg-Al-Cl-LDH) with different degrees of ion substitution and chemical formula of $\text{Mg}_{1-x}\text{Al}_x(\text{OH})_2 \text{Cl}^-_x$ were successfully prepared by two methods; one-step mechanochemical activation and the hydrothermal method. For a comparative study of the mechanically activated samples versus hydrothermally treated specimens, the structural features such as crystallite size, lattice strain, crystallinity, the interlayer spacing, and the unit cell volume of samples were determined. Results revealed that the phase purity of products was strongly influenced by different ion substitution degrees ($X=0.12, 0.18, 0.3, \text{ and } 0.42$). The unit cell volume and interlayer spacing of LDH obtained from both processes was also influenced by degrees of substitutions. Microscopic observations were also reported. Detailed analysis of the phase behavior and structural trends revealed that Mg-Al-Cl-LDH can be synthesized more easily and rapidly in high energy ball mill as compared with LDH prepared by the hydrothermal method. The product obtained from hydrothermal method showed greater crystallinity.

2.3.1. Materials and experimental procedure

2.3.1.1. Mechanochemistry method

Magnesium chloride (99%), Aluminum chloride (99 %), and Sodium hydroxide pellets (97%) were purchased from ACROS and used as received. The mechanochemical activation was done in a high energy ball mill for 60 min using hardened chromium steel vials (vol. 65 ml) at room temperature. The weight ratio of ball-to-powder (BPR) was 10:1. The designed degree of substitution of chloride was designated by the x value in the

general formula of $\text{Mg}_{1-x}\text{Al}_x(\text{OH})_2\text{Cl}^{-x}$, where x values were chosen equal to 0.12, 0.18, 0.3, and 0.42. The synthesized nanopowders were designated as M1, M2, M3, and M4, respectively. The target composition was adjusted according to the following general reaction (R4):



The powders were washed three times with deionized water (20 ml) on a paper filter, and dried in an oven at 80°C for 1h.

2.3.1.2. Hydrothermal method

Mg-Al-Cl-LDH with different amount of ions substitutions (0.12, 0.18, 0.3, and 0.42) was prepared via hydrothermal technique according to the following recipe. The products were labeled as H1, H2, H3 and H4, respectively. The target composition was adjusted according to [Table 2](#). $\text{Mg}_{0.82}\text{Al}_{0.18}(\text{OH})_2\text{Cl}_{0.18}$, for instance, had a formula of 1.8006 g of Aluminum chloride and 9.0256 g of Magnesium chloride. They were dissolved into 20 mL of deionized water and stirred at ambient temperature. 8 g of NaOH was dissolved into 20 mL of deionized water until clear solution was obtained. The solution was put into a burette and allowed to drop into the Mg/Al solution until the pH reaches 10. The mixture was transferred to a Teflon lined stainless steel autoclave. The autoclave was heated with an electric oven to 120°C for 2h. The supernatant was filtered and washed three times with deionized water (20 ml).

Table 2 Details of solution components

Series	Degree of substitution $\text{Mg}_{(1-X)}\text{Al}_X(\text{OH})_2\text{Cl}_X$	MgCl_2 (g)	AlCl_3 (g)	Phase composition	Mg/Al
H1	0.12	9.0256	1.8006	$\text{Mg}_{0.88}\text{Al}_{0.12}(\text{OH})_2\text{Cl}_{0.12}$	7.33
H2	0.18	8.4102	2.7009	$\text{Mg}_{0.82}\text{Al}_{0.18}(\text{OH})_2\text{Cl}_{0.18}$	4.55
H3	0.3	7.1794	4.5015	$\text{Mg}_{0.7}\text{Al}_{0.3}(\text{OH})_2\text{Cl}_{0.3}$	2.33
H4	0.42	5.9487	6.3021	$\text{Mg}_{0.58}\text{Al}_{0.42}(\text{OH})_2\text{Cl}_{0.42}$	1.38

2.3.2. Result and discussion

2.3.2.1. XRD analysis

The XRD patterns of Mg-Al-Cl-LDH with different amount of ions substitutions ($X = 0.12, 0.18, 0.3,$ and 0.42) prepared by hydrothermal (H) and mechanochemistry (M) are exhibited in Fig. 18. There is a close structural similarity between the two compounds based on the nearly identical diffraction data. Fig. 18a shows the XRD profiles of hydrothermally treated samples. From these profiles, all the main peaks belonged to the characteristic peaks of HT (JCPDS#14-0191). At low Al substitution ($X = 0.12$), Brucite and HT co-exist. At high Al substitutions ($X = 0.42$) Gibbsite appears as an additional phase with HT. Pure HT was obtained in the midrange concentration ($X = 0.18$). HT is the dominant phase at $X = 0.3$, and a weak peak corresponding to Gibbsite still remains. Fig. 18b illustrates mechanothesized samples at four different ion replacements. Based on these patterns, all the characteristic peaks of HT are present. The phase identification of the milled samples is almost the same as the hydrothermal powders; however, the peak broadening increased as the ion contents increased.

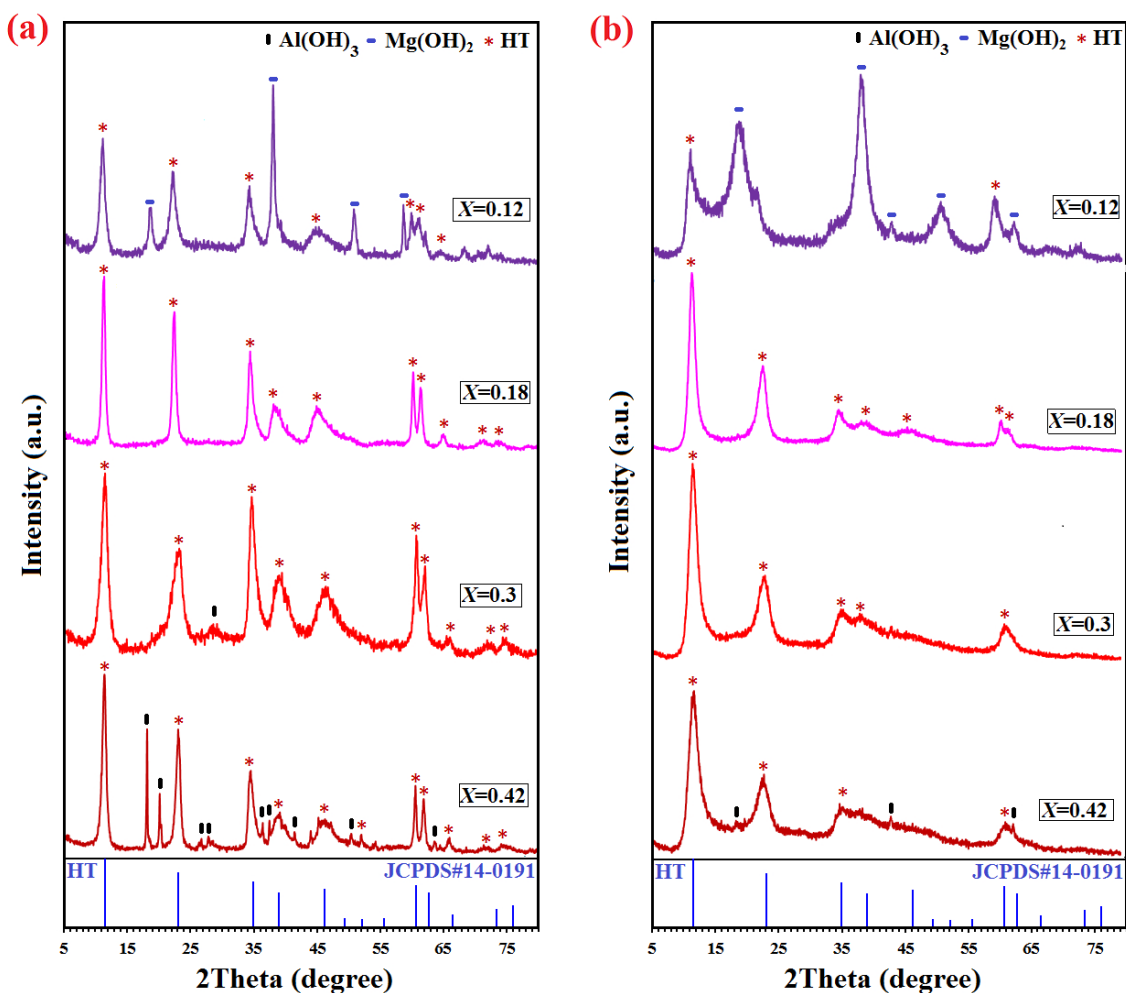


Fig. 18 XRD profiles of samples as a function of ion contents degree (X) prepared by Hydrothermal (a) and Mechanochemistry methods (b).

The intensity differentiation and the line broadening of XRD patterns in the range of $2\theta = 7^\circ$ to 25° are shown in Fig. 19. For hydrothermally treated samples (Fig. 19a), with increasing ion substitution of 0.18 and 0.42 (H2, and H4), the intensities of HT peaks increased and the peaks became narrower, while it decreased significantly for H1 and H3 samples and the peaks broaden. The peaks corresponding to HT for H2 sample were shifted gradually toward higher d spacing which may be due to changes in lattice parameters. Based on Fig. 19b, similar trend can be also observed for the milled samples; however, the peak intensity of HT became more intense for M2. The results suggest that

the product (Mg-Al-Cl-LDH) with ion replacement of 0.18 (H2, and M2) had greater phase purity. The products were produced successfully through hydrothermal and mechanochemistry methods.

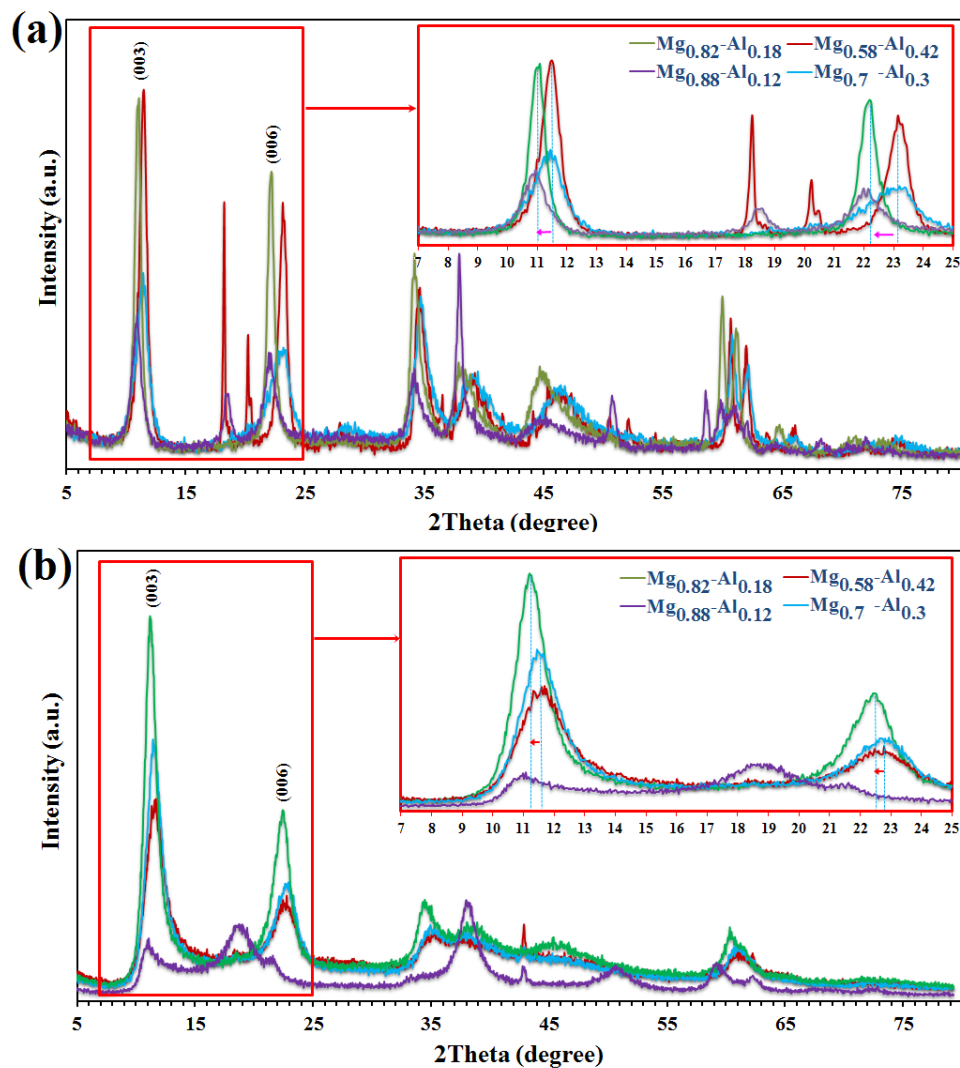


Fig. 19 XRD profiles along with the magnified regions between $2\theta = 7^{\circ}$ – 25° for samples prepared by Hydrothermal (a) and Mechanochemistry methods (b).

3.3.2.1.1 Crystallite size and lattice strain

The crystallite size (D), and lattice strain (η) of products synthesized by hydrothermal and mechanochemistry methods as a function of contour ion concentration

($X = 0.12, 0.18, 0.3, \text{ and } 0.42$) are shown in Fig. 20. According to the data calculated from equations II, the average crystallite sizes and lattice strains of HT from both processes were affected by different ion substitutions (Fig. 20a). The average crystallite size of specimens prepared hydrothermally was obtained in the range of 17.9 ± 0.3 to 20 ± 0.2 nm (H1-H4) indicating nonlinear trends. The trend of lattice strain magnitude was upward as ion replacement increased from 0.12 to 0.3 (0.0006 ± 0.00001 to 0.0209 ± 0.0002), while it decreased with additional substitution of 0.42 to 0.0089 ± 0.0001 . For the milled samples (Fig. 20b), the crystallite size increased in the range of 12 ± 0.2 to 18 ± 0.4 nm, while it reached a maximum value of 17.9 ± 0.2 nm in M2 sample ($X = 0.18$). The lattice strain values and it dropped considerably from 0.147 ± 0.003 to 0.0125 ± 0.0004 % when ion replacement rose from 0.12 (M1) to 0.18 (M2). These values increased for ion substitutions of 0.3 and 0.42. The average lattice strain is influenced by increasing ion replacements. It should be noted that the average rate of crystallite growth in hydrothermally treated samples is higher than in milled samples. This indicates that the product with higher crystallinity is obtained from the hydrothermal process as compared with milled samples. The crystallinity content will be discussed in more detail later.

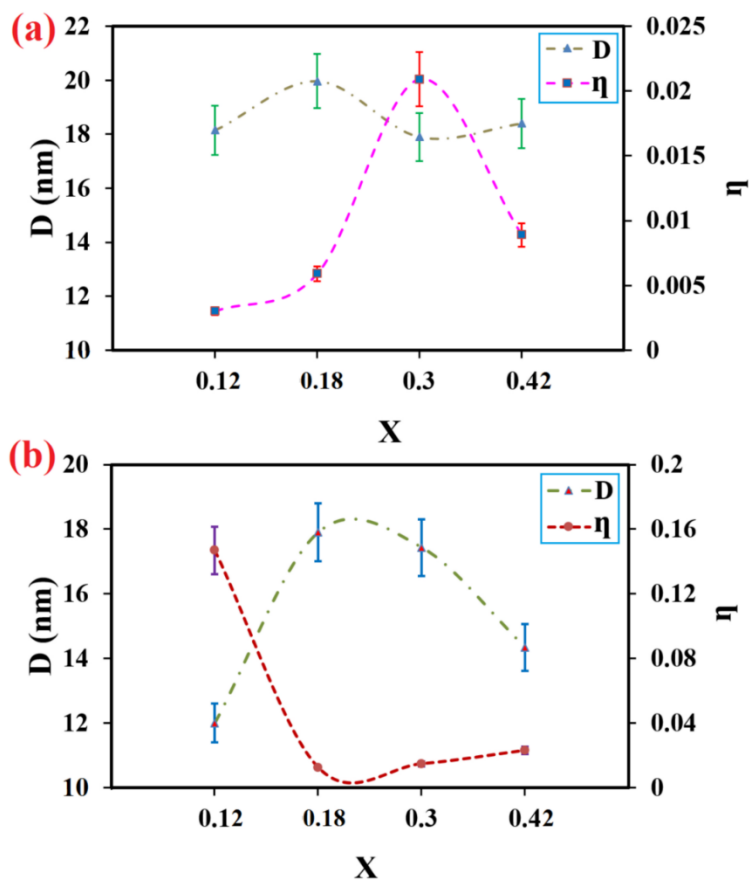


Fig. 20 Crystallite size, and lattice strain of samples prepared by Hydrothermal (a) and Mechanochemistry methods (b) as a variation of different ion contents (X).

3.3.2.1.2. Crystallinity degree (X_c)

Fig. 21 shows the FWHM values at different Bragg angles for hydrothermal and milled samples. The FWHM values demonstrated anisotropic line broadening. This may be caused by three factors: the presence of stacking faults, the existence of dislocations and none equivalence of the grain sizes along different crystallographic directions [22]. Anisotropic line broadening in this work was presumably the result of grain size anisotropy. The FWHM values of three different ion substitutions ($X = 0.18, 0.3,$ and 0.42) are exhibited in Fig. 21a, b and c, respectively. The average values of FWHM in milled specimens as a function of contour ion concentration are greater than the

hydrothermally prepared materials. This outcome is good agreement with the calculated results of crystallite size of both processes. The greater crystallite size belongs to lower FWHM values.

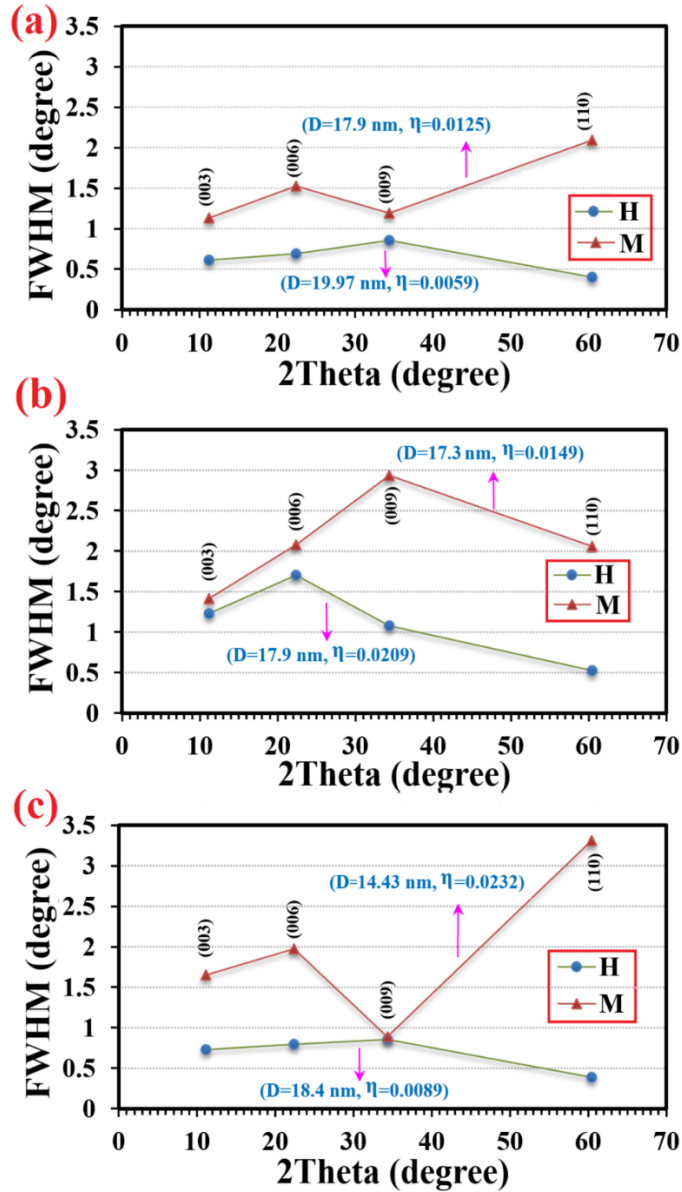


Fig. 21 FWHM of milled (M) and hydrothermally (H) treated samples at three different ion contents (X): (a) X=0.18, (b) X=0.3, and (c) X=0.42.

For further evaluation of the structural features, the degree of crystallinity of the powders was calculated from the following equation (VI) [50]:

$$X_C = 1 - \left(\frac{V_{015/009}}{I_{009}} \right) \quad (\text{VI})$$

where X_C is the crystallinity degree, I_{009} is the intensity of (009) plane, and $V_{015/009}$ is the minimum between (015) plane at $2\theta = 39.13$ and (009) plane at $2\theta = 34.73$. In Fig. 22, the fraction of crystalline phase of hydrothermally prepared samples is almost twice the milled samples. Based on Fig. 22, increasing the ion content (X) from 0.18 to 0.42 in hydrothermal samples (H2-H4) decreased, the crystallinity from 83 ± 4 to $74 \pm 3\%$, respectively. This downward trend was also obtained in the milled samples. The decrease was $38 \pm 2\%$ in $X = 0.18$ (M2) to a minimum of $16 \pm 1\%$, at $X = 0.42$ (M4). Results demonstrated that higher crystalline phase can be produced through the hydrothermal method.

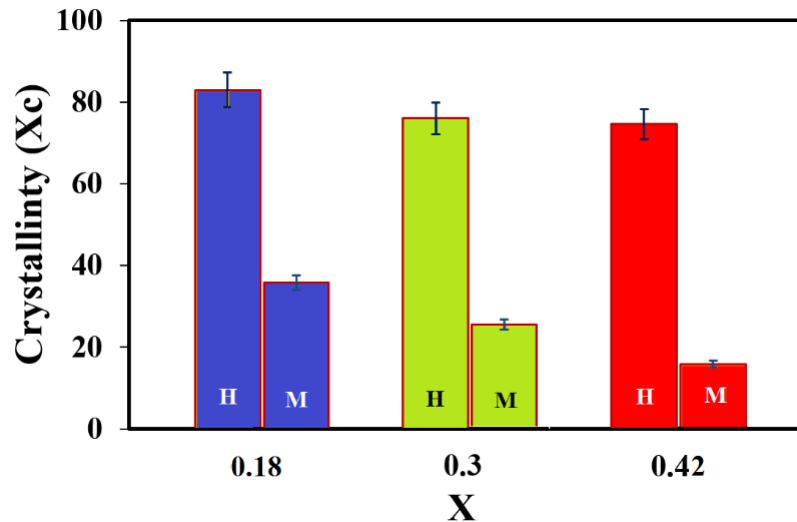


Fig. 22 Crystallinity degree of samples prepared by Hydrothermal (H), and Mechanochemistry (M) methods as a variation of ion contents (X).

3.3.2.1.3. Lattice parameters and interlayer space

To confirm the formation of HT, the lattice parameters were calculated from equation (IV) and compared with standard values. Fig. 23 exhibits the a -axis, c -axis

values, and unit cell volume of HT as a function of three different ion contents (0.18, 0.3, and 0.42). Based on the standard data (STD) of HT, *a*-axis and *c*-axis values were 3.07Å, and 23.23Å, respectively. Compared with the data calculated from equation IV, the *a*-axis and *c*-axis values for hydrothermal (Fig. 23a) and milled samples (Fig. 23b) were different. It shows an overall descending trend as ion content (*X*) increased from 0.18 to 0.42. Chloride intercalated LDH led to small changes in the *a*-axis and *c*-axis as compared with conventional HT. According to Fig. 23c, increasing *X* content from 0.18 to 0.42 resulted in unit cell volumes of the hydrothermal and milled samples decreasing from 196.89±0.01 to 184.94±0.02 Å³ and 192.7±0.02 to 185.6±0.0 Å³, respectively. From the data, it is clear that the disparities in the values for unit cell volume resulted from growths in the *c* constant, rather than from the *a* parameter.

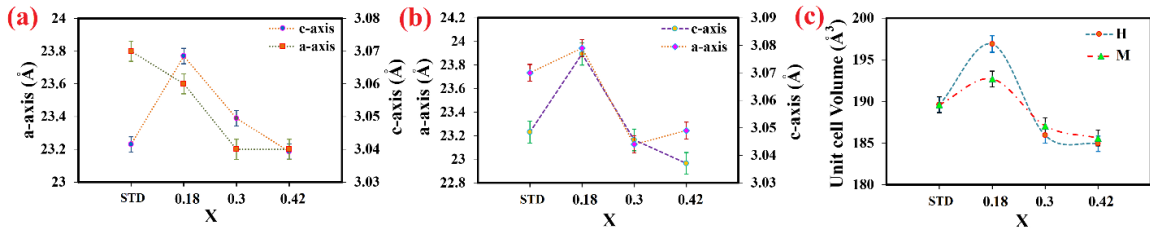


Fig. 23 lattice constants of hydrothermal specimens (a), mechanochemical samples (b), and Unit cell volume of specimens (c) prepared by Hydrothermal (H), and Mechanochemistry (M) methods as a variation of ion contents (*X*).

The shrinkage of unit cell volume can also be attributed to more substitution of chloride in HT structure. The structural features of the mechanosynthesized and hydrothermally treated Mg-Al-Cl-LDH were affected strongly by ion replacements.

Fig. 24 contains a plot of basal plane *d*-spacing as a function of ion substitution (*X* = 0.18, 0.3, and 0.42) and a comparison study of mechanochemical activation and hydrothermal methods. The interlayer spacing of the Brucite like structure is influenced by ion contents (*X*). It declined from 7.949±0.001 Å to 7.745±0.002 Å for milled samples

(M2-M4). The values for hydrothermal specimens (H2, H3) decreased from 7.895 ± 0.001 Å to 7.752 ± 0.002 Å, and increased to 7.797 ± 0.002 Å as ion content increased to 0.42 (H4). The reduction of interlayer spacing in higher ion contents is likely due to the shrinkage of the basal space by the removal of water. This basal spacing is very sensitive to the type of anion in the gallery.

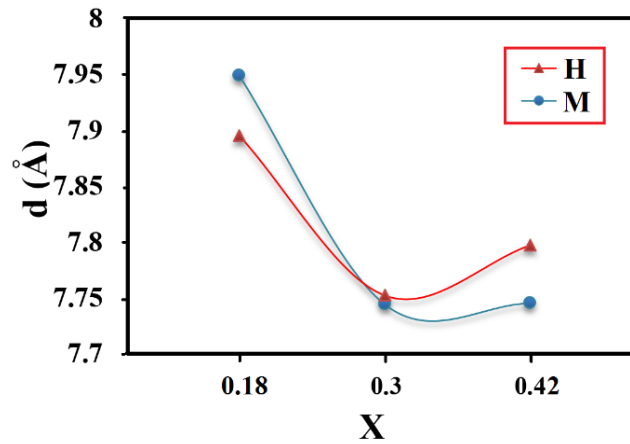


Fig. 24 Interlayer spacing of specimens prepared by Hydrothermal (H), and Mechanochemistry (M) methods as a function of ion contents degree(X).

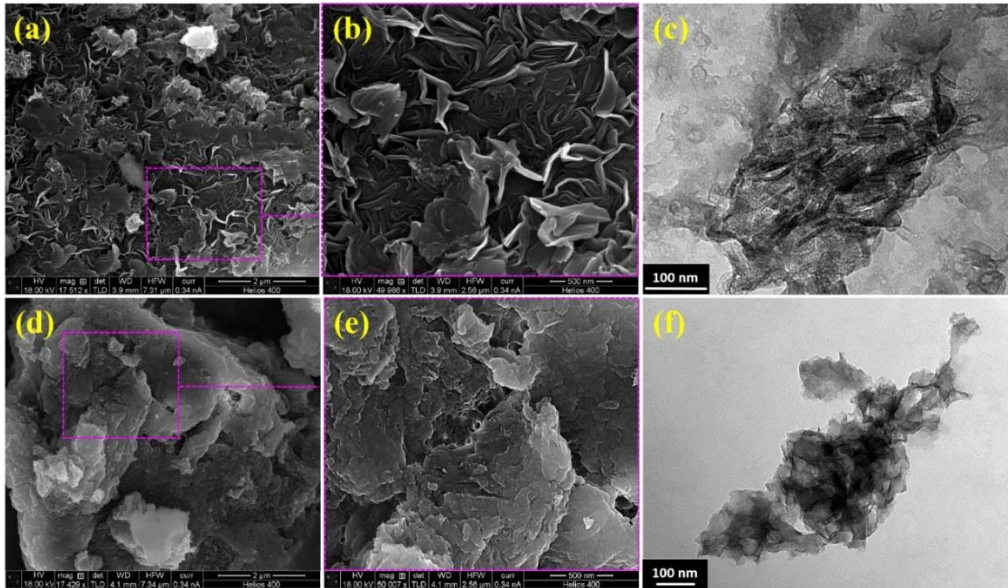


Fig. 25 (a,b) FESEM and (c) TEM images of hydrothermal sample (H2), (d,e) FESEM and (f) TEM images of milled sample (M2).

2.3.2.2. Morphological characterization

The FESEM and TEM images of the synthesized powders with ion replacement of 0.18 (H2, and M2) are shown in Fig. 25. Fig. 25a illustrates that the LDH powders possess a typical platelet microstructure which are assembled with numerous interlaced curved nanoplates. The enlarged FESEM image in Fig. 25b indicates the detailed morphologies of the LDH nanopowders. They are a compact, homogeneous and well-crystallized nanostructure. In Fig. 25c, the hydrothermal nanopowders (H2) is composed of a layered structure with a mean particle size of about 40 nm. As can be seen in Fig. 25d, the milled nanoparticles (M2) exhibit a tendency to agglomerate due to their large surface to volume ratio. Precise examination at higher magnification demonstrates that each agglomerate comprises of many fine round particles with platelet morphology (Fig. 25e). The TEM image of the milled sample indicates a laminar structure which is characteristic for hydroxide mineral and the stacking of the layers. The ill-defined crystallite structures of the milled sample demonstrate agglomerations of the crystallites. The average particle size of 30 nm for M2 by TEM is smaller than the 40 nm for H2. The average lateral particle sizes from TEM are significantly bigger than the crystallite sizes extracted from the XRD profiles. XRD only probes the size of the crystalline domains of the agglomerated particles. The results are in good accordance with the literature [51].

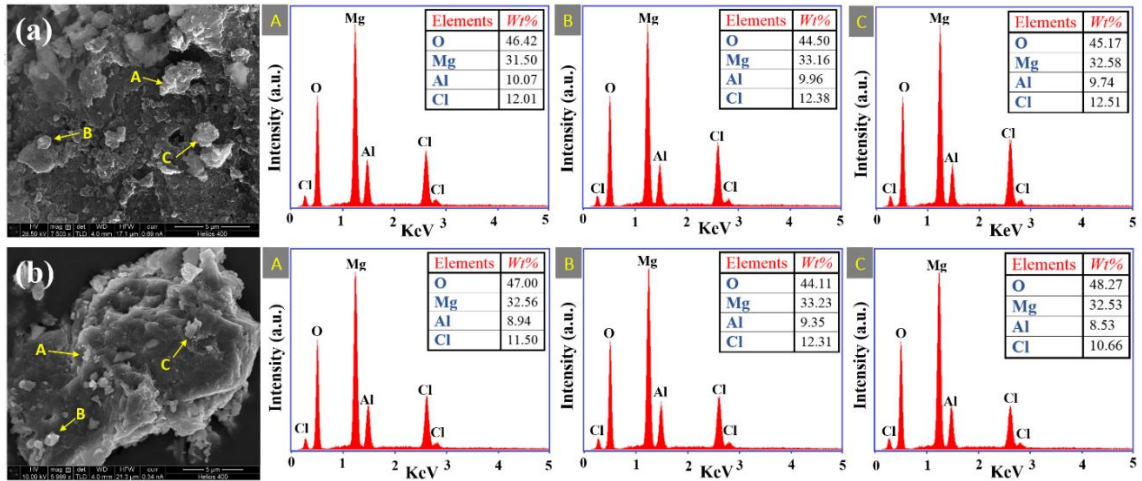


Fig. 26 EDS spectra of (a) hydrothermal sample (H2), and (b) milled sample (M2).

The chemical composition of hydrothermal treated and milled samples (H2, and M2) were measured by EDS analysis. Typical profiles have been selected and presented in Fig. 26. To provide more accurate results, the EDS analysis was recorded over three different points on the hydrothermal (Fig. 26a), and milled samples (Fig. 26b). The main components of both samples were oxygen, magnesium, aluminum, and chlorine. Contamination from excessive wear of vials and balls was absent. The average amount of magnesium and aluminum present on the hydrothermal sample (H2) was calculated to be 32.41 and 9.92 mass %, respectively. The value for milled sample (M2) was 32.77 and 8.94 mass %, respectively. The mole ratio of magnesium to aluminum was 3.62, and 4.07 for H2 and M2, respectively. This was lower than the theoretical mole ratio (4.55). The similarity of the recorded data over three different points on both samples indicates a homogenous microstructure.

2.3.3. Conclusions

This research section provides a comparative study of structural parameters for chloride intercalated HT as a function of contour ion concentration prepared by MC and hydrothermal methods. The two methods prepared a product with similar structural characteristics. The formation and structural features of Mg-Al-Cl-LDH were influenced by contour ion concentrations (0.12, 0.18, 0.3, and 0.42). Based on the phase analysis, chloride intercalated HT with appropriate purity was formed in the midrange contour ion concentration. The interlayer spacing of HT obtained from both procedures decreased as the ion content increased. Microscopic evaluations showed platelet structures of Mg-Al-Cl-LDH samples with greater mean particle size for the hydrothermal samples when compared with the milled ones. The product with high crystallinity degree was obtained from the hydrothermal method. This product can be used as a promising LDH for biomedical application especially for gene delivery. Mechanochemistry as a facile and simple method can be utilized for the mass production of Mg-Al-Cl-LDH with an acceptable crystalline phase.

2.4. Sulfate intercalated hydrotalcite

Sulfate intercalated Mg-Al layered double hydroxides (Mg-Al-SO₄-LDH) was successfully prepared by the one step mechanochemical activation method. From phase analysis, product with high purity was obtained after 60 min milling. Results demonstrated that the structural features of Mg-Al- SO₄-LDH were affected by milling time (30-900 min). Microscopic observations and elemental analysis are reported in this part.

2.4.1. Materials and experimental procedure

Magnesium chloride (99 %, ACROS), Aluminum chloride (99 %, ACROS), Sodium hydroxide pellets (97%, ACROS), and Sodium sulfate (Merck) were purchased and used without further purification. To synthesize Mg_{0.8}Al_{0.2}(OH)₂(SO₄)_{0.1}, the desired amounts (2 g) of MgCl₂, AlCl₃, Na₂SO₄ and NaOH were milled at different milling times (30, 60, 300, 600, and 900 min) in a high energy ball mill utilizing hardened chromium steel vials under air atmosphere. The weight ratio of ball-to-powder (BPR) was 10:1. The powders were washed three times with deionized water (20 ml) on a paper filter, and were dried in an oven at 80°C for 1h. The final composition was adjusted according to the following reaction (R4):



2.4.2. Result and discussion

2.4.2.1. XRD analysis

Fig. 27 presents the XRD patterns, interlayer spacing (d), lattice constants (a , and c), and unit cell volume of the samples as a function of milling time (30-900 min). Based on Fig. 27a, the main products of 30 min milling were Brucite and HT. The presence of Brucite indicates that the mechanochemical reaction was not completed. Brucite content almost vanished with increasing of milling time up 60 min when a pure phase composition of sulfate intercalated HT was formed. This trend continued for the 300 min milled specimen with slight increase in peaks intensity of HT and a partial trace of Periclase (MgO). HT decomposed slightly as the milling time increased. Further increase in the milling time up to 900 min led to further sharpening of the diffraction peaks of Periclase, which is believed to be the result of more decomposition of HT. All sharp peaks corresponding to sulfate intercalated HT were shifted gradually toward lower d spacing owing to the rise of the unit cell volume of HT and the presence of sulfate ions instead of carbonate ions. The interlayer spacing (d) of milled samples was determined by averaging the basal peaks according to the equation (I). Based on Fig 27b, the basal spacing between layers of $Mg_{0.8}Al_{0.2}(OH)_2(SO_4)_{0.1}$ was influenced by milling time so that it increased from 7.828 ± 0.001 to 7.942 ± 0.002 Å (30-600 min) and decreased to 7.878 ± 0.001 for the 900 milled sample. The change from tetrahedral SO_4^{2-} to trigonal planar CO_3^{2-} contributes to this expansion. The lattice parameters (a , and c) have been calculated from the equation (IV) for two Miller's planes of (003) and (110). The unit cell volume of samples was computed using the equation (V).

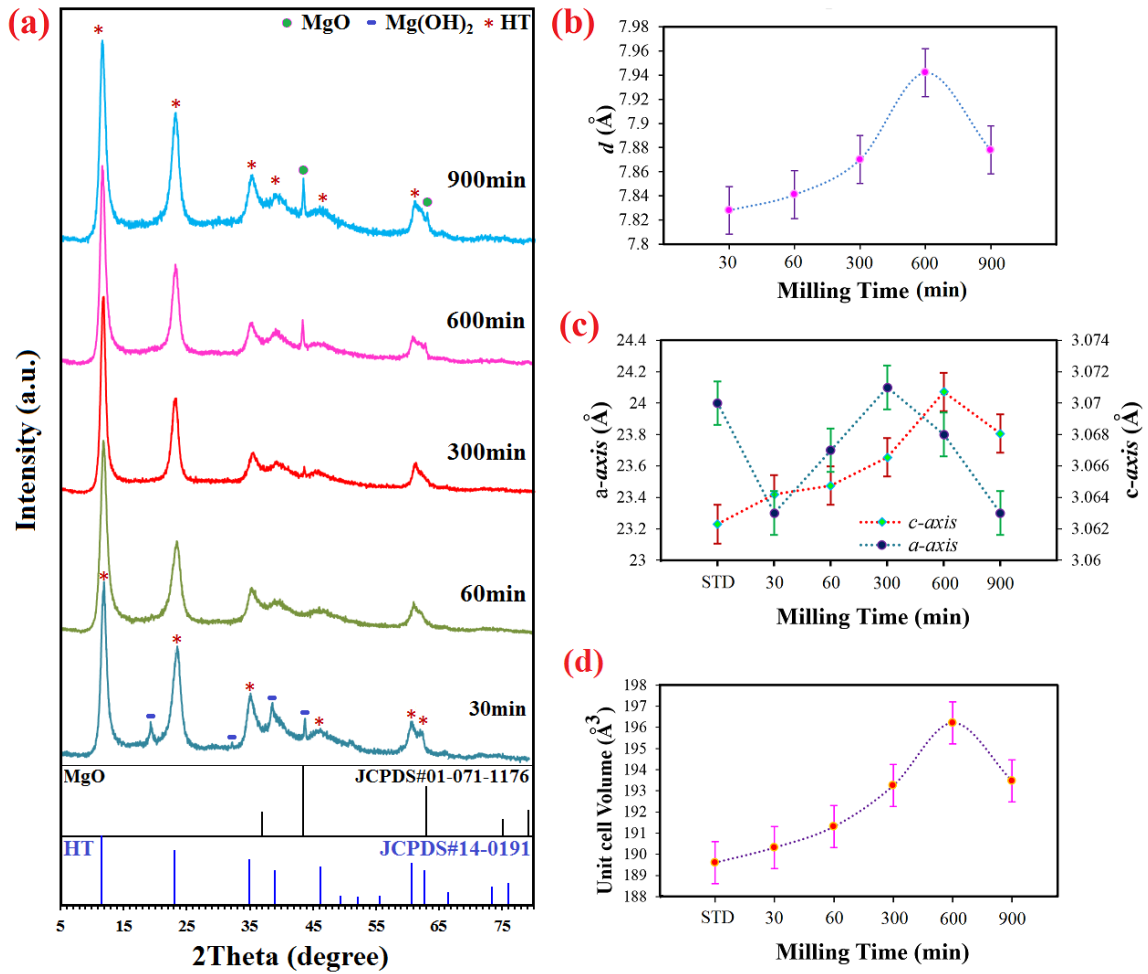


Fig. 27 (a) XRD patterns, (b) interlayer spacing, (c) lattice parameters and (d) the unit cell volume of the milled samples as a function of milling time (30-900 min).

Fig. 27c and d exhibits the lattice constants and unit cell volume of milled nanopowders as a function of milling time. From the standard data of HT (JCPDF#14-0191), a -axis values were 3.07Å, and c -axis values were 23.23Å, respectively. The comparison study of the data indicates that the a -axis and c -axis values were different. It shows an overall upward trend for milled samples with some fluctuation as milling time increased (30-900 min). According to Fig. 27d, the unit cell volumes of the milled powders increased slowly from 190.32 ± 0.01 to 196.22 ± 0.02 (Å³) as milling time rose (30-600 min) and declined to 193.48 ± 0.02 Å³ for the 900 min milled sample. The

differences in values for unit cell volume resulted from increase in the c axis values, rather than the a axis. This could be attributed to the change a tetrahedral arrangement of sulfate ion compared to trigonal planar configuration of carbonated ion. The structural features of the mechanothesized Mg-Al-SO₄-LDH were affected by the milling time.

2.4.2.2. FT-IR analysis

The FT-IR spectra of samples as a variation of milling time were displayed in [Fig. 28](#). The spectrum of 30 min milled sample exhibited a narrow weak band corresponding to the stretching vibrations of Brucite (3700 cm⁻¹), a broad Hydroxyl band (ν_2) at 3475 cm⁻¹, a weak water band at 1636 cm⁻¹, and two bands at 556 and 448 cm⁻¹ (due to metal-oxygen bond in the Brucite like lattice) [52]. Two weak bands at around 2920 and 2852 cm⁻¹ (the shoulder of graph) were possibly owing to the hydrogen bonded (OH) stretching of intercalated water molecule [53]. The absorption bands at around 1383 (ν_3), 870 (ν_2), and 631 cm⁻¹ (ν_4) shows the stretching vibration of CO₃²⁻, which is owing to the absorption of CO₂ from the air [54]. The FTIR spectra of Mg-Al-SO₄-LDH at 1066 cm⁻¹ were attributed to the bending mode of interlayer sulfate ions [53]. With increasing of milling time up to 60 min, the Brucite band completely disappeared indicating the reaction of magnesium hydroxide with the other reagents. This supported the results obtained from XRD data.

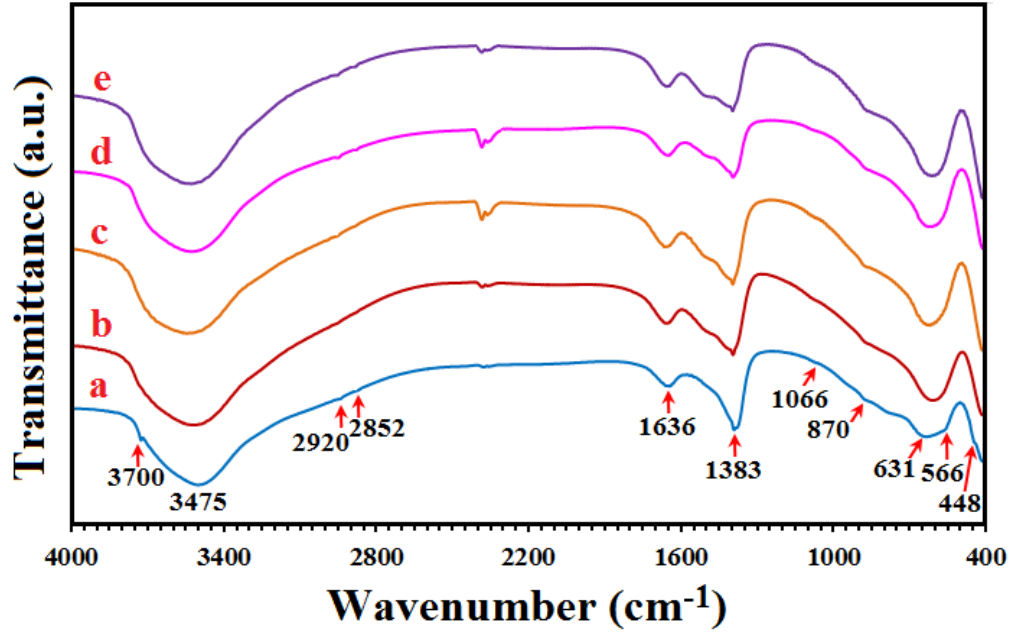


Fig. 28 FT-IR spectra of milled specimens (Mg-Al-SO₄-LDH) as a variation of milling time; (a) 30, (b) 60, (c) 300, (d) 600, and (e) 900 min.

2.4.2.3. Morphological characterization

The FESEM and TEM images of 60 min milled sample (Mg_{0.8}Al_{0.2}(OH)₂(SO₄)_{0.1}) are shown in Fig. 29. According to Fig. 29a, the product had a rounded platelet structure composed of several fine particles. Pursuant their relatively large specific surface area of particles, the product had high tendency to agglomeration. During milling, the system included one ductile constituent (NaOH) and three brittle components (Na₂SO₄, MgCl₂ and AlCl₃). Sodium chloride was formed owing to the hygroscopic nature of Halite, and followed by the formation of a ductile–brittle system. With continuous milling, both ductile and brittle particles got further refined and the interlamellar spacing dropped. Ultimately, product with the layered structure was developed when equilibrium between fracturing brittle particles by trapping and ductile constituents by work hardening was established. From EDS spectrum of 60 min milled specimen, the main elements were

oxygen, magnesium, aluminum, carbon, and sulfur. In addition, no other stable contaminants were recorded. Based on TEM image in Fig. 29b, smaller particles were mostly rounded platelet shape with a mean size of around 50-100 nm.

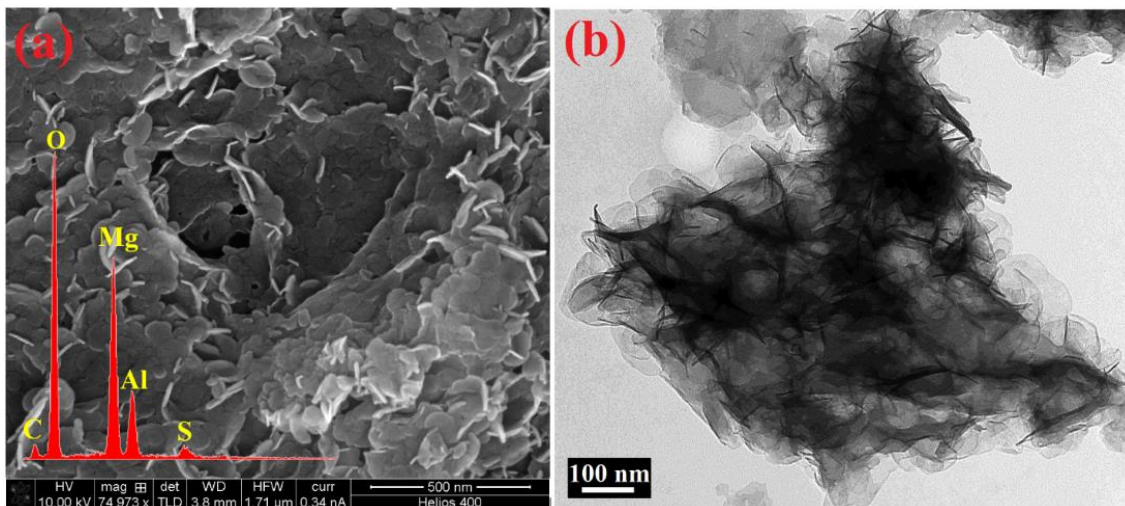


Fig. 29 Morphological features of 60 min milled sample (Mg-Al-SO₄-LDH): (a) FE-SEM image & EDS spectrum and (b) TEM image.

2.4.2.4. Thermogravimetric analysis

Fig. 30 displays the differential thermogravimetric analysis (DTGA) disclosing the degradation mechanism under the recording conditions for 60 min milled sample (Mg_{0.8}Al_{0.2}(OH)₂(SO₄)_{0.1}). As reflected in DTGA trend, the thermal decomposition process covers two stages, which were ascribed to processes like the structural dehydroxylation, and the removal of the interlayer anions. The first mass loss of ~ 2.9% occurred between around 133°C and 215°C which may be contributed to the elimination of the interlamellar water but not high enough for the removal of the carbonate anions or hydroxyl groups. From approximately 215°C to 514°C, the second mass loss was the largest occurring at 388°C accounting for 31.7%, which associated to the interlayer anions loss. In this stage, decarbonation and dehydroxylation were proposed to have been

removed. It is worthy to note that the conventional HTs having carbonate anions had a decomposition temperature of 310°C [55]. However, the growth in decomposition temperature may demonstrate that sulfate anions have been successfully intercalated in LDH. From 514°C, there is a constant residual mass associated to the formation of the magnesium and aluminum oxide, corresponding to ~ 40% of the initial mass.

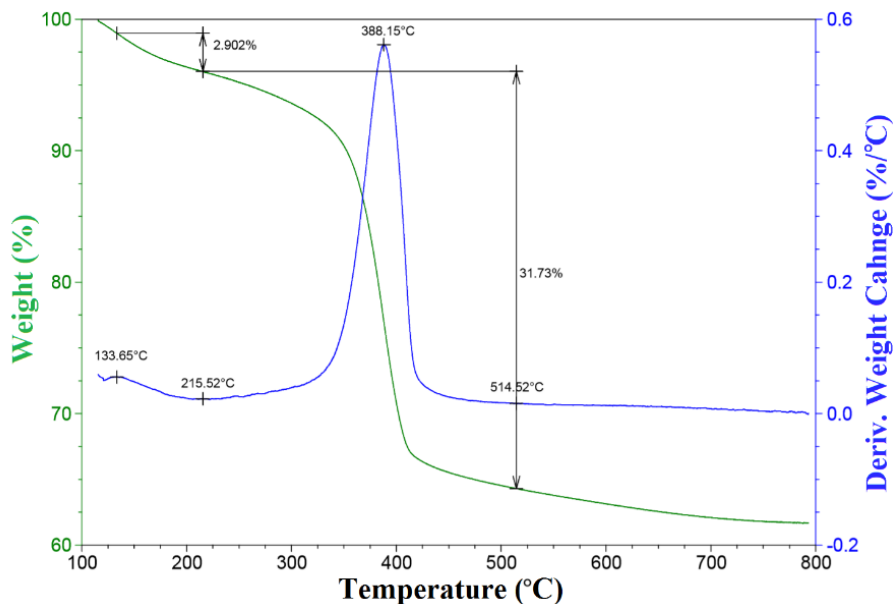


Fig. 30 DTGA of 60 min milled sample as a function of temperature.

2.4.3. Conclusions

In this report, one-step mechanochemical synthesis of Mg-Al-SO₄-LDH was investigated. Results showed that the structural features of product affected strongly by milling time (30-900 min) so that the interlayer space of resulting solid was expanded as milling time increased. Based XRD and FTIR spectra, a pure phase composition of sulfate intercalated HT was formed after 60 min milling. Microscopic observations showed a rounded platelet structure of product containing small particles with mean lateral size of 50-100 nm. Based on the DTGA data of Mg-Al- SO₄-LDH, two mass loss

characteristics events of the thermal decomposition of the LDH were observed which indicates that sulfate anions have been successfully intercalated in LDH structure.

Finally, the mechanothesized Mg-Al-SO₄-LDH with nanosized particles can be useful as a carrier and reservoir for target delivery and water treatment.

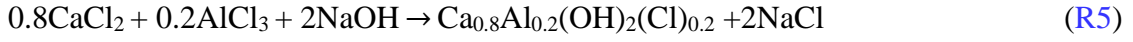
3. HYDROCALUMITE

Hexagonal-shaped hydrocalumite (Ca/Al Layered Double Hydroxide: Ca-Al-LDH) with proper crystallinity and purity was successfully synthesized by one-step mechanochemistry method within only 30 min. The structural features and morphological characteristics of milled powders have been investigated for a variety of milling times and ion substitutions. Products were characterized by XRD, FTIR, FESEM, EDS, XRF, TEM, and elemental mapping analysis. The Rietveld refinement of milled samples for different ion substitutions has been conducted and reported here. Detailed study of this phase behavior and structural trends was also scrutinized. Microscopic observations illustrated the hexagonal platelet-like shape of hydrocalumite powders with lateral dimension of 100 to 200 nm. Moreover, the thermal decomposition details of Ca/Al-Cl-LDH were reported.

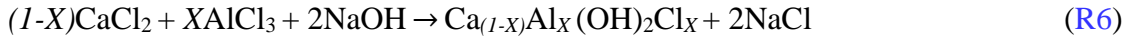
3.1. Experimental procedure

Calcium chloride (99 %, Sigma-Aldrich), Aluminum chloride (99 %, ACROS), and Sodium hydroxide pellets (97%, ACROS), were purchased and used without further purification. To prepare Ca-Al-LDH, the desired amounts of CaCl₂, AlCl₃, and NaOH were milled at different milling times (30, 60, 180, and 300 min) in a high energy ball mill using hardened chromium steel vials under air atmosphere. The weight ratio of ball-to-powder (BPR) for all specimens was 10:1. The powders were washed three times with deionized water (20 ml) on a paper filter, and then were dried under oven at 60°C for 1h. The samples milled at different milling time were labeled as S1, S2, S3, and S4,

respectively. The final composition for different milling time was adjusted according to the following reaction (R5):



The designed degree of substitution of chlorine was designated by the x value in the general formula of $\text{Ca}_{1-x}\text{Al}_x(\text{OH})_2\text{Cl}^-_x$, where x values were chosen equal to 0.1, 0.15, 0.2, 0.25, 0.3, 0.35, and 0.4, so the milled nanopowders were labeled as S11, S22, S33, S44, S55, S66, and S77, respectively. Thus, the final composition for diverse ion substitutions was adjusted based on the following general reaction (R6):



The specimens were scanned from 5 to 75 degrees 2θ at a step size of 0.03 degrees. The XRD spectra were compared to standards compiled by the Joint Committee on Powder Diffraction and Standards (JCPDS) involving card #31-0245 for Hydrocalumite. The structural refinements were carried out in the angular range 5–75 (2θ) using the Reflex module in Materials Studio, version 6.0, by Accelrys. In the Rietveld algorithm [56], the parameters being refined were optimized in order to minimize the weighted profile R factor R_{wp} (R7):

$$R_{wp} = \sqrt{\sum_i w_i |I_{obs}(\theta_i) - I_{cal}(\theta_i)|^2} / \sqrt{\sum_i w_i |I_{obs}(\theta_i)|^2} \quad (\text{R7})$$

Where $w_i = 1/I_{obs}(\theta_i)$.

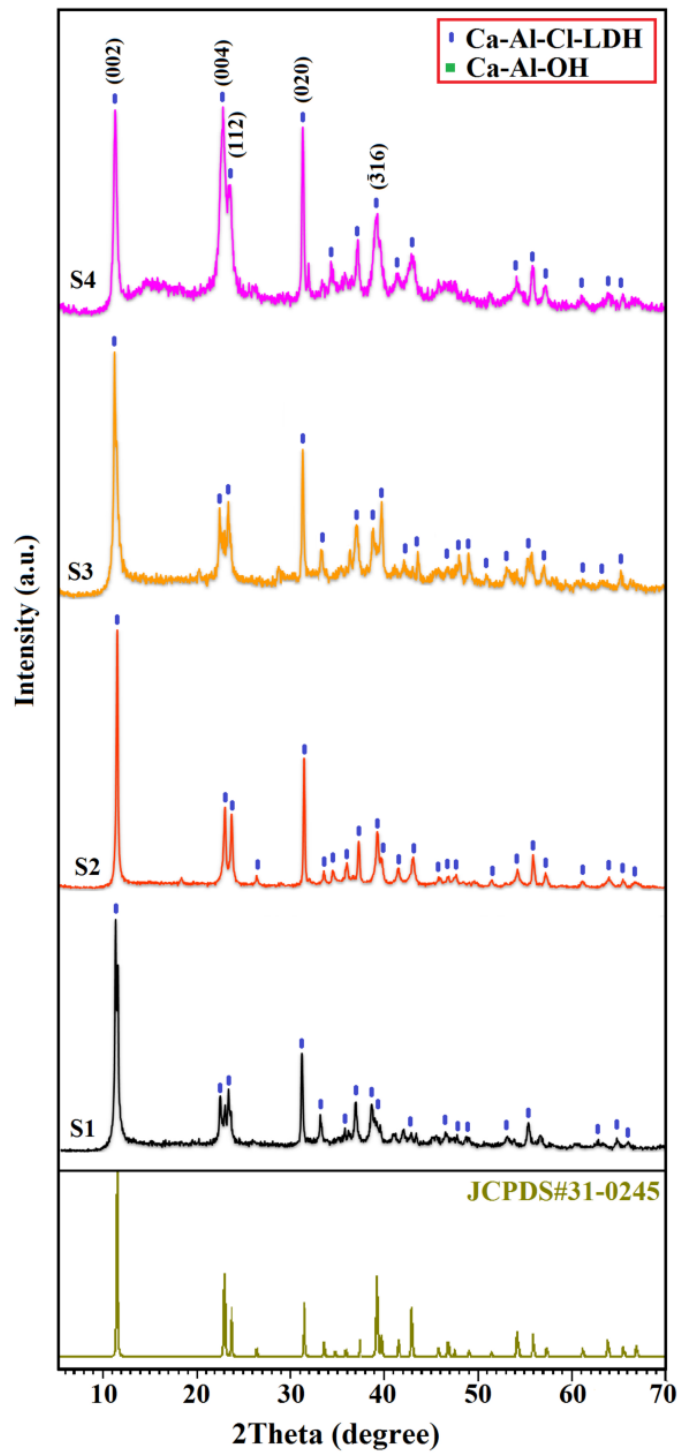


Fig. 31 XRD patterns of specimens (Ca-Al-LDH) milled at different milling time (30=S1, 60=S2, 180=S3, and 300=S4).

3.2. Result and discussion

3.2.1. XRD analysis

3.2.1.1. Effect of milling time

Fig. 31 shows the XRD profiles of samples as a function of milling time (30, 60, 180, and 300). HC displayed peaks corresponding to (200), (004), (112), (020), and ($\bar{3}16$) crystal plane. Based on Fig. 31, the main product of 30 min milling was in excellent agreement with the standard HC. With increasing of milling time up to 60 min, a well-crystallized Ca-Al-LDH with higher peaks intensity was formed. This trend continued for the 180 min milled specimen with slight decrease in peaks intensity of HC. Further increase in the milling time up to 300 min led to further decrease of the dominant peaks particularly for (002) plane. As is evident from the magnified 3D XRD profiles ($2\theta = 5\text{--}35^\circ$) in Fig. 32, with increasing milling time, both sharpness and intensity of the LDH-derived XRD peaks decreased and shifted towards larger d spacings (i.e. lower 2θ). This effects could be explained on the basis of mechanically induced amorphization, which was accompanied by a significant change in lattice imperfections.

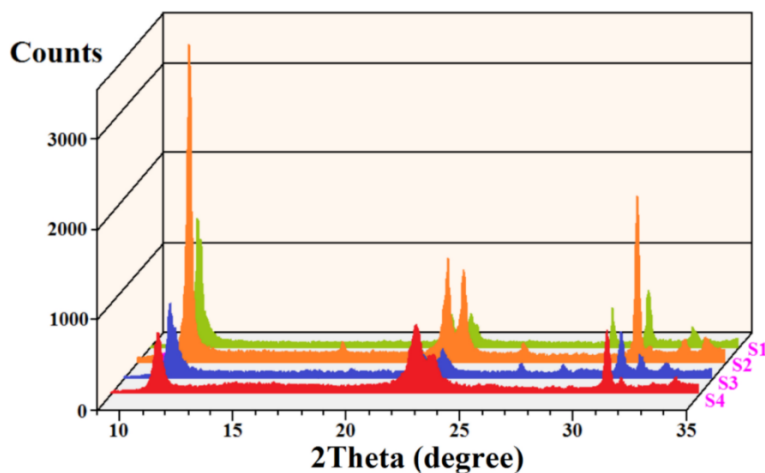


Fig. 32 The magnified 3D XRD profiles ($2\theta = 5\text{--}35$) of samples (S1, S2, S3, and S4).

Based on Fig 33, the basal spacing between layers of Ca-Al-LDH was strongly influenced by milling time so that it declined from 7.991 ± 0.001 (S1) to 7.833 ± 0.002 (S2) and then rose to 7.975 ± 0.001 and 8.04 ± 0.001 for S3 and S4, respectively. The presence of trigonal planar carbonate ion in interlamellar space instead of chloride ion may also contributes to this expansion [57]. This shows that the finding of optimum milling time to obtain carbonate free HC is essential.

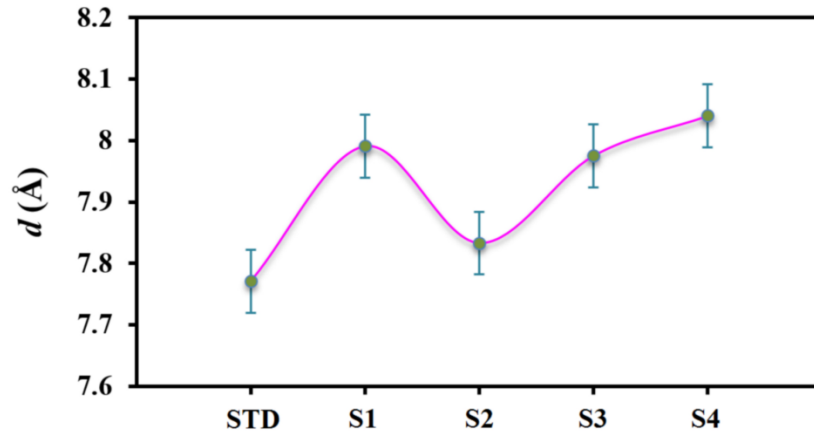


Fig. 33 The interlayer spacing of specimens (Ca-Al-LDH) milled at different milling time (S1, S2, S3, and S4).

3.2.1.2. Effect of ion substitution

Fig. 34 shows the XRD patterns of milled samples (Ca-Al-LDH) with various amount of ion substitutions (S11, S22, S33, S44, S55, S66, and S77). The diffractogram was assessed with Philips X'Pert High Score software to search for the phases of milled samples. As can be seen, there is a close structural similarity between all the samples from the nearly identical diffraction patterns, which can be corroborated the substitution of Ca^{2+} by Al^{3+} in the HC lattice and Cl^- in interlamellar space. Based on these profiles,

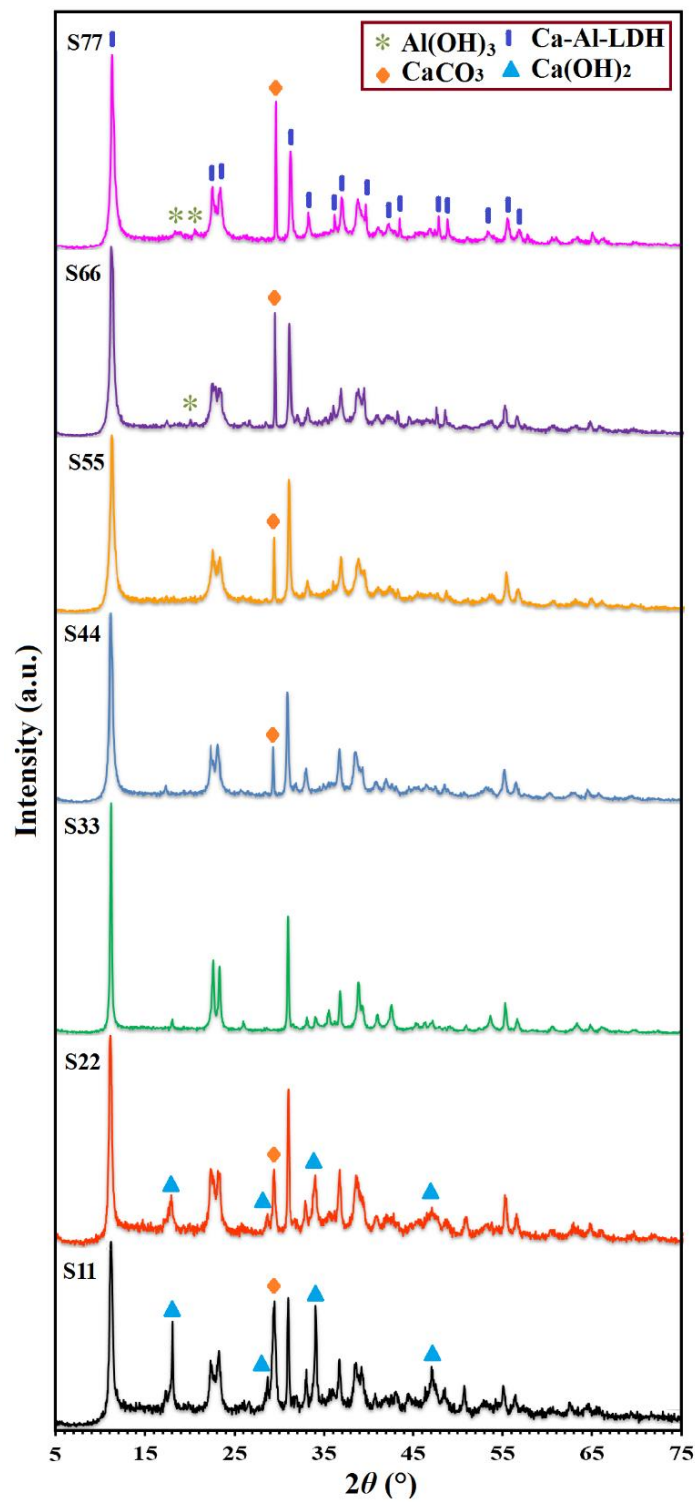


Fig. 34 XRD patterns of Ca-Al-LDH with various ion substitutions (S1=0.1, S2=0.15, S3=0.2, S4=0.25, S5=0.3, S6=0.35, and S7=0.4).

all the main peaks belonged to the characteristic peaks of Ca-Al-LDH. The main representing peaks of HC powders are as follows: (0 0 2) plane at $2\theta = 11.38^\circ$, (0 0 4) plane at $2\theta = 22.88^\circ$, (1 1 2) plane at $2\theta = 23.63^\circ$, (0 2 0) plane at $2\theta = 31.33^\circ$, ($\bar{3}$ 16) plane at $2\theta = 39.08^\circ$, ($\bar{2}$ 0 8) plane at $2\theta = 42.77^\circ$, ($\bar{2}$ 2 8) plane at $2\theta = 53.95^\circ$, and (0 1 9) plane at $2\theta = 55.62^\circ$. At low Al substitutions (S11 and S22) portlandite (calcium hydroxide) and HC co-exist, while at very high Al substitutions (S66 and S77) Gibbsite appears as additional phase with HC. A small peak at around $2\theta = 29.37^\circ$ corresponding to calcite were found as a by-product in all samples except in midrange (S33). The presence of calcite in high and low Al replacements can be attributed to the absorption of atmospheric carbon dioxide during the milling stage. In this case, the high intensity of the strongest peak ascribed to calcite [(1 0 4) plane] serves as proof that there is an incompleteness substitution due to the intrinsic structural constrains of HC. It has been demonstrated that calcite as secondary phase was dominant along with HC prepared via other procedures such as microwave [9], self-dissolved re-precipitation [58], and co-precipitation [59] processes. However, the absence of calcite in midrange can be a promising candidate for production of pure Ca-Al-LDH via mechanochemistry method.

Fig. 35 presents the basal spacing of milled samples as a function of ion substitutions. As is evident from Fig. 35, the basal spacing between layers of Ca-Al-LDH was strongly influenced by ion replacements (X) so that it shows a slight ascending trend from low ion substitution 7.955 ± 0.001 (S11) to high ion replacement 7.991 ± 0.002 (S77) with a reduction in midrange 7.833 ± 0.001 (S33), which is close to standard value 7.771 ± 0.001 (STD). This expansion at high ion contents may also contributes to the presence of trigonal planar carbonate ion in interlamellar space along with chloride ion as

the peak intensity of calcite was also sharpened [57]. This indicates the significance of finding optimum ion substitutions in HC structure.

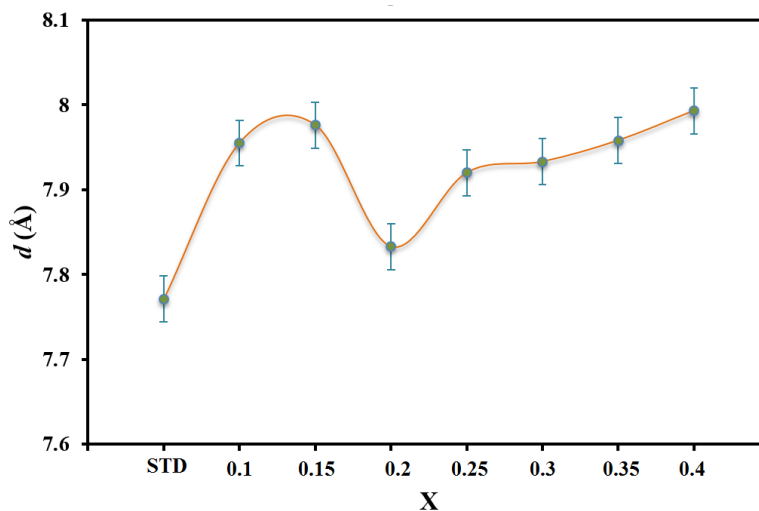


Fig. 35 The interlayer spacing of Ca-Al-LDH as function of ion substitutions.

3.2.1.3. Rietveld Refinement

The structural refinements were executed by the Rietveld method using Materials Studio as well as Crystallography Open Database (COD). Peak shapes were modeled on a Thompson-Cox-Hastings distribution, and an asymmetry parameter was refined. All the parameters were fixed according to the literature values, and they were all refined subsequently during the successive refinement cycles. Fig. 36 illustrates the experimental and refined XRD patterns of milled samples (S11-S77). The “+” red marks represent the measured diffraction data (Experimental). The blue solid curves indicate the calculated diffraction data (Simulated) and the green vertical lines display the positions of the simulated diffraction patterns. The black solid line denotes the deviation between the

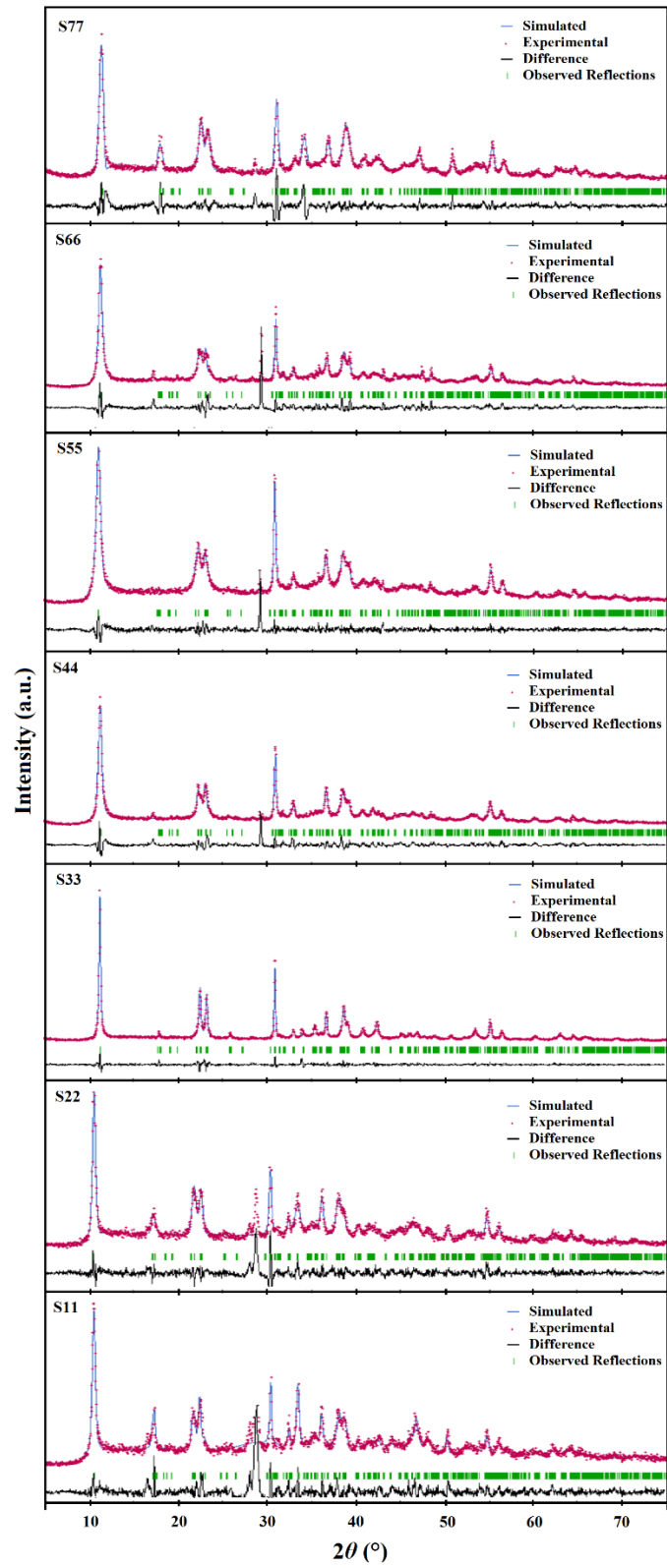


Fig. 36 Rietveld refinement plots of Ca-Al-LDH as function of ion substitutions.

measured and calculated values. After refining all necessary parameters with sufficient cycles, each peak indicates a good fit as reflected by small difference between calculated and experimental spectra. There is no impurity phase in midrange sample (S33) indicating a good single-phase of Ca-Al-LDH. All data related to profile R -factor (R_p) and weighted profile R -factor R_{wp} are presented in Table 3. The values of R factors are found to be large. Similar high values of R factors for the nanostructured materials have been reported by the former studies [60]. This effect is owing to the large ratio of surface to volume atoms. Indeed, the diffuse scattering becomes significant at the nanoscale while Bragg scattering gets diminished, which leads to decline in crystallinity and large R factors [61].

Table 3. R factors obtained from the Rietveld refinement of Ca-Al-LDH.

Sample	Ion (X)	R_{wp}	R_p
S11	0.1	19.23	13.56
S22	0.15	16.43	11.87
S33	0.2	10.49	7.94
S44	0.25	13.35	9.84
S55	0.3	11.02	7.48
S66	0.35	16.34	10.99
S77	0.4	12.86	10.08

Fig. 37 illustrates the refined lattice constants and unit cell volume for samples S11, S22, S33, S44, S55, S66 and S77 based on the XRD-Rietveld analysis. Fig. 37a shows the variation of the a -axis and c -axis parameters of the HC phase with ion substitutions. From the standard data of HC, a -axis, and c -axis values were 9.853\AA , and 16.898\AA , respectively. The comparison study of those data reveals that the a -axis and c -axis values were different; however, it shows an overall slight descending trend as ion

contents (X) increased from 0.1 to 0.4. Note that b -axis values from XRD-Rietveld analysis have been obtained around $\sim 5.76 \pm 0.04 \text{ \AA}$ for all samples, which was close to standard one 5.72 \AA . The unit cell volume of milled samples can be calculated using the following equation (VII) [62]:

$$V = (abc)\sin\beta \quad (\text{VII})$$

According to Fig. 37b, with increasing of X content from 0.1 to 0.4, the unit cell volume of milled samples decreased gradually from $913.12 \pm 0.01 \text{ \AA}^3$ for S11 to $897.63 \pm 0.02 \text{ \AA}^3$ for S77, respectively. It is clear that the differences in values of unit cell volume resulted mainly from increases in the c -axis values, rather than a -axis values. These findings demonstrate that the structural characteristics of the mechano-synthesized Ca-Al-LDH were affected considerably by ion substitutions.

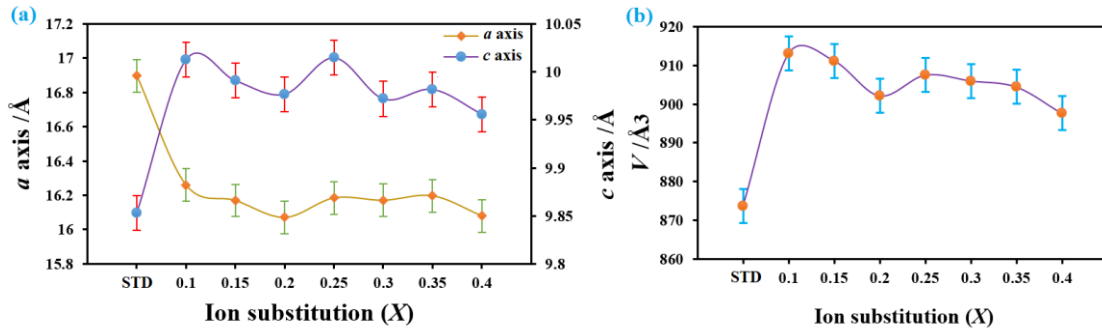


Fig. 37 The refined lattice constants (a) and unit cell volumes (b) of Ca-Al-LDH as a variation of ion substitution.

3.2.2. FTIR analysis

3.2.2.1. Effect of milling time

Fig. 38 displays the FT-IR spectra of samples as a function of milling time. The spectrum of 30 min milled sample exhibited two bands corresponding to the stretching vibrations of AlO-H at 3640 cm^{-1} , and a Hydroxyl band (ν_2) at 3492 cm^{-1} present in the

inorganic main layers. From 3350 to 3650 cm^{-1} , the OH stretching vibrations of water can be observed as a broad band. Two weak bands at around 2918 and 2843 cm^{-1} (the shoulder of graph) were possibly owing to the hydrogen bonded (OH) stretching of intercalated water molecule [63]. A weak water band at 1636 cm^{-1} came from deformation vibration of water molecule [52]. The absorption bands at around 1422 (ν_3), and 873 (ν_2), shows the stretching vibration of CO_3^{2-} , which is owing to the absorption of CO_2 from the air [64]. The band below 800 cm^{-1} were attributed to M–O vibrations (M = Ca or Al). Moreover, the bands at 786 and 710 cm^{-1} correspond to the characteristic vibrations of hydrotalcite [65]. The results demonstrate that the milling time affected intensity and the broadening bands supporting outcomes obtained from XRD profiles.

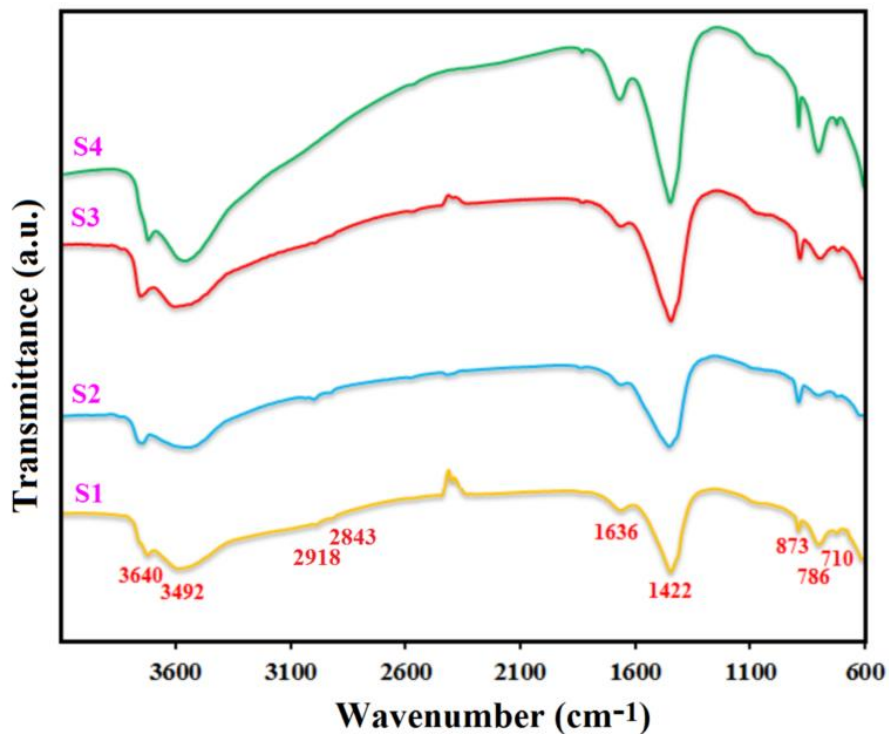


Fig. 38 FT-IR spectra of milled specimens (S1, S2, S3, and S4)

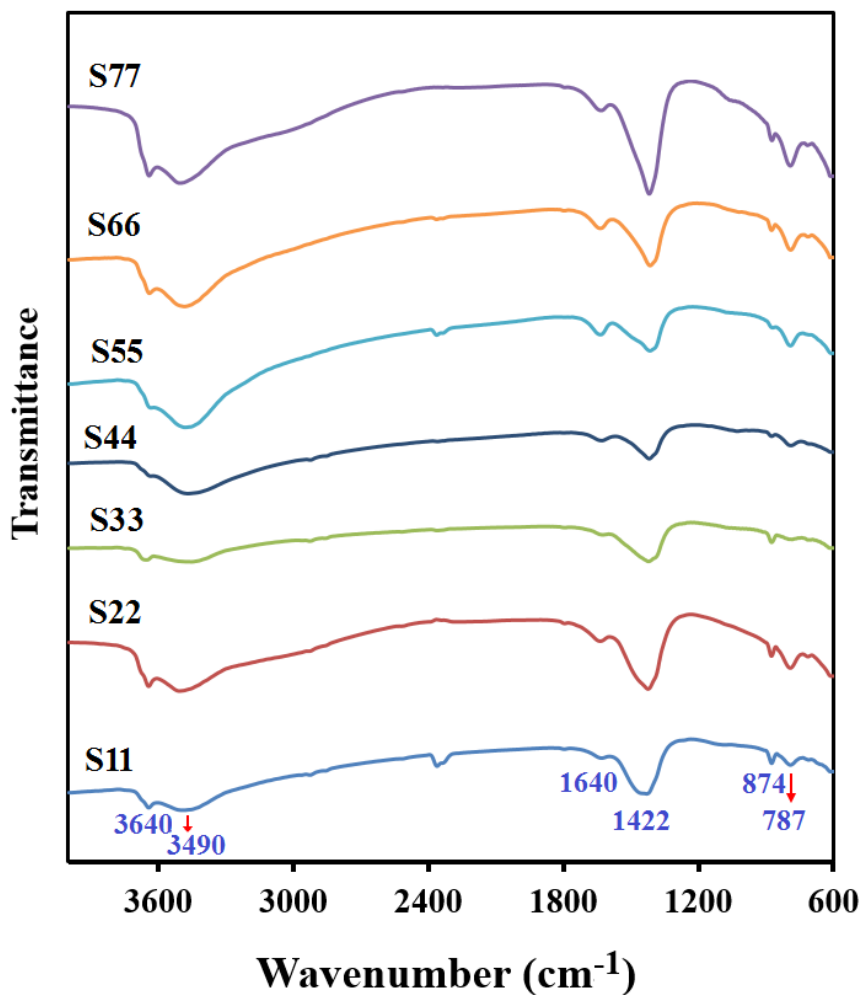


Fig. 39 FT-IR spectra of Ca-Al-LDH as variation of ion substitutions (S11=0.1, S22=0.15, S33=0.2, S44=0.25, S55=0.3, S66=0.35, and S77=0.4).

3.2.2.2. Effect of ion substitution

The FT-IR spectra of samples as a variation of ion substitution are displayed in Fig. 39. From all spectra, the representing bands of HC were recognized in all cases. The characteristic bands for AlO–H and Hydroxyl band (ν_2) appeared at 3640 cm^{-1} and 3490 cm^{-1} , respectively. The OH stretching vibrations of water can be also observed as a broad band from $3350\text{ to }3650\text{ cm}^{-1}$. Moreover, a weak water band at 1640 cm^{-1} can be resulted from deformation vibration of water molecule [52]. The symmetric stretching modes of

CO_3^{2-} were observed at around 1422 cm^{-1} (ν_3), and 874 cm^{-1} (ν_2) confirming the absorption of CO_2 from the atmosphere during milling process [64]. The results were in good agreement with XRD data. The band around 800 cm^{-1} was associated to M–O vibrations (M = Ca or Al). Besides, the characteristic vibration bands of anionic layered double hydroxide can be detected at 874 and 787 cm^{-1} [65]. The results demonstrate that the various ion contents impacted the intensity and broadening bands as well.

3.2.3. Morphological characterization

The FESEM and TEM images of 60 min milled sample Ca-Al-LDH are shown in Fig. 40. From Fig. 40a, the product shows a hexagonal platelet structure composed of some fine particles. The relatively large specific surface area of the particles, resulted in the product having high tendency to agglomeration. This phenomenon commonly occurs in a three-step processes namely; *Rittinger*, *aggregation*, and *agglomeration* stage [66]. It is most likely that the mechanochemical reactions and structural changes mainly occur at the last stage owing to chemical bonding of fine particles [57]. The mechanics for MC of HC may involve first forming a lamellar structure of the two metals (Ca, and Al), that on continued milling, become finer and finer, and finally alloying occurs via diffusion. Based on TEM image in Fig. 40b, a well-shaped layered structure with the lateral dimension of 100-200 nm can be observed. The morphology obtained by this method is similar to the other procedures that prepared through co-precipitation and hydrothermal methods [59].

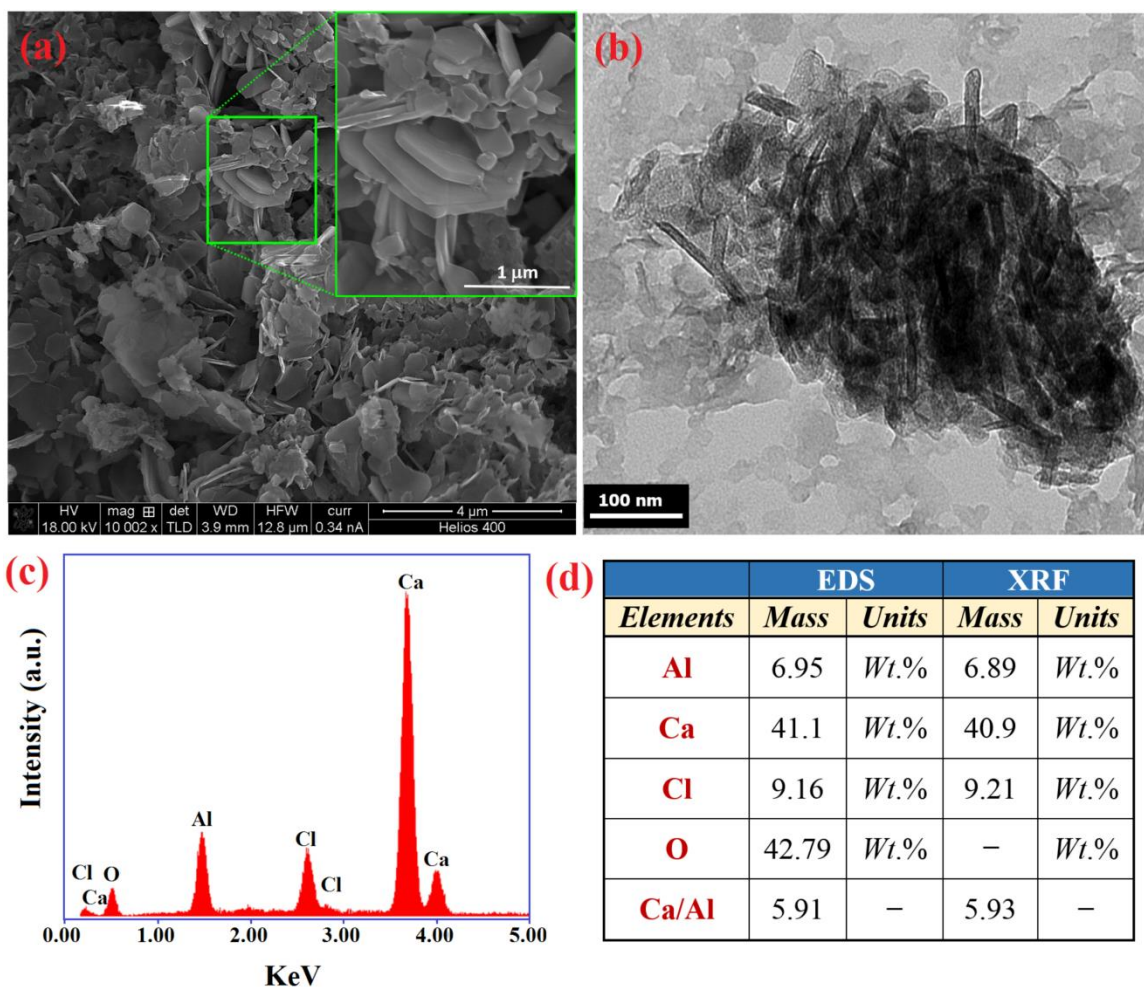


Fig. 40 Morphological features and chemical composition of 60 min milled sample (Ca-Al-LDH): (a) FE-SEM, (b) TEM images.

Fig. 40c and d exhibit EDS and XRF spectra of 60 min milled sample. From the obtained data, the main components of the sample were oxygen, calcium, aluminum, and chlorine. Since sodium chloride was the only by-product of milled sample, and was washed from the sample, no other chemically stable contaminants were found. The total amount of calcium and aluminum present in Ca-Al-LDH from both techniques were detected similarly, which are comparable with the accepted values. The mole ratio of calcium to aluminum was also achieved 5.91 by EDS and 5.93 by XRF, which were very close to actual mole ratio (5.94). The results illustrate that the composition and structure

of chlorine incorporated Hydrocalumite were also very stable. Fig. 41 shows elemental mapping analysis of 60 min milled sample (Ca-Al-LDH). An appropriate spatial distribution of elements (Ca, Al, O, and Cl) was detected in elemental mapping images, indicating the formation of a homogenous microstructure after 60 min of milling.

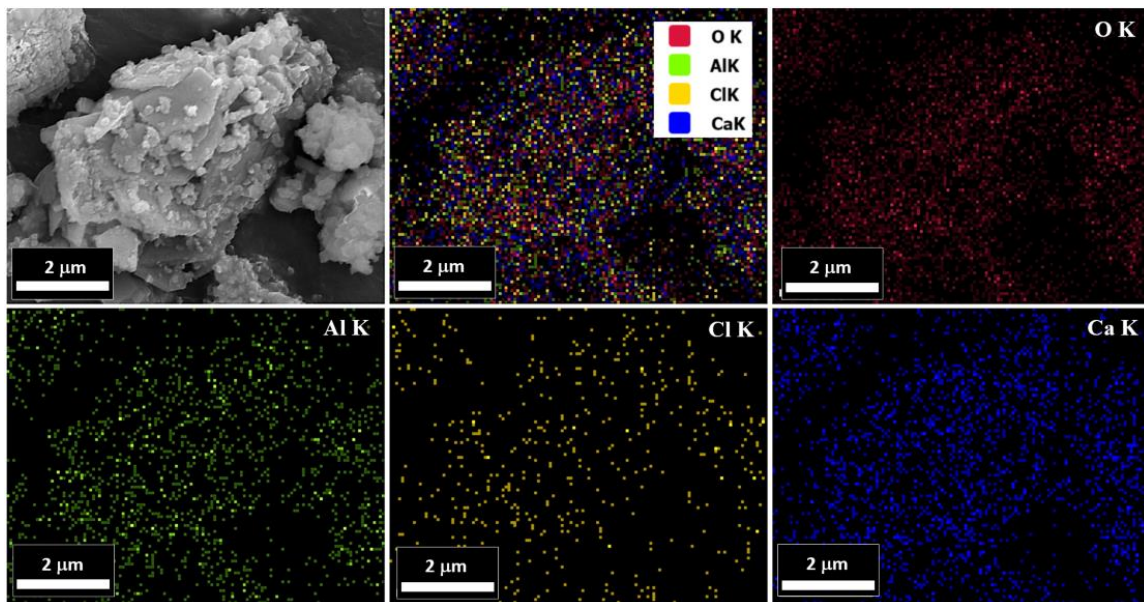


Fig. 41 The elemental mapping analysis of 60 min milled sample (Ca-Al-LDH).

3.2.4. Thermogravimetric analysis

Fig. 42 shows the differential thermogravimetric analysis (DTGA) of 60 min milled sample (Ca-Al-LDH) disclosing the degradation mechanism under the recording conditions from room temperature to 800°C. Based on DTGA graph, the thermal decomposition process covers three stages, which were ascribed to processes like elimination of physisorbed water, the structural dehydroxylation, and the removal of the interlayer anions. The first mass loss of 4.35% occurred between around 53°C and 159°C which may be contributed to the elimination of physically bound absorbed water and/or the dissociation some of hydrated reactants, which was formed during milling or washing

process. The second region from 159°C to approximately 370°C, corresponding to a mass loss of 12.3% associated to the interlamellar water loss. The final and largest decomposition phase from 370°C to 751°C with a mass loss of 25.7% attributed to the total anion decomposition and dehydroxylation of the HC lamellae, which is bonded mostly with Ca^{2+} [Ca-(OH)-Ca] and [Al-(OH)-Ca]. It is worthy to note that the conventional LDH having carbonate anions had a decomposition temperature of 310°C [55]. However, the reduction in decomposition temperature (~ 258°C) may demonstrate that chloride anions have been successfully intercalated in LDH. From 751°C and above, there is a constant residual mass associated to the formation of the calcium and aluminum oxide, corresponding to ~ 42.35% of the initial mass.

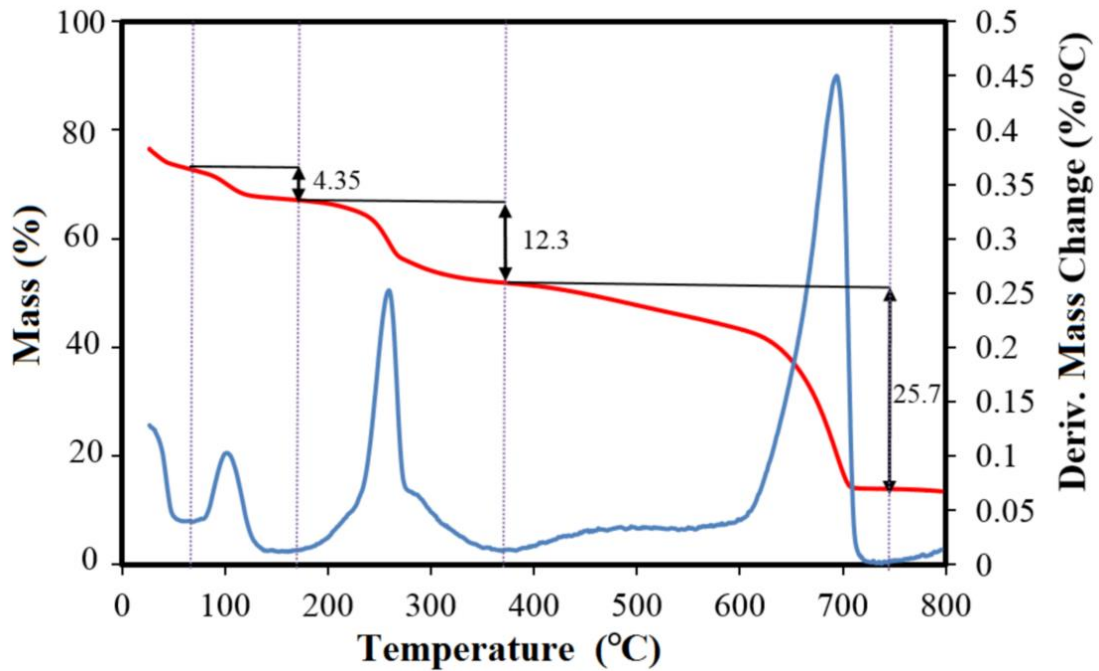


Fig. 42 DTGA of 60 min milled sample (Ca-Al-LDH) as a function of temperature.

3.3. Conclusions

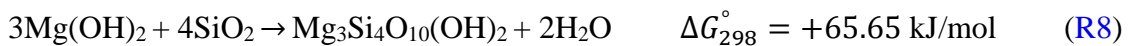
Rapid synthesis of mechanically induced hydrocalumite was investigated in this research section. Results showed that the structural characteristics of product affected strongly by milling time and ion substitutions. Based upon XRD and FTIR spectra, a pure phase composition of Ca-Al-LDH was formed after 30 min milling, however the product of 60 min milling showed higher crystallinity. Additionally, a pure phase composition of Ca-Al-LDH was formed at midrange ($X=0.2$). Microscopic observations displayed a hexagonal platelet structure of product containing fine particles with lateral dimension of 100-200 nm. From EDS and XRF spectra, no other chemically stable impurities were detected. From TGA data, three mass loss characteristics events of the thermal decomposition of Ca-Al-LDH were observed demonstrating the successful chloride intercalation in LDH structure. Finally, this rapid synthesis method improved the production efficiency of hydrocalumite, and could be applied in various industries.

4. TALC

In this chapter, the synthesis of talc using wet and dry mechanochemistry was investigated. Furthermore, the effect of subsequent autoclave treatment on the milled samples was also evaluated. The structural features and morphological characteristics of milled powders have been studied for a variety of milling times and different conditions. Products were characterized by XRD, FTIR, FESEM, EDS, TEM, and DTGA. Detailed study of the phase behavior and structural trends were also scrutinized. Moreover, the thermal decomposition details of talc were examined and reported.

4.1. Experimental procedure

Magnesium hydroxide (99 %, Sigma-Aldrich), and silica gel (99 %, Sigma-Aldrich), were purchased and used without further purification. To prepare Talc, the desired amounts of Mg(OH)₂, silica gel, and certain amount of water were milled at different milling times (0.5, 1, 5, and 10h) in a high energy ball mill using hardened chromium steel vials under air atmosphere. The weight ratio of ball-to-powder (BPR) for all specimens was 10:1. In order to take advantage of hydrothermal process in mechanical activator, water was used and the water to mixture (water and powders) ratio was kept around 0.286. An optimal ratio is one part of water per four parts of the mixture [67]. The samples milled at different milling time were labeled as T1 (0.5h), T2 (1h), T3 (5h), and T4 (10h), respectively. The final composition for different milling time was adjusted based on the following reaction (R8):



The certain amount of milled powders (0.5 g) for all samples was suspended in 15 ml deionized water and stirred in 50 ml beaker for about 10 min under constant vigorous stirring using a magnetic stirrer. Then, the slurry was poured in autoclave chamber (25 ml volume) and was kept in oven at 260°C for 12h. Finally, the slurry was poured on a paper filter, and then were dried under oven at 60°C for 1h. So the autoclaved products were labeled as T11, T22, T33, and T44, respectively.

4.2. Result and Discussion

4.2.1. XRD analysis

The Gibbs free energy change of R8 was calculated as +65.65 (kJ/mol) at the standard conditions (298.15 K and 1 atm) indicating a nonspontaneous process. This means that an outside action should introduce energy to drive the process. Thus, the above reaction hardly occurs unless both compounds are composed of very fine particles and form an ideal state of solid solution [68]. Therefore, talc is known to be synthesized by only a hydrothermal method, which required very high temperature and/or pressure [69].

Fig. 43 shows the XRD patterns of the mixtures milled for 10h with water (wet grinding), and without water (dry grinding). Based on dry grinding XRD profile, there are a large amorphous hump of silica and two small crystalline peaks corresponding to Fe due to excessive wear of balls and vials. This indicates that all compounds in the sample have transformed into amorphous or glassy phase after grinding for 10h. However, when a certain amount of water was added in the starting mixture, the peaks representative of talc have appeared. This indicates that high pressure and temperature may exist in a vial

and assist the mechanochemical activation process. It is interesting to note that the dry milling of brittle components like silicon does not raise the temperature [44]. In addition, the peaks related to Fe were not detected through wet grinding. The analogous results of wet grinding of hydrated calcium silicates were also obtained and reported [70].

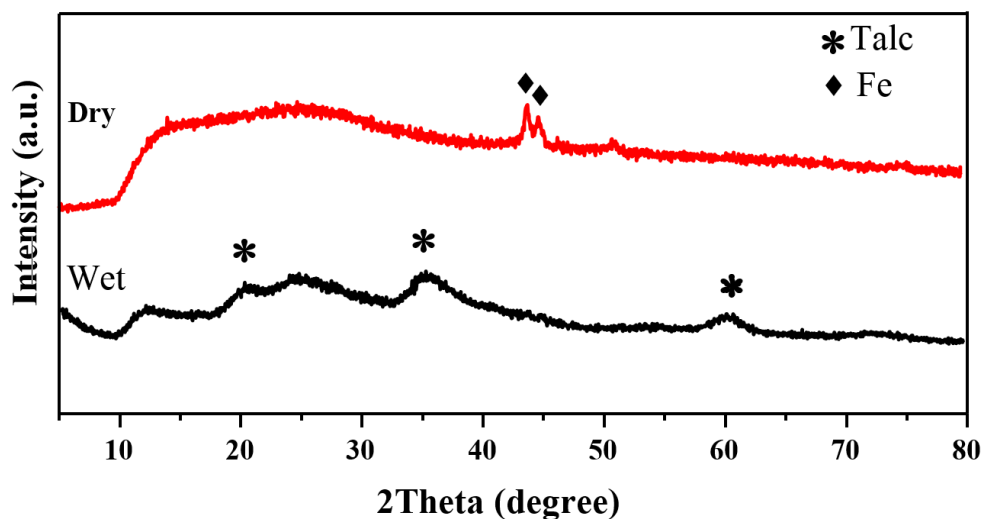


Fig. 43 XRD patterns of the 10h milled mixtures with (wet) and without water (dry).

Fig. 44 displays the XRD profiles of mixtures milled for different times, with the weight rate of water kept at 0.286. Peaks of amorphous silica evidenced by the broad XRD baseline hump at about $25^\circ 2\theta$, and brucite are detected in the patterns of the mixtures milled over 0.5h. The peak intensity of brucite was found to decline with increasing grinding time from 0.5 to 1h. This suggests that the amount of brucite decreases as grinding is progressing. With increasing milling time to 10h, the XRD patterns of brucite disappeared, and a poorly crystalline talc appeared confirming the formation of talc by a mechanochemical reaction. Thus, controlling of milling time at about 10h is a very important key to synthesize talc mechanochemically.

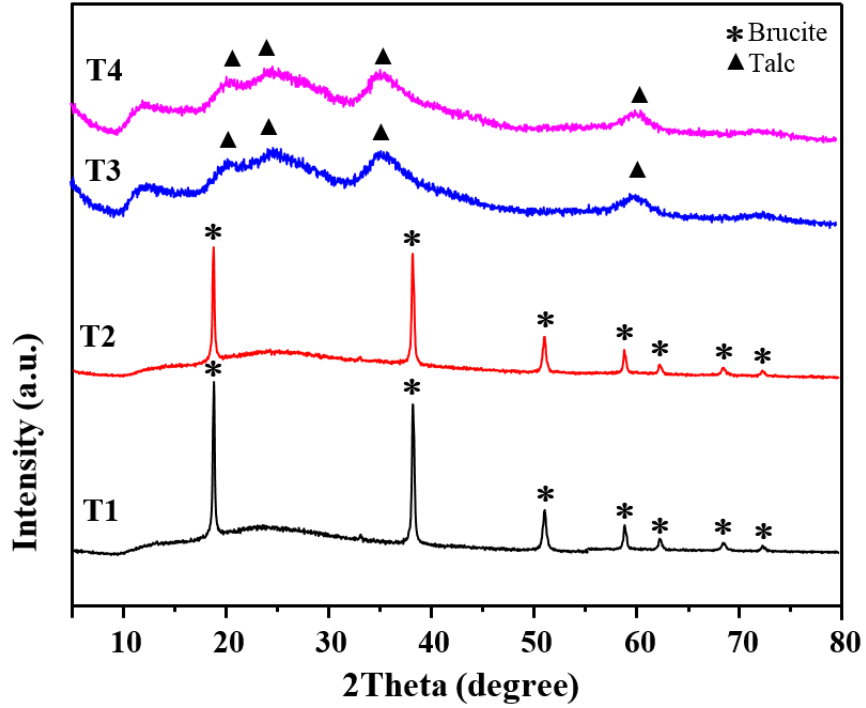


Fig. 44 XRD patterns of the mixtures as a function of milling time: T1 (0.5h), T2 (1h), T3 (5h), and T4 (10h).

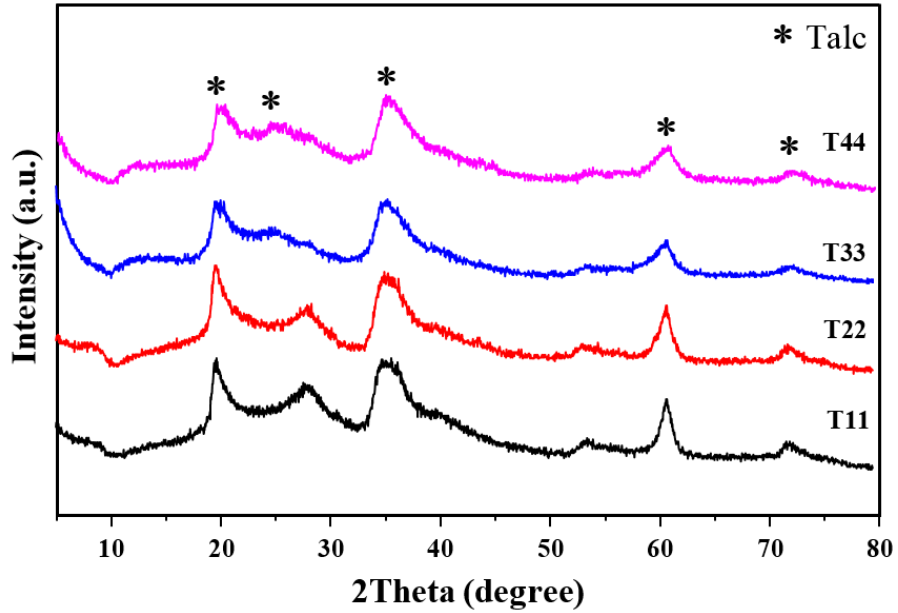


Fig. 45 XRD patterns of the different milled powders followed by autoclave treatment mixtures at 260°C for 12h: T11 (0.5h), T22 (1h), T33 (5h), and T44 (10h).

Fig. 45 presents the XRD patterns of different milled samples followed by autoclave treatment for 12h at 260°C. As evident from this figure, hydrothermal condition led to growth in crystallinity, and finally talc with appropriate crystallinity was obtained for all different milled samples. Note that the intensity and sharpness of peaks increased as compared with the peak intensity of ground powders before autoclave treatment. Moreover, the peak intensity of autoclaved specimens dropped slightly from T11 to T44, which could be associated to the reduction in particle sizes. The samples synthesized under MC and autoclave conditions exhibit the $02l-11l$ at 19.67° (2θ), 003 at 28.3° (2θ), and $06l-33l$ at 60.5° (2θ) reflections characteristic of a talc structure [71]. However, $00l$ reflections of talc were almost nonexistent, which was also reported for the synthetic talc prepared hydrothermally [72]. Finally, poorly crystalline talc can be produced via one step wet mechanochemistry method, while product with greater crystallinity can be obtained by an autoclave process step following the grinding. The findings propose a method to synthesis of talc with high purity and acceptable crystallinity, which reduces the hydrothermal treatment step from months to hours, and eliminates the preparation step of a talc precursors before hydrothermal synthesis [69].

4.2.2. FTIR analysis

The FT-IR spectra of samples as a variation of milling time (T1:1h, T2:5h, and T3:10h) are displayed in Fig. 46. It can be seen that all spectra illustrate strong or very strong absorption near 3433, 1635, 1018, 620, and 467 cm^{-1} . Bands shown near 3680, 1442, 1384, and 920 cm^{-1} , however, are weak or absent in some samples. The structural hydroxyl group and the interlayer water of all samples have stretching vibrations between

3000 and 3700 cm^{-1} . The bands in the region of 900–1100 cm^{-1} were recognized as Si-O stretching motions with tetrahedral SiO_4 groups [41], and those in the 600–700 cm^{-1} region belong to OH librations, which are accompanied by weak Si-O bending vibrations [73]. Based on Fig. 46, The spectra of T2 sample shows relatively little chemical interaction between silica gel and brucite due to the presence of brucite bands at 3762, and 3695 cm^{-1} . With increasing milling time (T3, and T4), the band at 3762 was vanished and a new absorption band at around 3675 cm^{-1} was appeared which is 20 cm^{-1} lower than the corresponding band of brucite [74], indicating the formation of talc via wet MC method. A broad peak at 3433 cm^{-1} can be attributed to the stretching modes of adsorbed water in talc [74]. Moreover, a weak water band at 1635 cm^{-1} can be resulted from deformation vibration of water molecule [52]. The bands range at 2200-2400 cm^{-1} , and 2800-3000 cm^{-1} are from KBr [75]. The symmetric stretching modes of CO_3^{2-} were also observed at around 1422 cm^{-1} (ν_3), and 1384 cm^{-1} (ν_2) confirming the absorption of CO_2 from the atmosphere during milling process [64]. The band near 1116 cm^{-1} in T2 sample is due to the stretching vibrations of the silicon-apical oxygen units in silica gel, which are perpendicular to the layer sheets [76]. The weak absorption band at 903 cm^{-1} in the T3 and T4 samples may also be attributed to the interlayer Si-OH group of layered magnesium silicate hydrate. There is a shifting band from 620 cm^{-1} in T2 to 640 cm^{-1} in T3, and T4, demonstrating the talc structure [74]. Thus, the FTIR spectra of specimens milled for longer times (T3 and T4) confirm the formation of talc as supported previously by XRD results.

Fig. 47 presents the FTIR spectra of different milled samples followed by autoclave treatment for 12h at 260° (T11, T22, T33, and T44). The spectra of all

specimens were similar to each other, resembling the spectrum of talc [77]. By applying autoclave treatment on the milled samples, the adsorption bands owing to four coordinated silica changed to the band of layer structure talc, e.g., the band at 620 cm^{-1} shifted towards 670 cm^{-1} , indicating the talc structure [74]. Since the Si-O vibration might be greatly affected by particle size, the adsorption band at 1105 cm^{-1} was vanished for T44 sample as a longer milling time (10h) has been applied. However, the O-H stretching vibrations should not be significantly impacted by particle size due to a weak coupling between adjacent hydroxyl groups [74]. The absence of bands at around 1422 cm^{-1} (ν_3), and 1384 cm^{-1} (ν_2) demonstrates a layer structure of talc without trace of any carbonate ions.

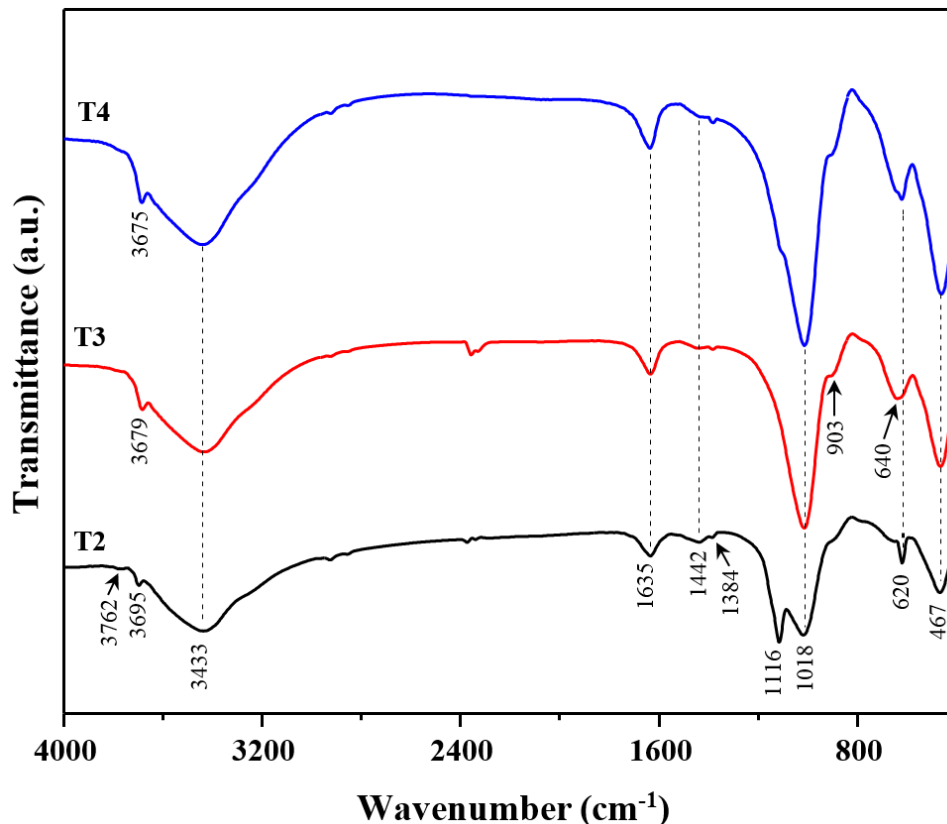


Fig. 46 The FT-IR spectra of samples as a variation of milling time (T1:1h, T2:5h, and T3:10h).

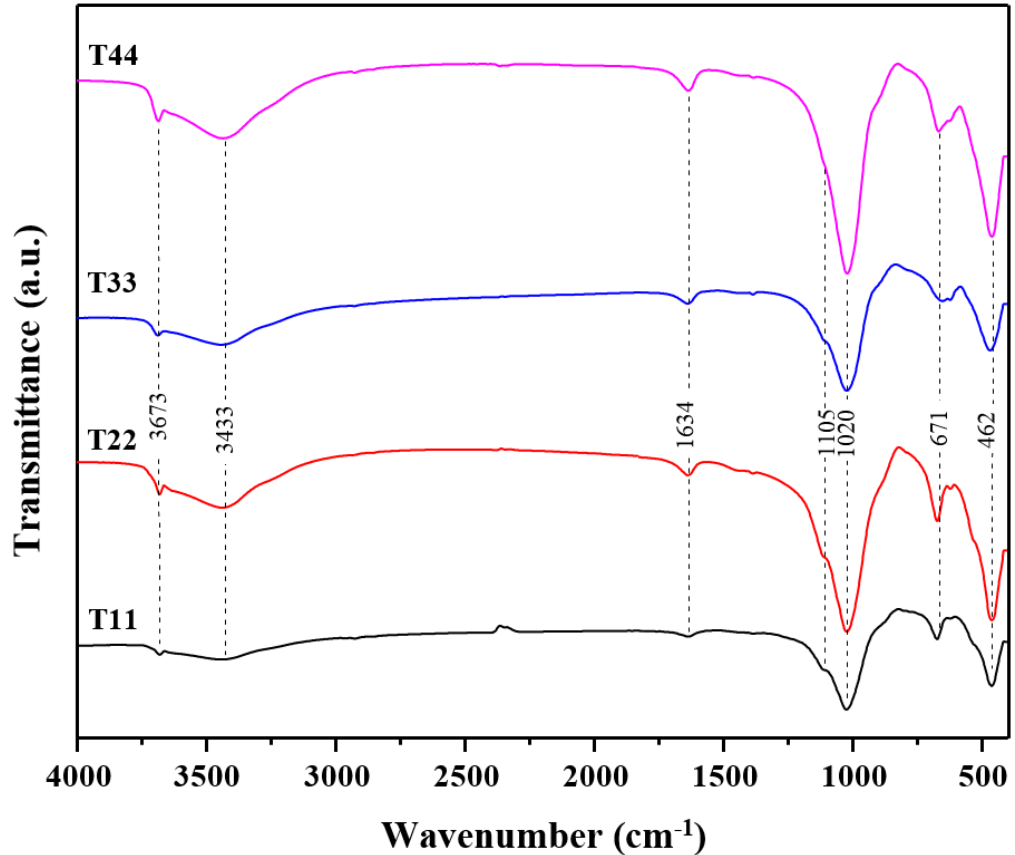


Fig. 47 FTIR spectra of the different milled powders followed by autoclave treatment mixtures at 260°C for 12h: T11 (0.5h), T22 (1h), T33 (5h), and T44 (10h).

4.2.3. Morphological characterization

Fig. 48 displays the FESEM images of sample milled for 5h. As can be seen, the agglomerates containing very fine particles formed after 5 h of milling. The SEM micrograph indicated that the mean size of agglomerates was in the range of 0.5–2 μm , however, the distribution range of the agglomerates was not identical. The occurrence of agglomerations may be associated to the coalescence of fine agglomerates/particles under mechanical activation [78]. From the close-up section, a pseudo-hexagonal platelet structure with the lateral dimension of around 300-500 nm long and 300 nm width can be

observed. This confirms the formation of clay structure through wet MC means. It is worthy to note that natural talc forms aggregate of layers [79].

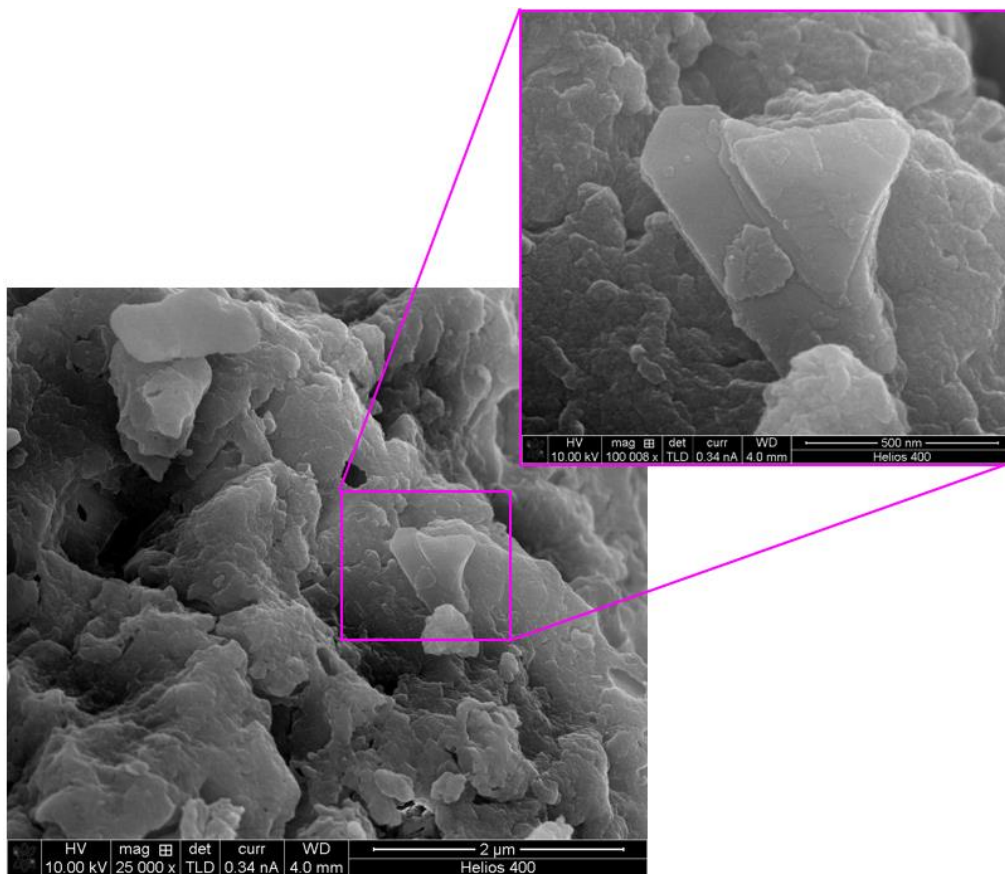


Fig. 48 FESEM image of sample milled for 5h.

The FESEM images of talc produced after 5h milling and subsequent autoclave treatment at 260°C for 12h (T33) are depicted in Fig. 49. The morphology of synthetic talc particles was very distinct as evident from Fig. 49. The shape seemed to be flaky and wavy. The length of one particle ranged between 500 and 700 nm, and the thickness was around 15 nm. It should be mentioned that the natural talc had a flaky and straight shape [79]. The particle sizes of the autoclaved sample were much larger than those of the talc particles produced mechanochemically. Thus, the morphology and sizes of the ground

particles containing talc particles are considerably different from those of the autoclaved sample.

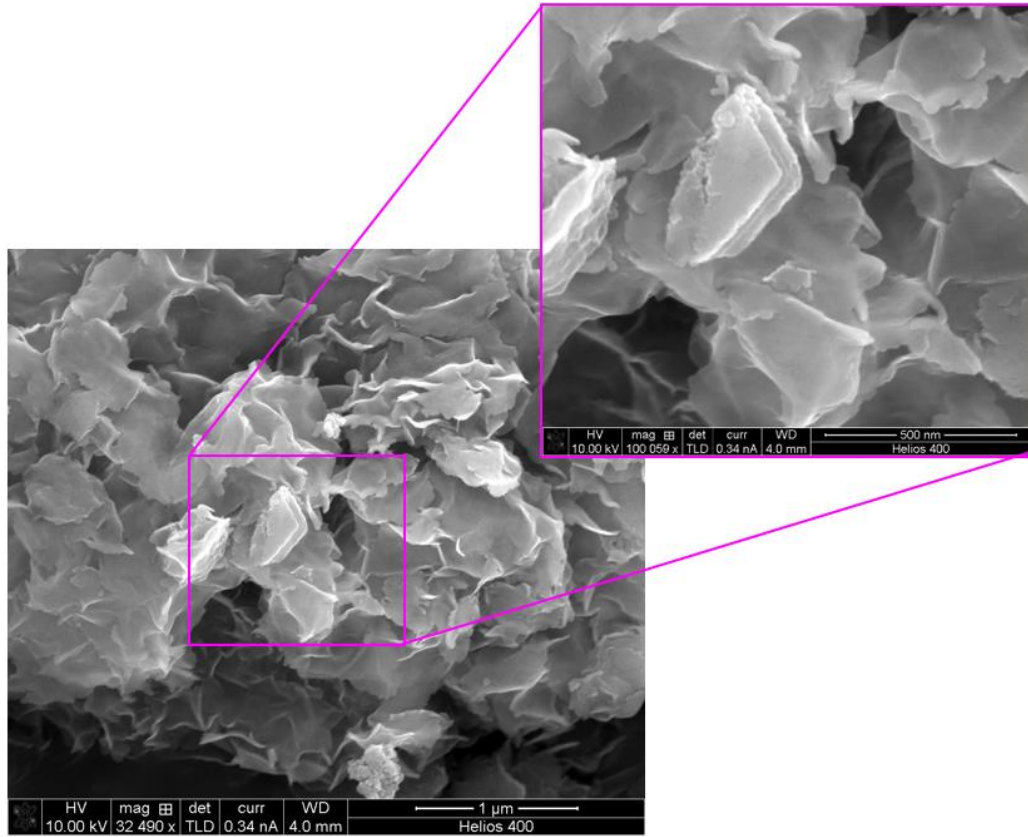


Fig. 49 FESEM images of talc produced after 5h milling and subsequent autoclave treatment at 260°C for 12h (T33).

Fig. 50 shows the TEM image of talc prepared after 5h milling and following autoclave treatment at 260°C for 12h (T33). It can be seen that a flaky structure and the polygonal (pseudo-hexagonal) platelet structure co-exist. The lateral length of polygonal particles did not exceed 1 µm and the thickness was around 15 nm. The TEM micrograph supports the morphology shown in FESEM. The morphology obtained by this method is similar to the other procedures that prepared talc through co-precipitation after one year [80], and hydrothermal methods [81].

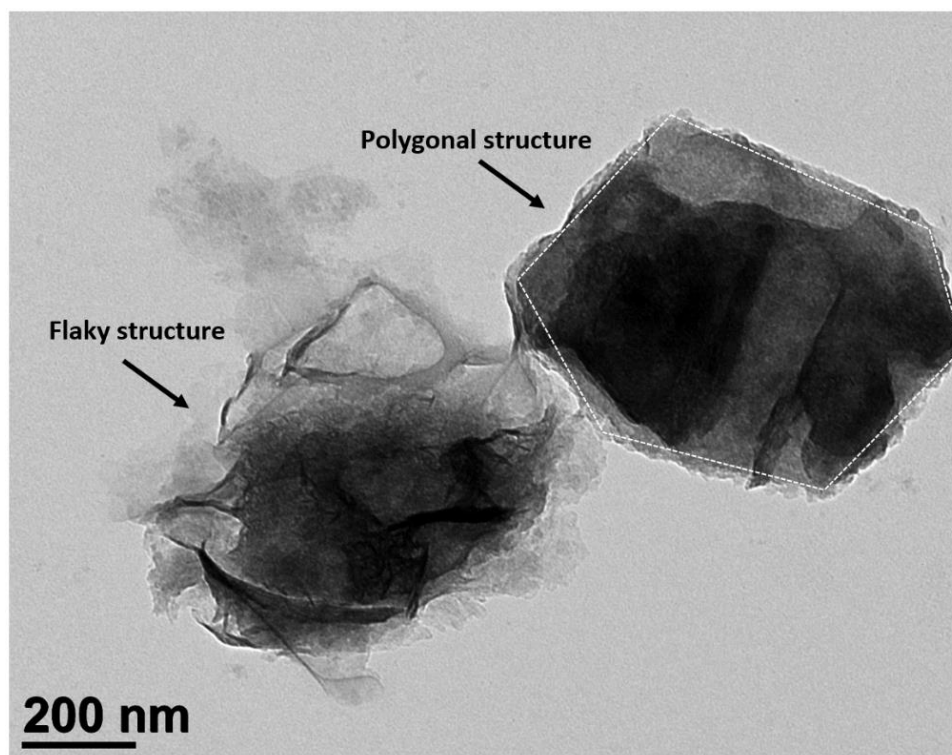


Fig. 50 TEM micrograph of talc prepared after 5h milling and following autoclave treatment at 260°C for 12h (T33).

Fig. 51 exhibit EDS spectrum of talc produced after 5h milling and following autoclave treatment at 260°C for 12h (T33). From the obtained data, the main components of the sample were oxygen, magnesium, silicon, and carbon. The EDS result demonstrates the purity of final composition of talc with no other chemically stable impurities. The total amount of magnesium and silicon present in talc was comparable with the accepted values. Based on the average value of three points from EDS data, the mole ratio of magnesium to silicon was obtained 0.79, which was very close to actual mole ratio (0.75), indicating the formation of a homogenous microstructure after 5h milling and 12h autoclave treatment.

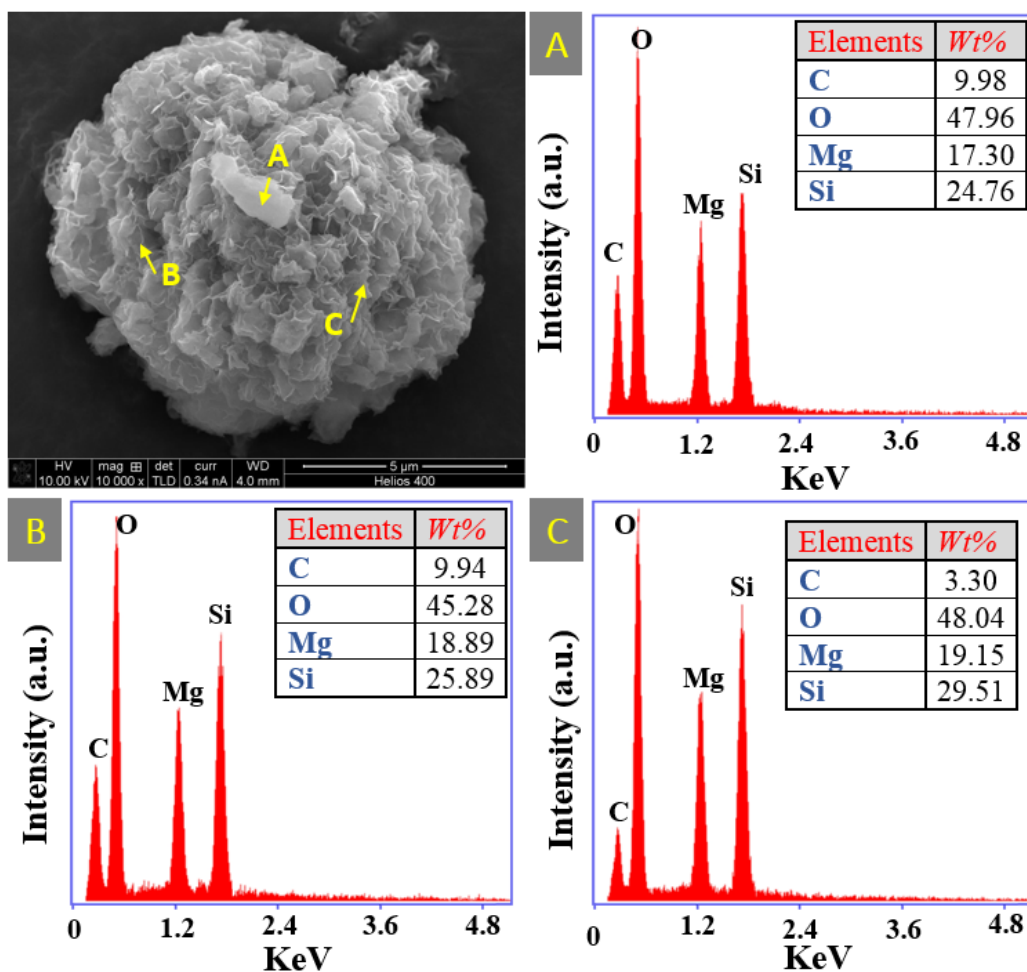


Fig. 51 EDS spectrum of talc produced after 5h milling and following autoclave treatment at 260°C for 12h (T33).

4.2.4. Thermogravimetric analysis

Fig. 52 shows the differential thermogravimetric analysis (DTGA) of 5h milled sample followed by autoclave treatment mixtures at 260°C for 12h (T33). From room temperature to 800 °C, inflections cover thermal continuous degradation with three different mass losses; 25–100, 150–250, and 450–650 °C. The TGA analysis of T33 exhibits a total mass loss similar to natural talc; however, its main loss occurs at 59.4 °C much before natural talc temperature 485 °C, which associates to the decomposition of

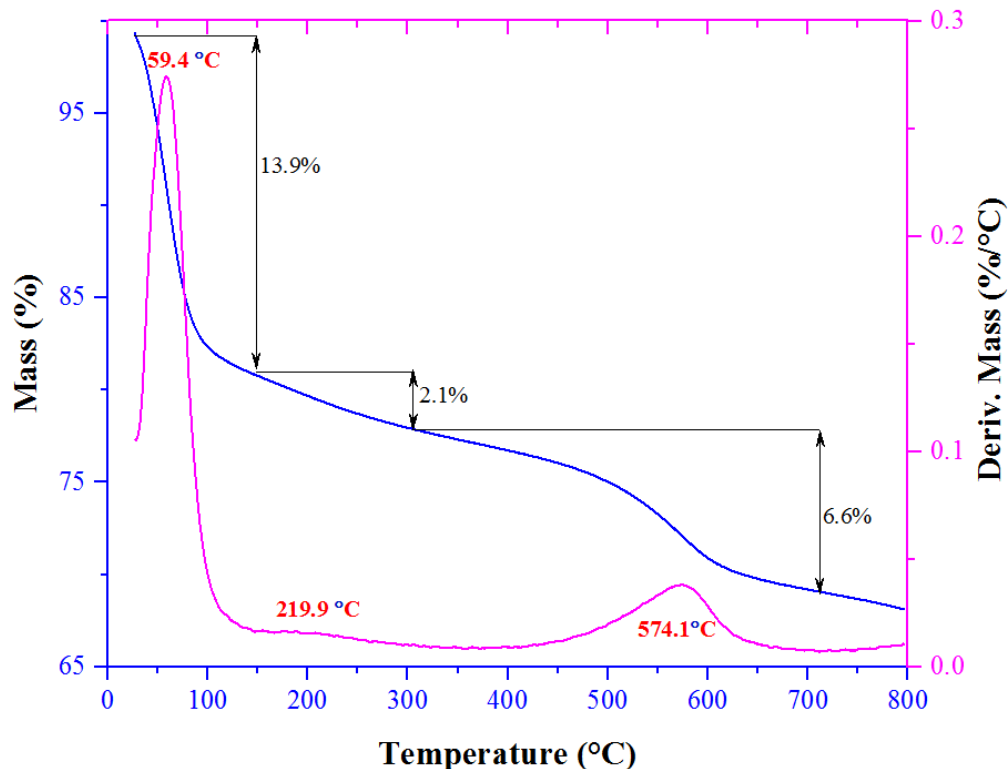


Fig. 52 DTGA graph of 5h milled sample followed by autoclave treatment at 260°C for 12h (T33).

calcite and chlorite impurities exist in the talc layers. It should be note that the full degradation of natural talc appears above 850 °C [79]. Based on Fig. 52, the first mass loss of 13.9% (25–100 °C) was contributed to the elimination of physisorbed water. The synthetic talc from our method (MC and subsequent autoclave treatment) show a great water loss due to hydrophilic behavior of synthetic talc related to more hydroxyl groups on the layer edges, consequently trapping water molecules. Nevertheless, the natural talc layers are longer and overlap at the edges indicating hydrophobic nature [81]. The second and smallest decomposition mass loss of 2.1% from 150°C to approximately 250°C was attributed to the interlayered water loss, which may be based on the loss of magnesium hydroxides (Mg–OH) on the sheet edges and silanols (Si–OH) [81]. The final

decomposition from 450 °C to 650 °C with a mass loss of 6.6% attributed to the dehydroxylation of talc lamellae, which is a lower thermal stability of our new synthetic talc compared to the natural talc (950 °C). The total mass loss at 800 °C was about 22.6%. The thermal stability difference can be explained by thinner particles in the case of synthetic talc prepared in this research [82]. The TGA result of talc using our new method is comparable with the hydrothermally treated ones [81, 83].

4.3. Conclusions

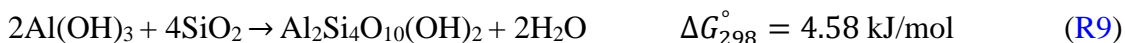
This research part presents that poorly crystalline talc can be produced successfully via one step wet mechanochemistry method, while talc with greater crystallinity can be obtained by the following autoclave process. Based on phase analysis, the FTIR spectra of specimens milled for longer times e.g. 5h (T3) and 10h (T4) confirm the formation of talc as supported previously by XRD results. Moreover, the FTIR spectra of different milled samples followed by autoclave treatment demonstrates a layer structure of talc without trace of any carbonate ions. From microscopic observations, talc produced mechanochemically shows agglomeration including a pseudo-hexagonal platelet structure with the lateral dimension of around 300-500 nm long and 300 nm width. While, talc formed through autoclaving assisted mechanochemistry displays a delaminated and flaky structure containing the polygonal (pseudo-hexagonal) platelet structure with larger particle sizes indicating crystal growth. DTGA analysis shows the thermal continuous degradation with three different mass losses exhibiting a total mass loss similar to natural talc.

5. PYROPHYLLITE – HALOYSITE

In this chapter, the preparation of Pyrophyllite (PP) and Halloysite (HS) using wet mechanochemistry and subsequent autoclave processes was investigated. To achieve this goal, two distinct reactions were designed. The structural features and morphological characteristics of samples have been studied for different conditions. Products were then characterized by XRD, FTIR, FESEM, EDS, TEM, and DTGA. Detailed study of the phase behavior and structural trends was also studied. Moreover, the thermal decomposition details of both final products were examined and reported.

5.1. Experimental procedure

Aluminum hydroxide (99 %, ACROS), and silica gel (99 %, Sigma-Aldrich), were purchased and used as received. To prepare Pyrophyllite (PP) and Halloysite (HS), the desired amounts of Al(OH)₃, silica gel, and certain amount of water were milled for 5h in a high energy ball mill using hardened chromium steel vials under air atmosphere. The excess water was used to take advantage of hydrothermal process in mechanical activator, so the water to mixture (water and powders) ratio was considered around 0.286. The weight ratio of ball-to-powder (BPR) for all specimens was 10:1. The final composition for PP and HS was adjusted based on the following reactions (R9), and (R10), respectively:



The 0.5 g of milled powders of each reaction was then poured in 15 ml deionized water and stirred in 50 ml beaker for about 10 min under constant vigorous stirring using

a magnetic stirrer. Then, the slurry was placed in autoclave chamber (25 ml volume) and was put in an oven at 260°C for 24h. Finally, the slurry was poured on a paper filter, and then were dried under oven at 60°C for 1h. So the product produced after 5h milling and autoclaving for Pyrophyllite and Halloysite were labeled as K1, K2, K3 and K4, respectively.

5.2. Result and Discussion

5.2.1. XRD analysis

Fig. 53 shows the XRD profiles of milled and autoclaved samples for Pyrophyllite (K1, K3) and Halloysite (K2, K4), respectively. With the aid of the JCPDS X-ray powder data files, the phase identification disclosed the broad XRD baseline hump of silica and several sharp peaks of brucite for milled samples (K1, and K2). However, the intensity of brucite peaks for PP sample was greater than HS as expected according to equation (R9). By applying autoclave treatment on the milled samples (K3, K4), the formation of kaolinite as the main product of reactions (R9) and (R10) was obtained, however the trace of PP and HS peaks can be also observed, which were overlapped by some KAO peaks. This indicates that the synthesis of PP and HS via one step MC method cannot be achieved solely, and subsequent autoclave treatment led to the KAO formation with appropriate crystallinity. The XRD results were in good agreement with former studies, where KAO were precipitated hydrothermally at different temperature for a time periods varying from 6 h to 60 days [84]. The basal spacing of K3 and K4 were obtained as follow: 7.15Å at 12.37°, and 7.14Å at 12.39°, respectively. The obtained basal spacing confirms the presence of KAO as a major phase, which is close to standard value (7Å)

[85], However, Wilson et al. [86] reported $\sim 7.2\text{\AA}$ as a basal spacing value for Metahalloysite. It should be noted that the chemical formula of KAO and HS are the same, and the XRD patterns of both are similar in most angles, hence final identification of those phases needs to be determined through other characterization techniques such as electron microscopy. The employment of MC and hydrothermal methods to synthesis of aluminosilicate may also be of great interest in industrial applications, which decreases the preparation time of synthetic clays through hydrothermal treatment means [87, 88].

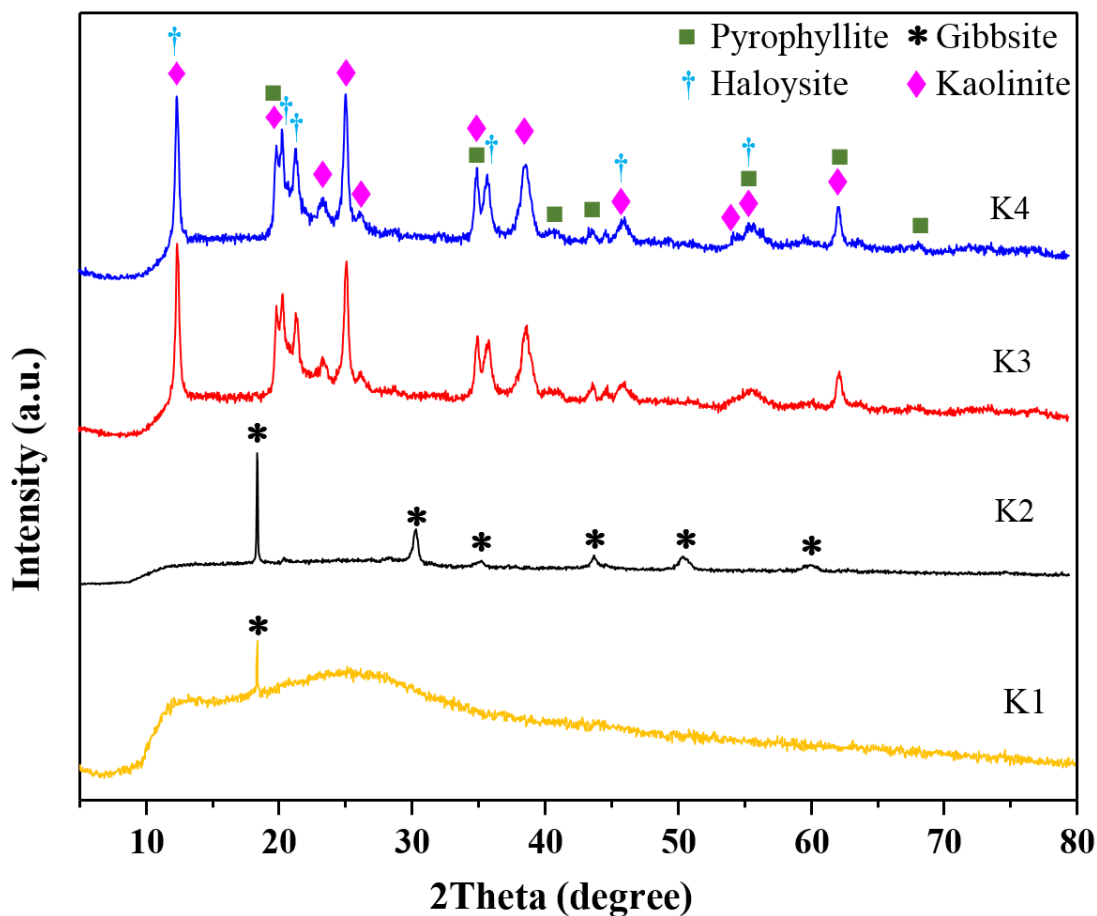


Fig. 53 XRD patterns: Pyrophyllite; MC (K1), autoclave assisted MC (K3), Halloysite; MC (K2), autoclave assisted MC (K4).

5.2.2. FTIR analysis

Fig. 54 displays the FTIR spectra of different milled samples followed by autoclave treatment for 24h at 260° (K3, and K4). The spectra of both specimens were similar to each other, resembling the spectrum of layer structure aluminum silicate [89]. The spectra in the 3400-3750 cm^{-1} region were recognized as the hydroxyl stretching region for the series of kaolinite and halloysite minerals. The band at 3626 cm^{-1} has been

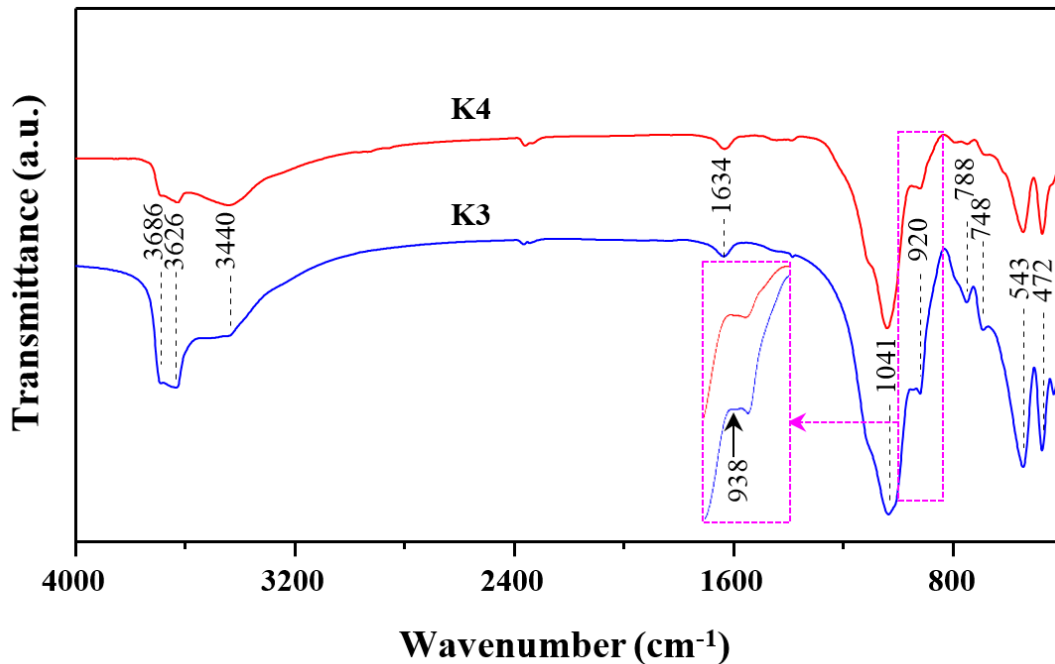


Fig. 54 FTIR spectra of PP (K3) and HS (K4) samples milled for 5h followed by autoclave treatment for 24h at 260 °C.

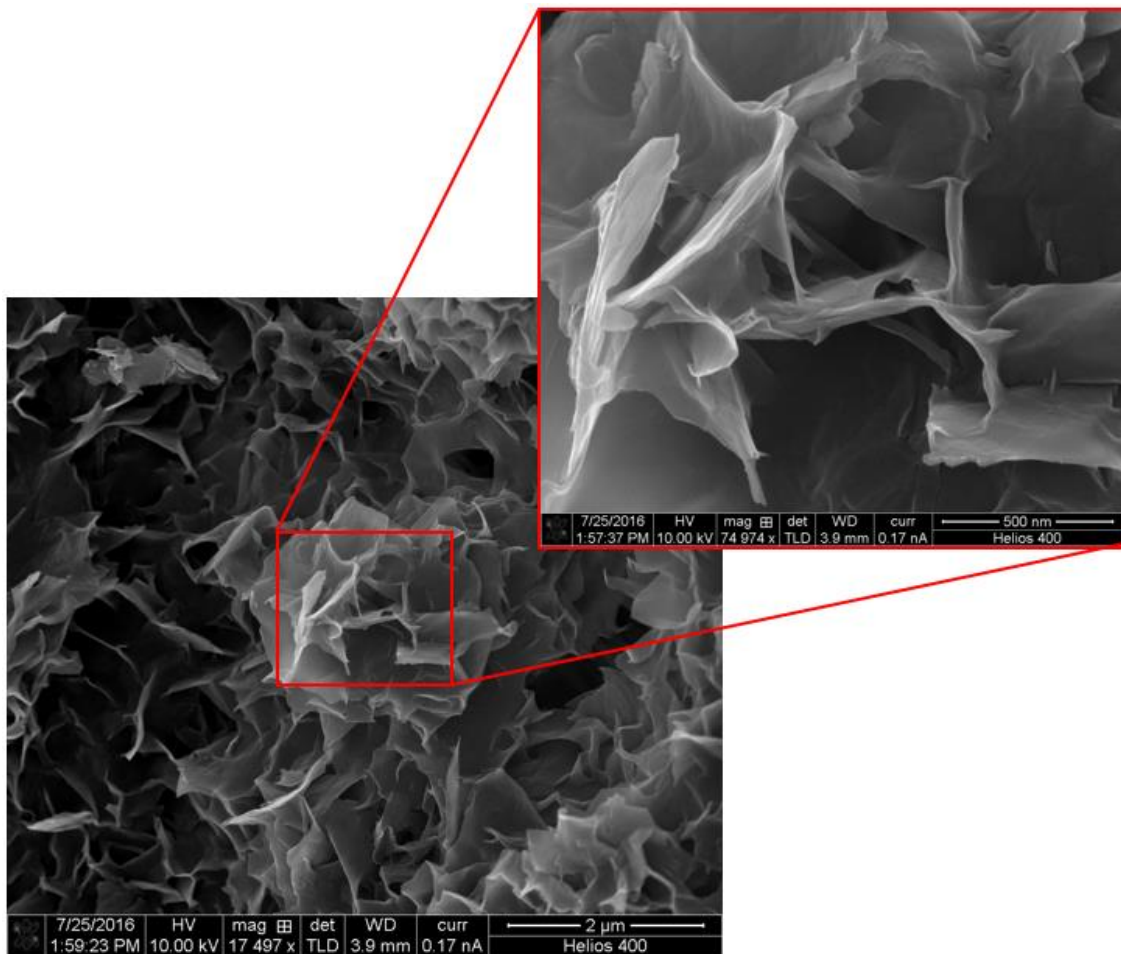
assigned to the coupled inner surface hydroxyl, while the presence of band at 3686 cm^{-1} has been attributed to an uncoupled inner surface hydroxyl [90]. The two bands at around 3626, and 3686 cm^{-1} were assigned for Halloysite. The OH stretching vibrations of water can be also observed at the band at 3440 cm^{-1} . This band was also credited as a bond between a basal hydroxyl of one sheet and the "puckered" oxygen of the next sheet [91].

Moreover, a weak water band at 1634 cm^{-1} can be resulted from deformation vibration of water molecule [52]. The absorption bands centered at 1101 cm^{-1} , and 1041 cm^{-1} are assigned to Si-O stretching vibrations [92]. Additionally, the band at 920 cm^{-1} is also corresponding to Al-OH bending vibrations of HS for both sample, however, in KAO this band has a shoulder at 938 cm^{-1} [89], which can be observed in K3 (as evident from close-up). The band at 788 cm^{-1} was recognized as Si-O-Si inter tetrahedral bridging bonds in silica [93]. Moreover, the two bands at 543 cm^{-1} and 472 cm^{-1} correspond to Si-O bending vibrations, which are analogous for pyrophyllite [94]. Therefore, the results may suggest a KAO structure for K3, and HS structure for K4, however high-defect KAO and HS exhibit very similar IR spectra [89].

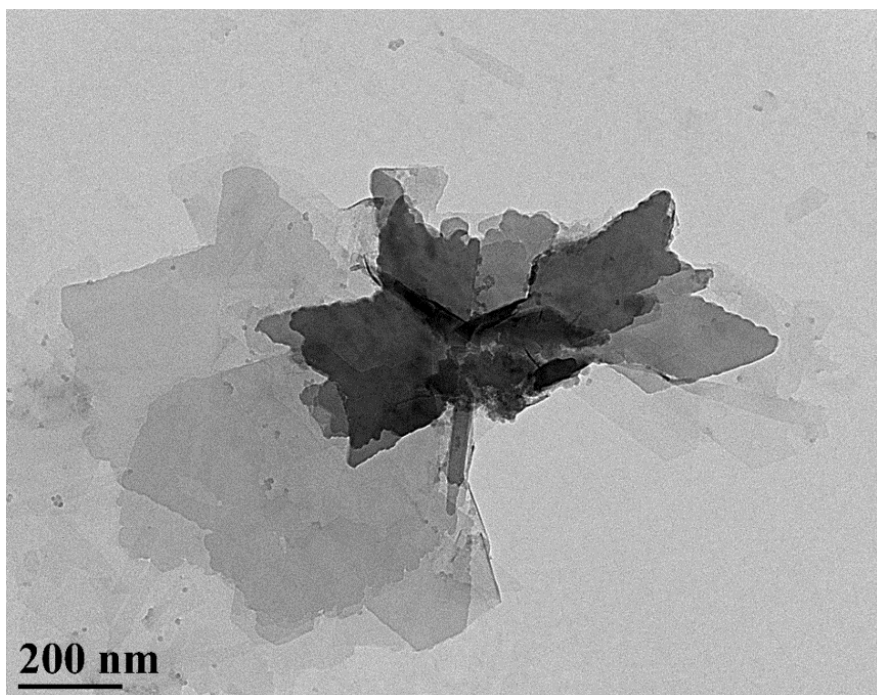
5.2.3. Morphological characterization

The FESEM images of sample (K3) milled for 5h milling and autoclave treated for 24h at 260°C are depicted in [Figs. 55](#). As evident from [Fig. 55](#), the morphology of K3 powders seemed to be flaky, which may be seen growing from the edges of the plates. The similar morphology was also reported for KAO synthesized by other methods e.g. hydrothermal process [95, 96]. Such an arrangement proposes that authigenic KAO grows at distinct temperature through the aggregation of very fine particles including positively charged edge surfaces, and negatively charged basal surfaces. The length of platy particles ranged between 500 nm and 1 μm , and the thickness was around 13 nm. [Figs. 56](#) presents the TEM image of sample K3. A well-defined delaminated flakes structure in a pseudo-hexagonal form was evidenced by TEM micrograph. The individual flaky crystal displays different lateral dimensions ranged from 200 nm to 600 nm.

Figs. 57 shows the FESEM micrographs of sample (K4) milled for 5h followed by autoclave treatment for 24h at 260°C. From a lower magnification, a flower-shaped platy structure including ribbons can be observed. From the close-up section, some partially rolled plates was entirely recognizable, while the particles showed the signs of layer folding. The partially rolled platy layers did not exceed 1 μm in length, and the thickness

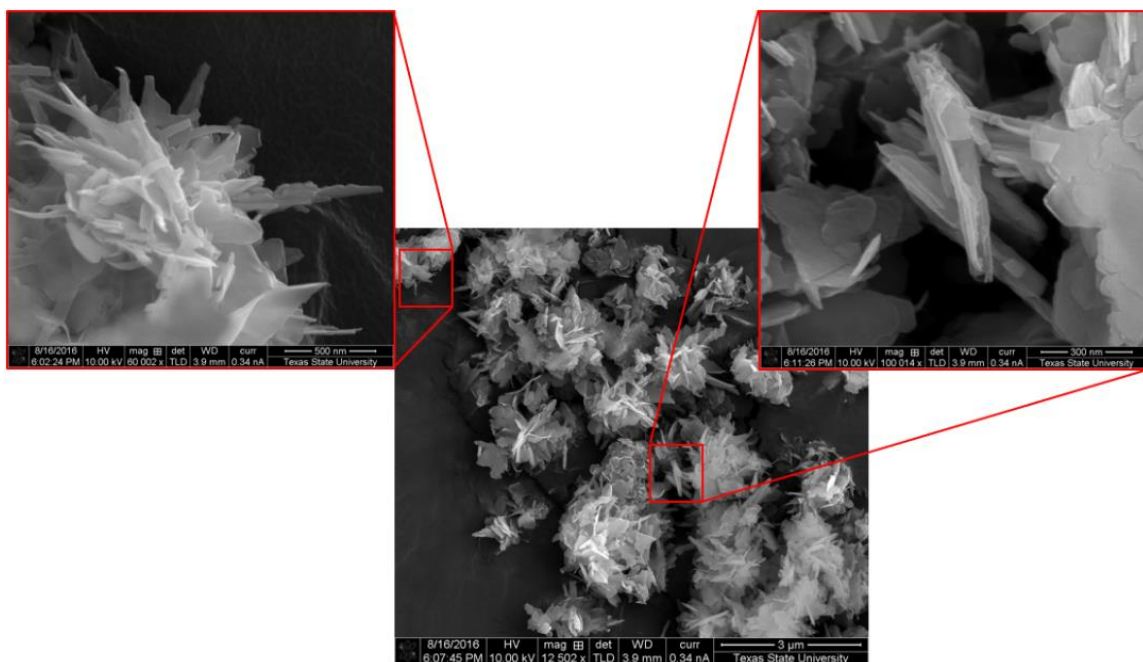


Figs. 55 FESEM images of K3 milled for 5h and autoclave treated for 24h at 260°C.



Figs. 56 TEM image of K3 milled for 5h and autoclave treated for 24h at 260°C.

was around 10 nm. The difference in FESEM morphology between K3 and K4 would be ascribed to the amount of initial reagents used in which gibbsite for K4 was consumed in double based on the reaction (R10) as compared with K3 (R9). Although, the flaky morphology of K3 in Figs. 55 was representative of KAO crystal structure, the partially rolled plates can be also attributed to the KAO [97]. It should be noted that HS has a nanotubular morphology, whereas short tubes and spheroids can also be associated to HS [89]. Therefore, the morphology obtained for K4 might not be assigned to HS. TEM image in Figs. 58 further discloses that the flower-like hierarchical assemblies had numerous nanoribbon (~ 500 nm long), and ultrathin nanosheets extending outwards from the center of microstructure.



Figs. 57 FESEM images of K4 milled for 5h and autoclave treated for 24h at 260°C.

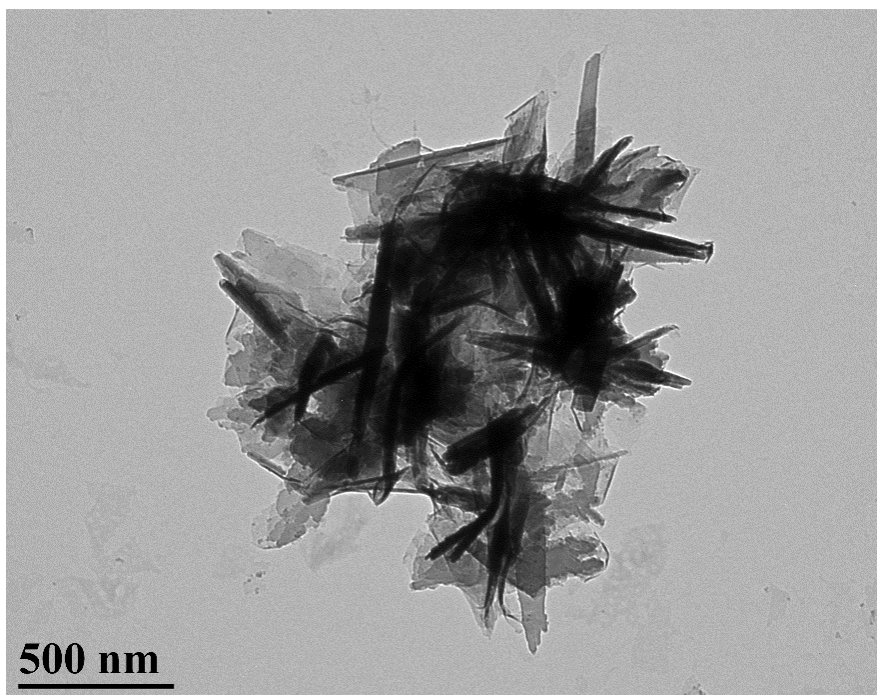


Fig. 58 TEM image of K4 milled for 5h and autoclave treated for 24h at 260°C.

5.2.4. Thermogravimetric analysis

The differential thermogravimetric analysis (DTGA) of samples milled for 5h followed by autoclave treatment for 24h at 260 °C (K3, and K4) are portrayed in Figs. 59 and 60. It can be seen that there are two mass losses during heating of both samples. The first mass loss appears between 50 to 100 °C, and 25 to 65 °C for K3 and K4, respectively. The mass losses of 4.24% (K3) and 1.96% (K4) are recognized as the elimination of adsorbed water (surface and interlayer) [98]. The second and largest mass losses of 9.62% (300-500 °C), and 11.9% (300-600 °C) occur in K3 and K4, respectively, which corresponding to structural dehydroxylation, and the removal of octahedral hydroxyl groups [94]. It has been reported [99] that the well-ordered KAO has broad

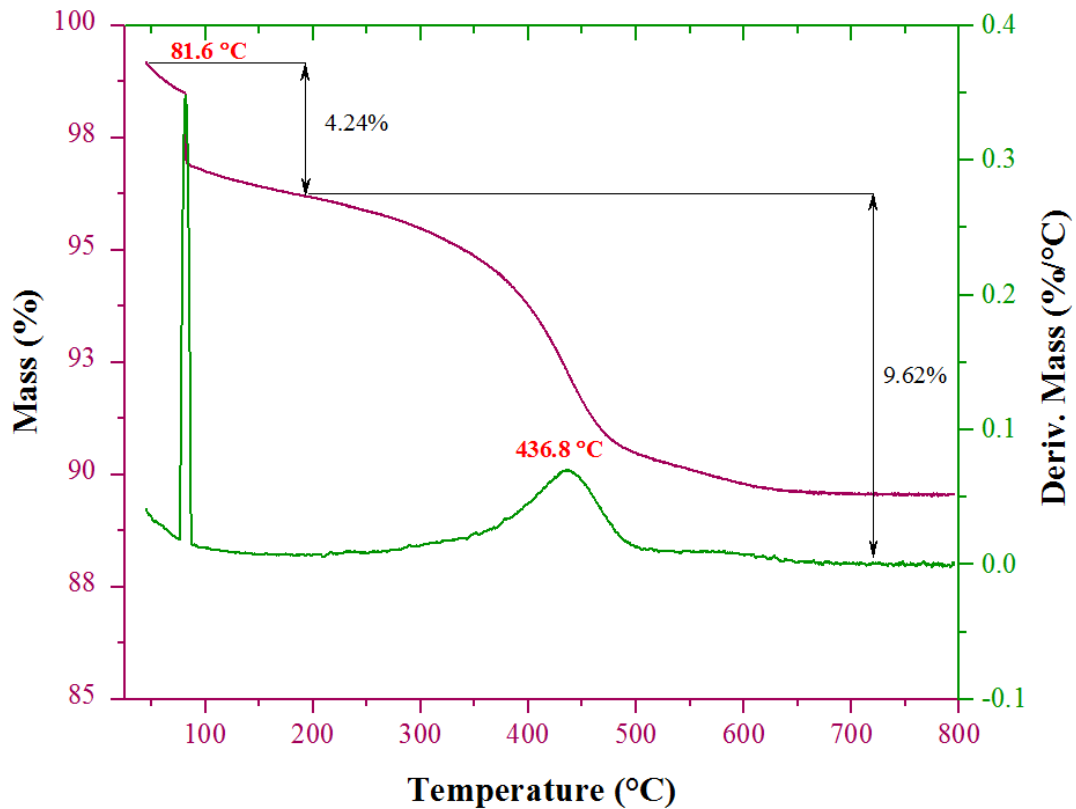


Fig. 59 DTGA of K3 milled for 5h followed by autoclave treatment for 24h at 260 °C.

endotherms, as indicated in Fig. 59. Note that the peak centered at around 436 °C in K3 was reported for KAO [100]. The endothermic peak centered at 460 °C in K4 is equivalent to the data reported for HS [89], suggesting HS formation based on our method. The total mass losses for K3 and K4 at 800 °C were about 13.86%.

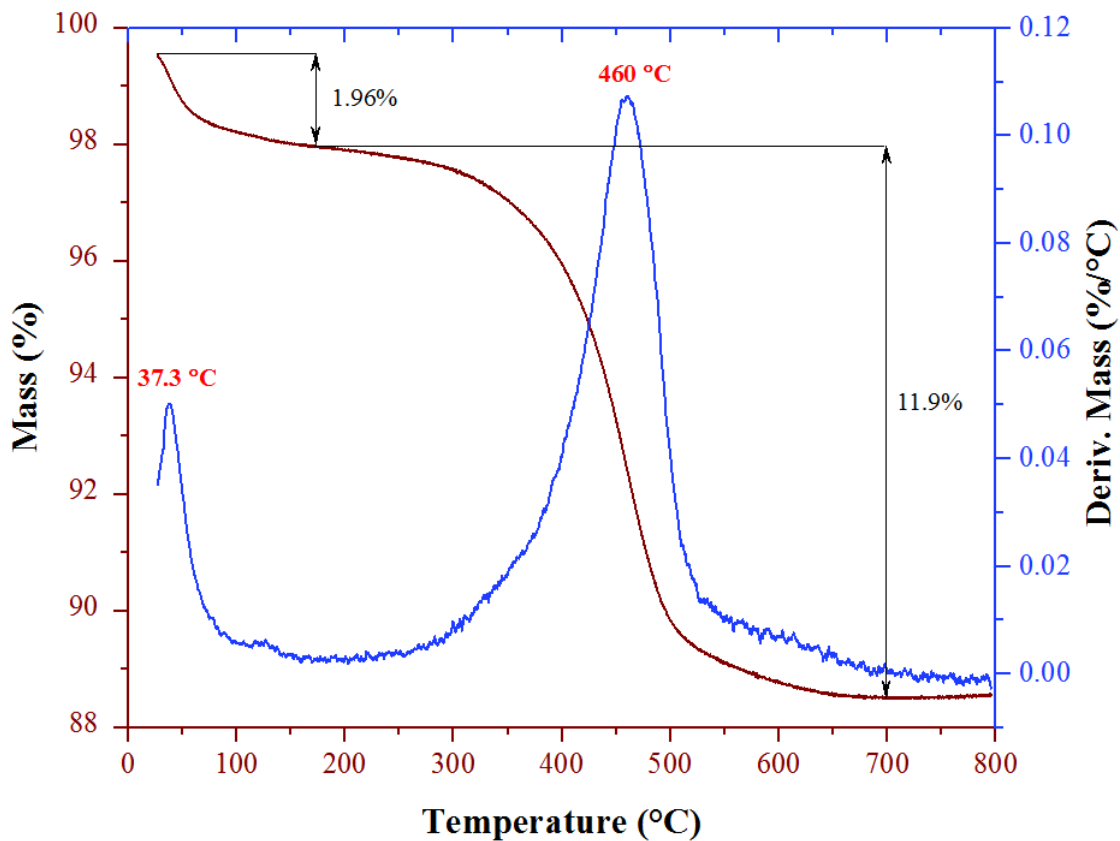


Fig. 60 DTGA of K4 milled for 5h followed by autoclave treatment for 24h at 260 °C.

5.3. Conclusions

This research aims at producing PP and HS based on two distinct reactions. According to the phase analyses, high crystalline KAO with two different morphologies was formed after milling and autoclaving processes. In simple terms, the synthesis of PP

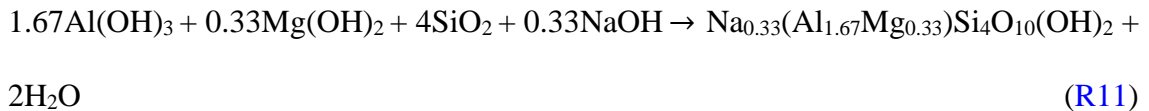
and HS via one step MC method cannot be achieved solely, and subsequent autoclave treatment instead led to the KAO formation with appropriate crystallinity. FTIR results suggest a KAO structure for K3, and HS structure for K4, respectively, however high-defect KAO and HS exhibit very similar IR spectra. The electron microscope micrographs disclose that a well-defined delaminated flakes structure in a pseudo-hexagonal form was obtained for K3 sample, while, a flower-shaped platy structure including ribbons was formed for K4 sample. The DTGA curves reveal that there are two mass losses during heating of both samples. The DTGA graph of K3 sample was assigned to KAO, while graph of K4 was equivalent to the data reported for HS.

6. MONTMORILLONITE

This chapter introduces the synthesis of Montmorillonite (MMT) using wet mechanochemistry and following autoclave process. The structural features and morphological characteristics of powders have been studied for a variety of milling times and different autoclave time. Products were characterized by XRD, FTIR, FESEM, EDS, TEM, and DTGA. Detailed study of the phase behavior and structural trends was also scrutinized. Additionally, the thermal decomposition details of MMT were studied and reported here.

6.1. Experimental procedure

Reagents used in this research part were Magnesium hydroxide (99 %, Sigma-Aldrich), Aluminum hydroxide (98 %, ACROS), Sodium Hydroxide (Sigma-Aldrich), and silica gel (99 %, Sigma-Aldrich). The mixture (2 g) of Brucite, gibbsite, silica gel, and sodium hydroxide was put into the mill pot with certain amount of water (0.8 ml) and milled at different milling times (5 and 10h) in a high energy ball mill (Vibratory mill). An optimal ratio of water to mixture (water and powders) was kept 0.286 [67]. The presence of excess amount of water would provide a hydrothermal condition along with mechanical activation. For all specimens, the weight ratio of ball-to-powder (BPR) was 10:1. The final composition for different milling time was adjusted following the reaction (R11):



A slurry containing 0.5 g of milled sample and 15 ml deionized water were stirred in 50 ml beaker for 10 min under constant vigorous stirring using a magnetic stirrer. Then, the slurry was poured in autoclave chamber (25 ml volume) and was kept in an oven at 260°C for different times (24, 48, 72, and 96h). Finally, the slurry was poured on a paper filter, and then were dried under oven at 60°C for 1h. So the sample milled for 10h, and autoclaved for various times were labeled as M1(24h), M2 (48h), M3 (72h), and M4 (96h).

6.2. Result and Discussion

6.2.1. XRD analysis

[Fig. 61](#) shows the XRD patterns of the mixtures ground for two milling times (5 and 10h). Based on wet grinding XRD profiles, it can be observed a broad amorphous hump of silica and sharp peaks of gibbsite after 5h milling treatment. Moreover, the peaks representative of sodium hydroxide and brucite were not detected owing to lower concentration. With increasing the milling time to 10h, a large amorphous hump and two small crystalline peaks corresponding to Fe contamination due to excessive wear of balls and vials were detected. The absence of gibbsite after 10h confirmed that an amorphous solid solution containing silica, gibbsite, brucite, and sodium hydroxide was formed.

In order to synthesis of MMT, an autoclave treatment was applied on the milled powders at temperature of 260 °C, at time period varying from 24h (M1), 48h (M2), 72h (M3), and 96h (M4). The diffraction patterns of autoclaved powders were illustrated in [Fig. 62](#). As evident from this figure, a single phase of MMT was obtained for all samples, as evidenced by the position of the characteristic reflection peaks at 4–8°, 12.3°, 19.8°,

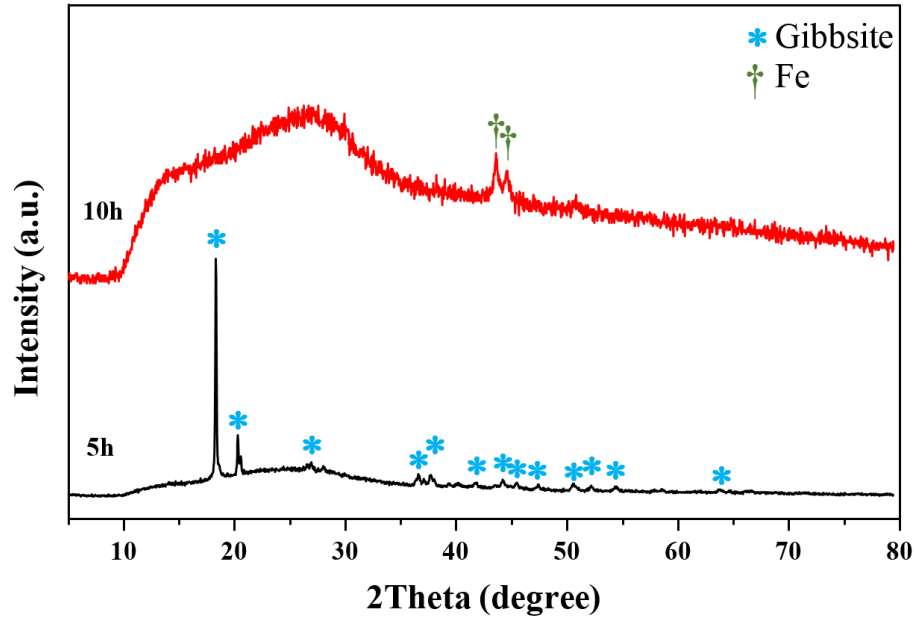


Fig. 61 XRD patterns of the mixtures grounded for two milling times (5 and 10h).

25.2°, 35.3°, 38.3°, and 60.2°. This indicates that the amorphous solid solution has been transformed into crystalline MMT phase. The reflection at angles 4–8° (d_{001}) is characterized by basal space between the silicon-oxygen layers in the MMT sample [42]. At lower temperature (M1), a crystalline MMT phase with a broad reflection peak at angles 4–8° was obtained. The broadening of the reflection peak (001) can be associated with a reduction in the size of coherent scattering regions, which is perpendicular to the layer plane [101], with a loss of periodicity along axis c [102, 103], low dimension of particles, irregularity of packing of packages (lamellae), insufficient degree of crystallinity [42], and insufficient time of autoclaving. A MMT phase with higher crystallinity was obtained at longer autoclaving time period particularly for M3 sample, clearly indicating a reflection d_{001} with higher intensity. With increasing of autoclaving duration for 96h (M4), a lower crystalline MMT phase was obtained. A close-up section of diffractions at angles 4–8° (d_{001}) is visible in Fig. 62. The basal spacings were obtained

as follow; 13 Å at 6.82° (M1), 14.58 Å at 6.06° (M2), 15.96 Å at 5.54 (M3), and 15.11 Å at 5.84° (M4). This demonstrates a small shifting peaks toward higher d space particularly for M3 sample. This changes can be related to the enhancing degree of substitution of magnesium atoms for aluminum. This shows that the duration of autoclaving for 72h works best to prepare a high crystalline MMT. The XRD profile of MMT obtained via this process is comparable with product of hydrothermal method [42].

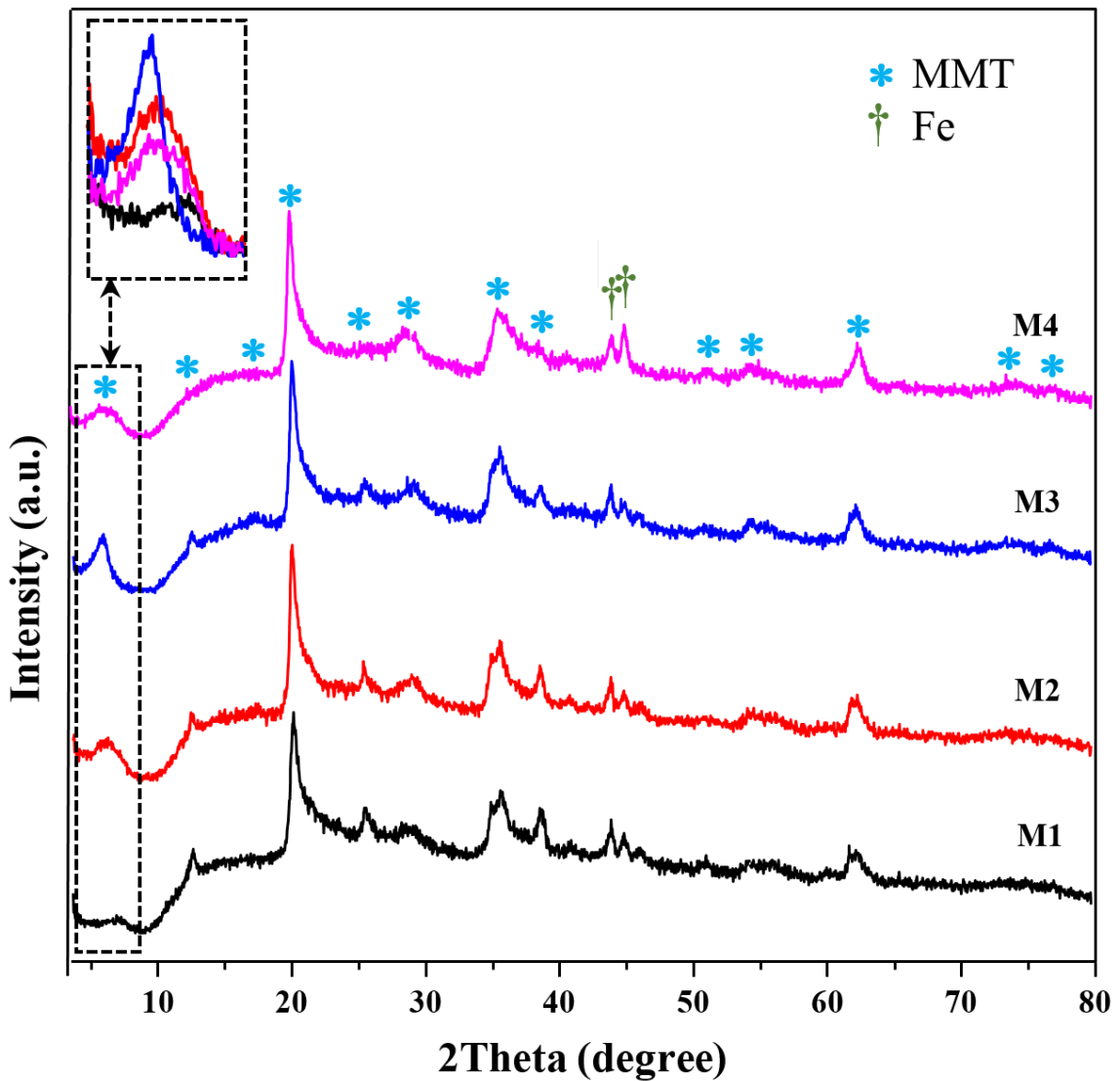


Fig. 62 XRD patterns of autoclaved powders as a variation of time: 24h (M1), 48h (M2), 72h (M3), and 96h (M4).

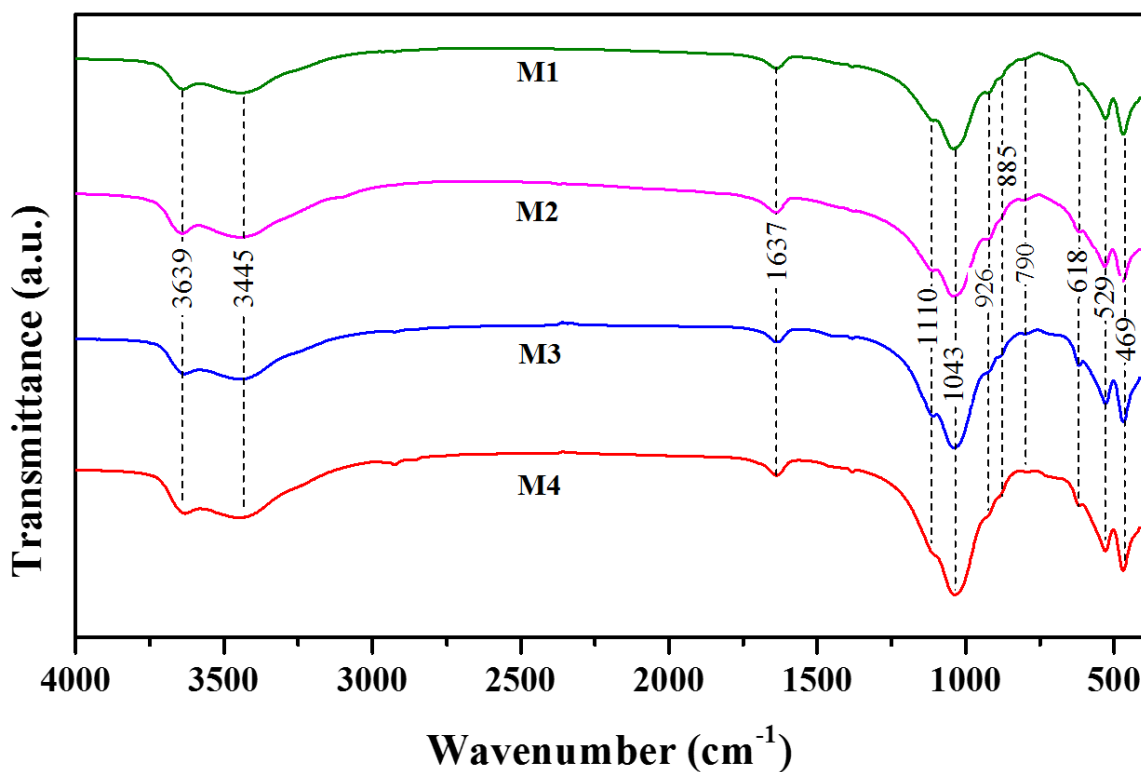


Fig. 63 FTIR spectra of MMT milled for 10h followed by autoclave treatment at 260° for different times: 24h (M1), 48h (M2), 72h (M3), and 96h (M4).

6.2.2. FTIR analysis

FTIR spectra of milled powders for 10h followed by autoclave treatment at 260° for different times varied from 24h to 96h (M1, M2, M3, and M4) are shown in Fig. 63. The bands at around 3639 cm^{-1} and 3445 cm^{-1} are associated with the stretching modes of Si–OH and OH groups of interlayer water, respectively [104], and the bending vibrations of adsorbed water in the interlayer can be also seen at 1637 cm^{-1} [105]. The band at 1043 cm^{-1} and its shoulder peak at 1110 cm^{-1} are ascribed to Si–O and Si–O–Si, respectively. Note that the strong peak at around 1043, 926, 885, and 790 cm^{-1} (Al–O bending) are characteristic vibrations of MMT clay [106, 107], which are evident in all samples. In the region of the spectrum under 1000 cm^{-1} , the peaks are ascribed to some

small lattice absorption bands, which can be attributed to the Si–O–Al and Mg–O stretching modes at 529 cm^{-1} , and 469 cm^{-1} , respectively. The Mg–O and Al–O stretching vibrations are associated to structural tetrahedral and octahedral absorption bands in MMT, respectively [105]. As can be seen, a new band was also appeared at 618 cm^{-1} , which could be due to the formation of isolated broken octahedral layer filled with divalent Mg cations indicating their trioctahedral character [108]. From the FTIR spectra, all the bands corresponding to MMT are evident in all autoclave times, demonstrating the formation of MMT with no trace of carbonate ions and appropriate purity.

6.2.3. Morphological characterization

The FESEM images of MMT (M3) produced after 10h milling and subsequent autoclave treatment at 260°C for 72h are depicted in [Fig. 64](#). The morphology of synthetic MMT particles appears in the form of microlayers twisted in a rose-shaped platy structure. It should be mentioned that the average pore diameters were around $1\text{ }\mu\text{m}$. The size distribution of particles was homogenous. The pore and particle size obtained through our method are much bigger than ones obtained via hydrothermal means [42]. This characteristic provides a great potential to synthesis of new nanocomposites for many applications.

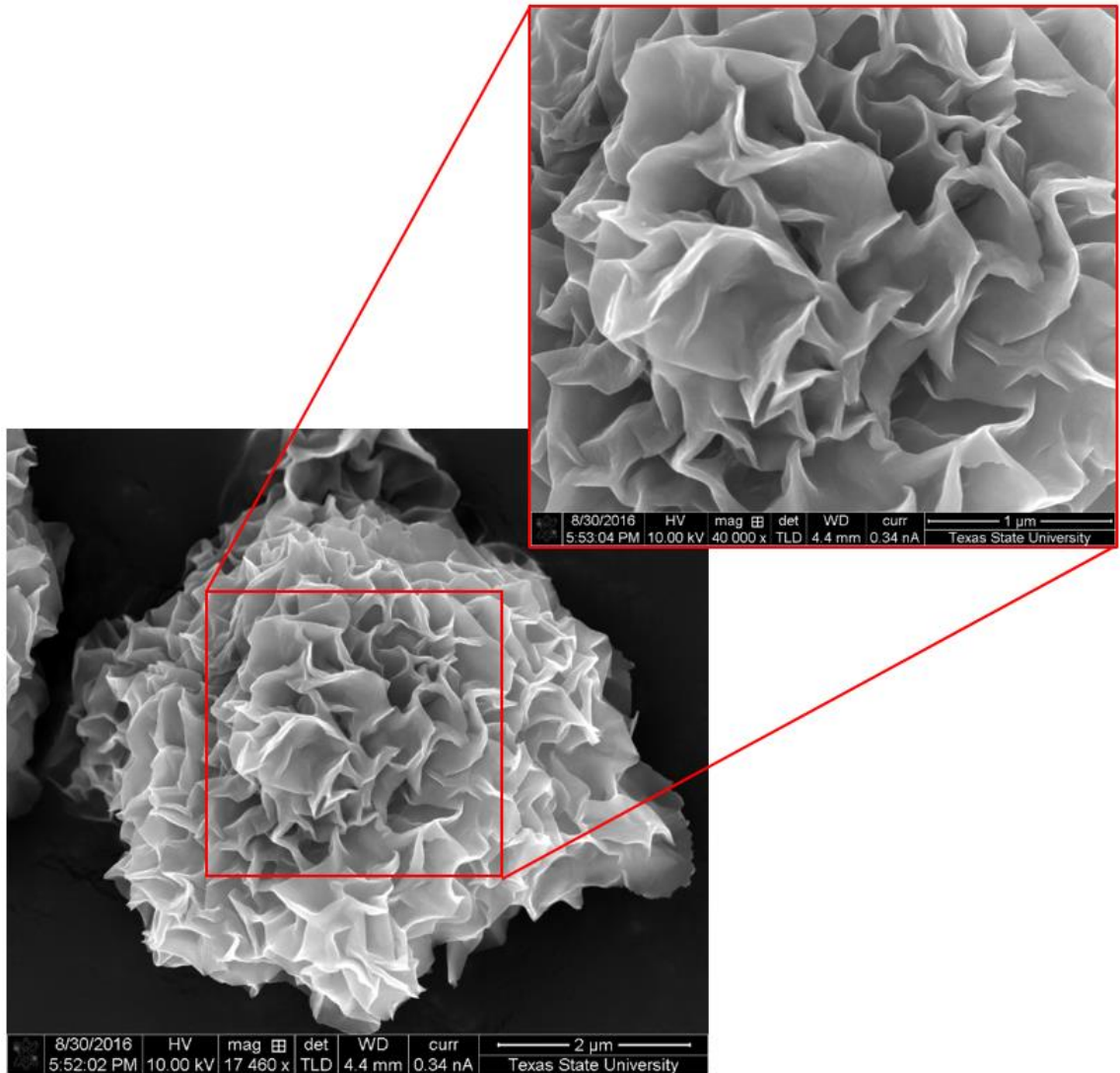


Fig. 64 FESEM images of MMT (M3) produced after 10h milling and subsequent autoclave treatment at 260°C for 72h.

Fig. 65 presents the TEM images of MMT (M3) prepared after 10h milling and subsequent autoclave treatment at 260°C for 72h. From the lower magnification, it can be seen the typical lamellar structure of MMT in a sheet on-sheet manner, showing the flexibility of these clay platelets and high aspect ratio [109]. As revealed by the high magnification figure, the MMT lamellae with an average size about 500 nm to 1μm long and 10–20 nm thick can be readily observed. Note that the initial milling not only did not destroy the platelet structure, but also cause to increase the particle size of MMT after

hydrothermal treatment. This can be of great interest in synthesis of clay based nanocomposite coating for oxygen barrier application.

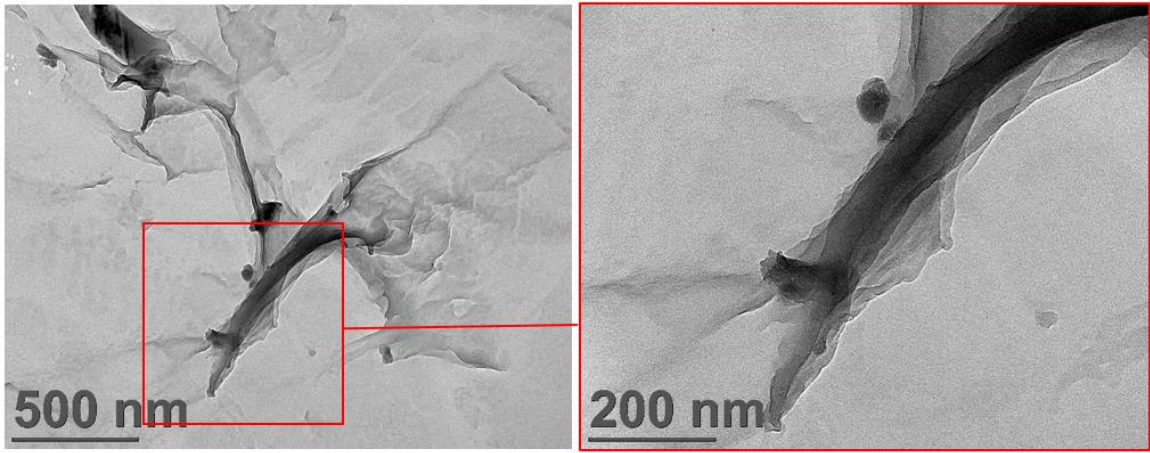


Fig. 65 TEM images of MMT (M3) prepared after 10h milling and subsequent autoclave treatment at 260°C for 72h.

Fig. 66 exhibits the EDS spectrum of MMT (M3) produced after 10h milling and subsequent autoclave treatment at 260°C for 72h. Based on the obtained data, the main components of the sample were oxygen, sodium, magnesium, aluminum, silicon, and carbon, confirming the presence of all elements in MMT. The EDS result validates the purity of final composition of MMT without trace of chemically stable impurities. From the average values of three points, the total amount of sodium, magnesium, aluminum, and silicon present in MMT were 2.08%, 2.45%, 13.73%, and 29.64%, which were close and comparable with the accepted values (Na:2.07%, Mg:2.18%, Al:12.28%, and Si:30.61%), respectively. This indicates the formation of a homogenous microstructure of MMT produced by wet MC and following autoclave treatment.

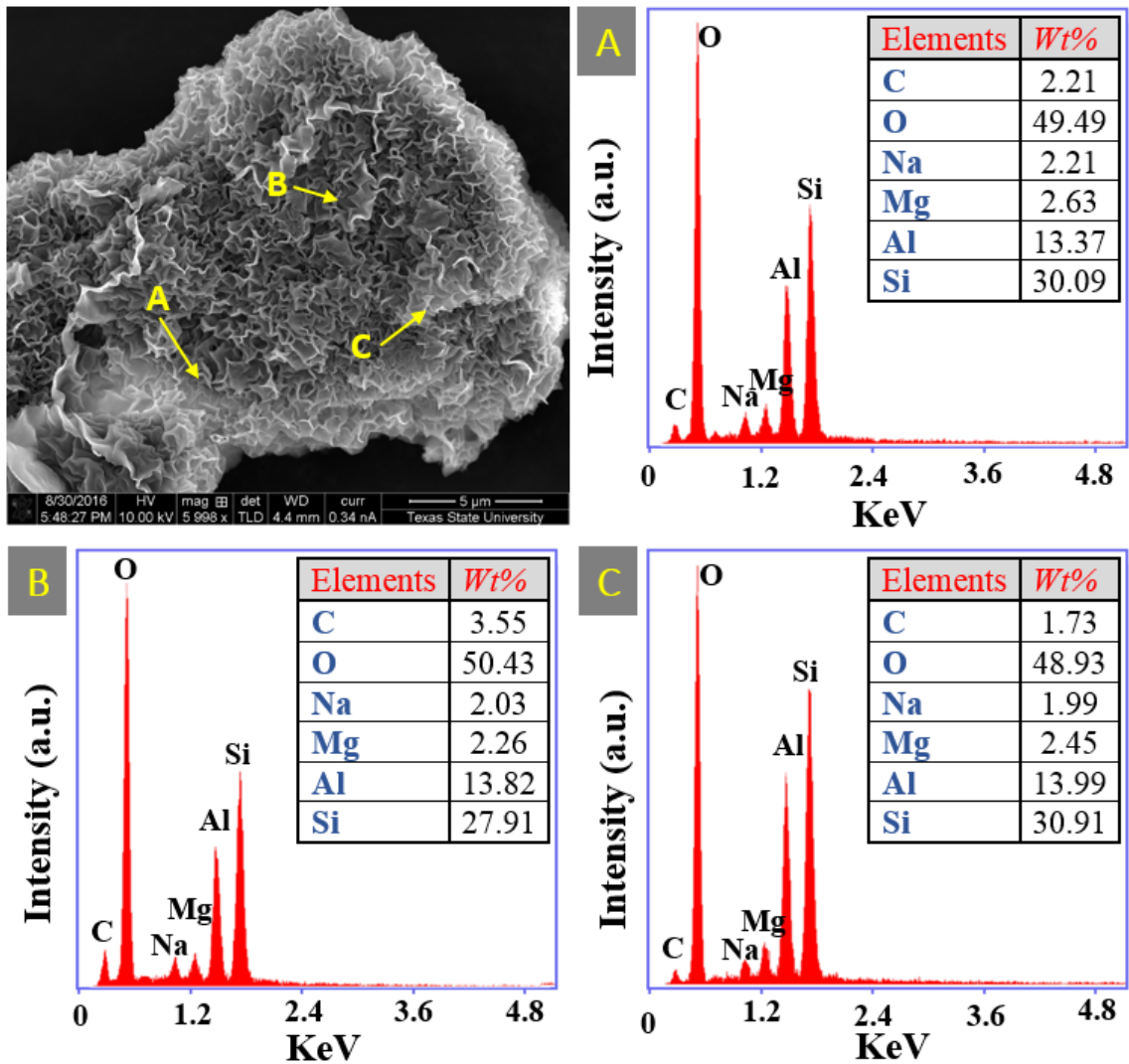


Fig. 66 EDS spectrum of MMT (M3) produced after 10h milling and subsequent autoclave treatment at 260°C for 72h.

6.2.4. Thermogravimetric analysis

The differential thermogravimetric analysis (DTGA) of sample milled for 10h followed by autoclave treatment for 72h at 260 °C (M3) is displayed in Fig. 67. It can be observed that there are three mass losses during heating of MMT sample. The first and greatest mass loss of 17.35% centered at 55.4 °C (25–100 °C) is attributed to the elimination of adsorbed water (surface and interlayer) [98], and the surface property transformation of montmorillonite from hydrophilic to hydrophobic [110]. The second

mass loss of around 2.5% was obtained between 400 and 550 °C centered at 484.3 °C, which corresponding to the interlayer water loss of MMT in the specimen. The final decomposition from 550 °C to 700 °C with a mass loss of 1.88% is attributed to the dehydroxylation or release of structural hydroxyl (OH) of MMT [111]. The total mass loss at 800 °C was about 21.73%. The all mass losses particularly the last one centered at 620.5 °C is equivalent to MMT prepared through hydrothermal means [110]. In this research, the thermal degradation behavior from TGA analysis proposes successful formation of MMT via our new method.

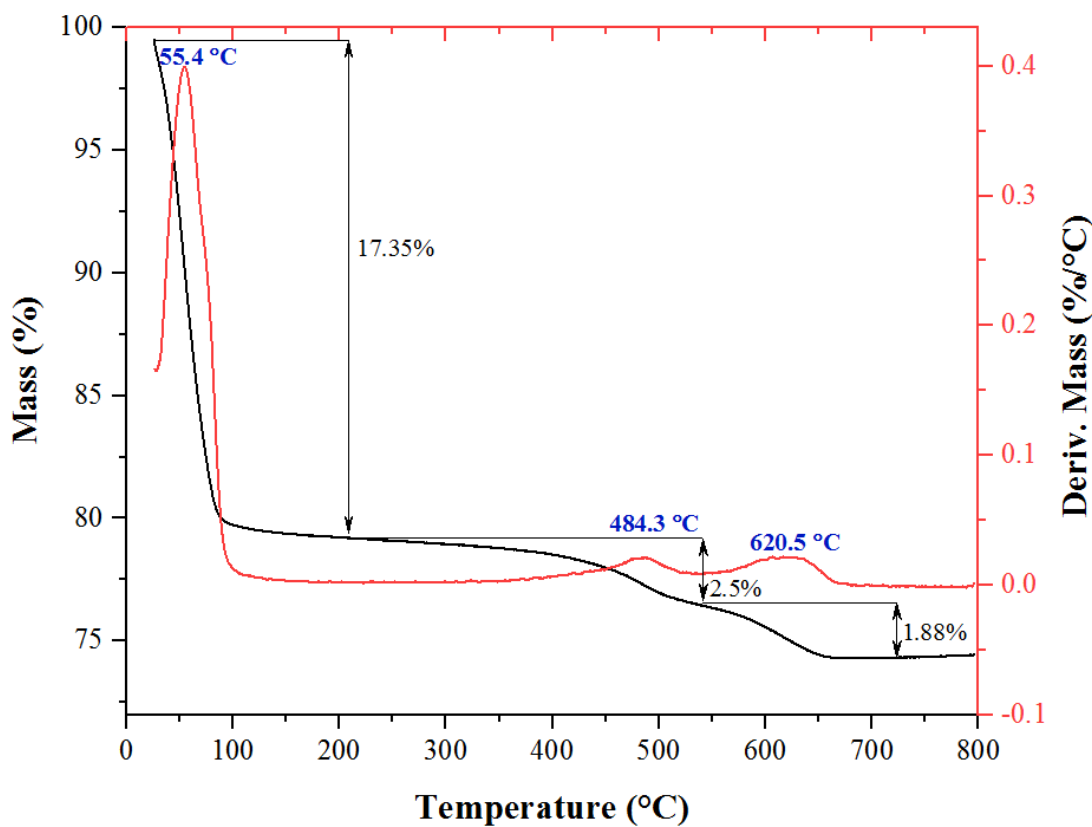


Fig. 67 DTGA curve of sample milled for 10h and followed by autoclave treatment for 72h at 260 °C (M33).

6.3. Conclusions

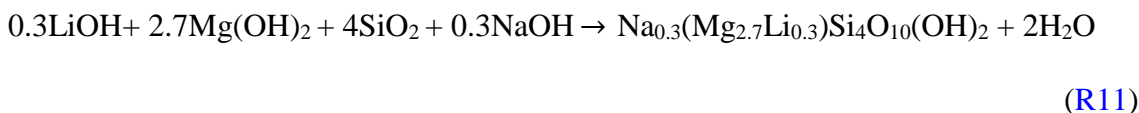
This research presents an overview of MMT production through solid state method. Based on phase analyses, an amorphous solid solution was obtained after 10h milling, and by applying subsequent autoclave treatment on the milled powders, high crystalline MMT was appeared. This indicates that the amorphous solid solution has been transformed into crystalline MMT phase. A MMT phase with higher crystallinity was obtained at longer autoclaving time period 72h (M3), clearly indicating a reflection d_{001} with higher intensity. From the EDS and FTIR spectra, all the bands corresponding to MMT are evident in all autoclave times, demonstrating the formation of MMT with no trace of carbonate ions and appropriate purity. The morphology of synthetic MMT particles appears in the form of microlayers twisted in a rose-shaped platy structure with an average size about 500 nm to 1 μ m long and 10–20 nm thick. The thermal degradation behavior from DTGA analysis presented three mass losses, and proposed successful formation of MMT via our new method. MMT with better morphological characteristics having greater particles sizes provides a great potential to synthesis of new nanocomposites for many applications.

7. HECTORITE

In this chapter, the production of Hectorite (HEC) using wet mechanochemistry method was investigated. Besides, the effect of subsequent autoclave treatment on the milled samples was evaluated. The structural characteristics and morphological features of products have been studied for different milling times and conditions. Specimens were also characterized by XRD, FTIR, FESEM, EDS, TEM, and DTGA. The phase behavior and structural trends was also scrutinized in details. Likewise, the thermal decomposition details of HEC were examined and reported.

7.1. Experimental procedure

Hectorite synthesis started with wet mixing the powders (2 g) including Magnesium hydroxide (99 %, Sigma-Aldrich), lithium hydroxide (99 %, Sigma-Aldrich), silica gel (99 %, Sigma-Aldrich), and Sodium Hydroxide (Sigma-Aldrich), followed by adding 0.8 ml deionized water to the powder mixture. The samples were milled for different milling times (5 and 10h) in a high energy ball mill using hardened chromium steel vials (65 ml volume) under air atmosphere. The ball-to-powder ratio (BPR) for both specimens was kept as 10:1. The samples milled at different milling times were labeled as H1 (5h), and H2 (10h). The final composition of powders was adjusted following reaction (R11):



The 0.5 g powders of milled sample (H2) were poured in 15 ml deionized water and stirred in 50 ml beaker under constant stirring for 10 min using a magnetic stirrer.

Then, the slurry was placed in autoclave chamber (25 ml volume) and was kept in an oven at 260°C for 24h and 48h. Finally, the slurry was poured on a paper filter, and then were dried under oven at 60°C for 1h. The autoclaved samples were labeled as H3, and H4.

7.2. Result and Discussion

7.2.1. XRD analysis

Fig. 68 displays the diffraction patterns of the mixtures grounded for two milling times (5 and 10h). Based on the XRD profiles, a broad amorphous hump of silica, and sharp peaks of brucite co-exist after 5h milling treatment (H1). Furthermore, the peaks representative of sodium hydroxide and lithium hydroxide were not detected due to lower concentration. The XRD patterns of brucite disappeared as the milling time increased to 10h (H2), and a poorly crystalline HEC appeared confirming the formation of HEC using wet MC method. Besides, two small peaks corresponding to Fe contamination were obtained because of excessive wear of balls and vials. Thus, controlling of milling time at about 10h is a significant key to synthesize HEC mechanochemically. Our synthetic HEC, the mechanochemically induced HEC, is comparable with Laponite, which is a commercially available synthetic hectorite known to have a small particle size [112]. In addition, the basal spacing peak in XRD pattern was not displayed, which is the same as Laponite XRD pattern [113, 112, 114].

By applying autoclave treatment on the milled sample for two duration times (H3:24h, and H4:48h), a high crystalline HEC was formed. HEC with Li⁺ as exchangeable cations exhibited a basal spacing of 11.3 Å for H4 sample. This basal

spacing is very close to the value of HEC reported by Pawar et al. [115] in which HEC obtained using hydrothermal process. Peaks at 4.6 Å (~ 19.5° 2θ), 2.5 Å (35.8° 2θ), 1.7 Å (53° 2θ), and 1.5 Å (60.7° 2θ) represented the [(110), (020)], [(130), (200)], [(150), (240), (310)], and [(060), (330)] reflections of hectorite, respectively [115].

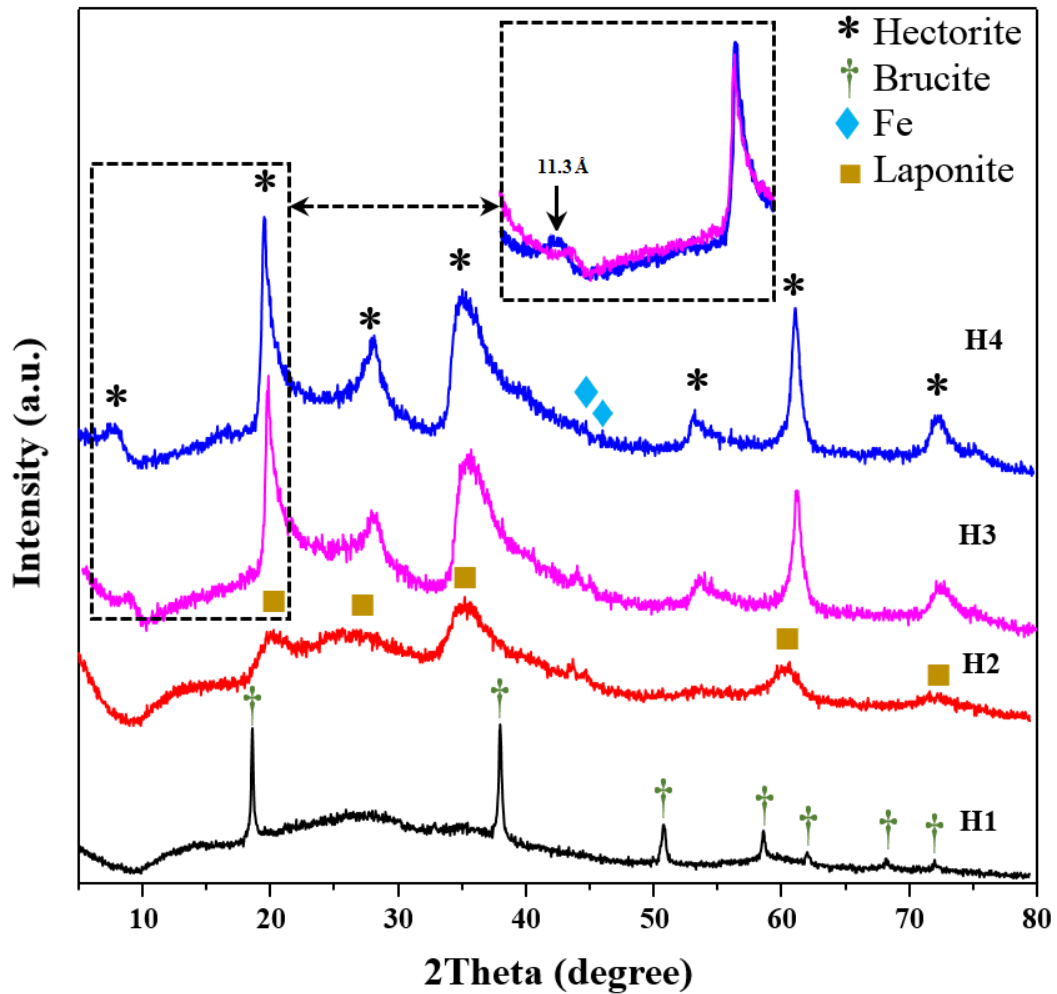


Fig. 68 XRD profiles of the mixtures grounded for two milling times: (H1:5h, and H2:10h), and the autoclaved samples as a function of time: (24h:H3, and 48h:H4).

From a close-up section of diffraction at angles 5-20° (2θ), the results also indicate that autoclave duration for shorter time (H3) affected the basal space and shifted it to the lower value (10.1 Å), which may impact cation exchange properties. The (060) values of

H3 and H4 were determined to be nearly 1.52 Å, confirming the trioctahedral nature of synthesized samples [115]. Therefore, it can be concluded that a single phase of Laponite was formed using MC method, while high crystalline HEC was the product of MC and subsequent autoclave means.

7.2.2. FTIR analysis

FTIR spectra of powders milled for 10h (H2), and subsequent autoclave treatment on the milled powders for two different times (H3:24h, and H4:48h) are collected in Fig. 69. Although the XRD data illustrate the formation of synthetic Laponite after 10h of wet milling, and HEC after autoclave treatment, a clear identification can be made by FTIR. FTIR spectrum of H2 exhibits a broad band at around 3400–3700 cm^{-1} , which is usually assigned to the stretching and bending of surface hydroxyl groups and sorbed water [116]. Moreover, the bending vibrations of adsorbed water in the interlayer Laponite can be also seen at 1639 cm^{-1} . The presence of peaks at 1422 cm^{-1} (ν_3), and 1384 cm^{-1} (ν_2) was recognized as asymmetric stretching modes of CO_3^{2-} , confirming the absorption of CO_2 from the atmosphere during milling process [64]. The peaks centered at 1013, 910 and 462 cm^{-1} , are classified as Si–O bond, Si–O stretching mode, and Si–O–Si bending vibrations, respectively [117, 118]. Note that the Si–O stretching at 1013 cm^{-1} in the 2:1 layer silicates shows the dioctahedral minerals [119]. The peaks observed at 6 the bending vibrations of adsorbed water in the interlayer Laponite can be also seen at 1639 [117]. The spectra of two autoclaved samples (H3, and H4) show very similar peaks as compared with milled one (H2), however the band at 910 cm^{-1} was vanished in H3 and H4. In addition, the peaks centered at 624 and 646 cm^{-1} shifted to 670 cm^{-1} in H4, which

associate to inplane OH bending [120]. There were two more bands at 3624 and 1110 cm^{-1} in H4, which can be attributed to the MgLi-OH and Si-O stretching vibrations [115]. Therefore, higher autoclave time (48h) demonstrate a clay structure resembling the spectrum of HEC.

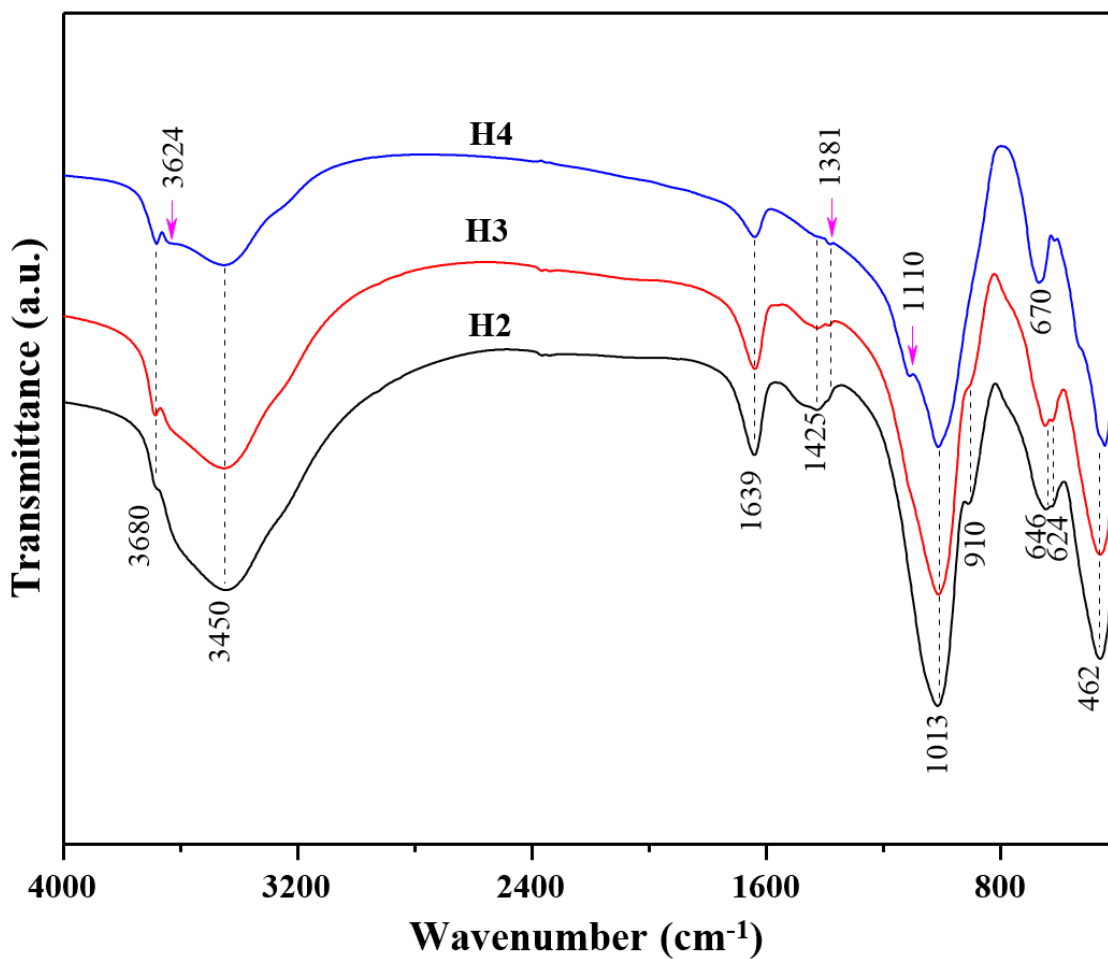


Fig. 69 FTIR spectra of powders milled for 10h (H2), and subsequent autoclave treatment on the milled sample for two different times (H3:24h, and H4:48h).

7.2.3. Morphological characterization

Fig. 70 displays the FESEM images of HEC prepared after 10h milling and subsequent autoclave treatment for 48h (H4). From the lower magnification, the morphology of synthetic HEC appears in the form of microlayers twisted in a large

quantity of flower-like branched structure. As evident from the close-up part, this unique structure had homogenous leaf-like microstructures with a leaf thickness of about 35 nm. It is interesting to note that the average pore diameters were around 2 μm , which was much larger than those synthesized via microwave [121], Hydrothermal [122], and template free route means [123].

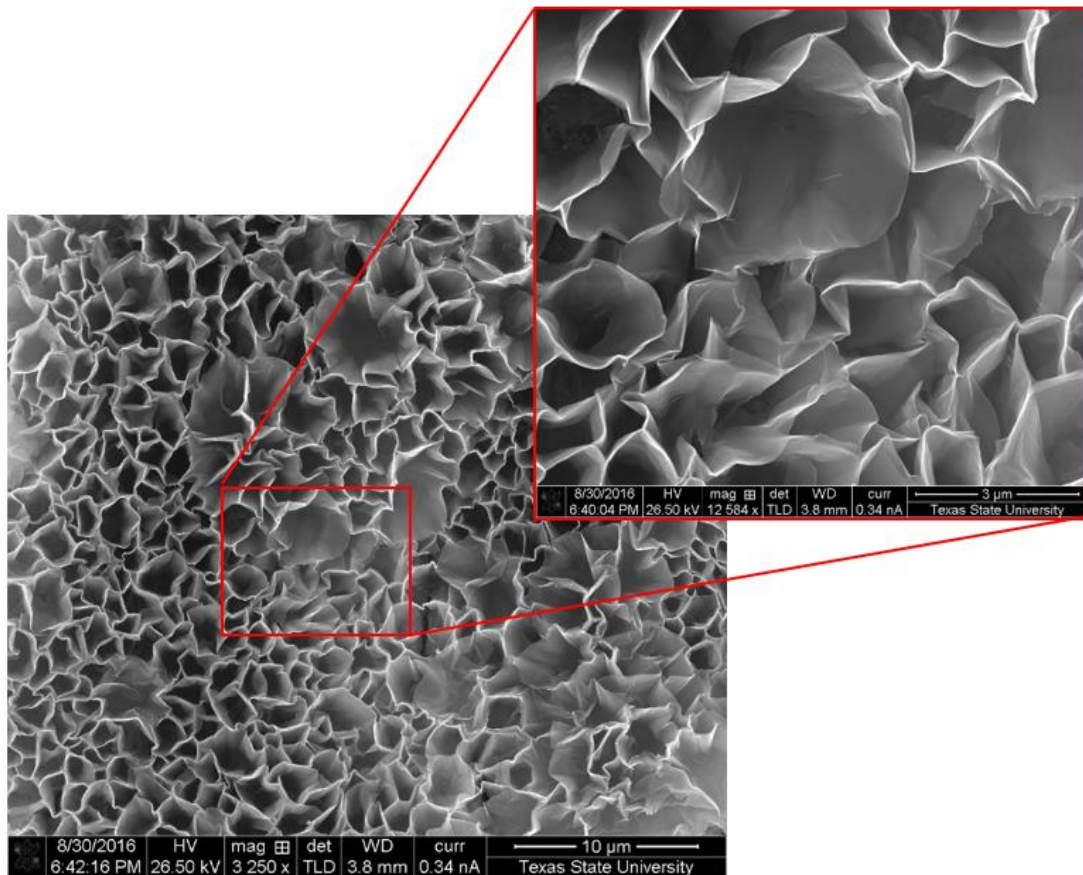


Fig. 70 FESEM images of HEC (H4) prepared after 10h milling and subsequent autoclave treatment for 48h.

Fig. 71 presents the TEM image of HEC prepared after 10h milling and subsequent autoclave treatment for 48h (H4). It can be observed the typical lamellar structure of HEC with long-ranged stacked layers in a sheet on-sheet manner, indicating high delamination of the sheets. The HEC lamellae with an average size about 2 μm long

and 30 nm thick can be readily observed. The synthetic HEC particle size in this study was much greater than natural HEC (~ 372 nm in length, 50 nm in width, and 1 nm in thickness) [124]. The micrographs are in good agreement with SEM results as well. This morphology with layered structure provides a great potential to synthesis of new HEC based nanocomposites for many applications.

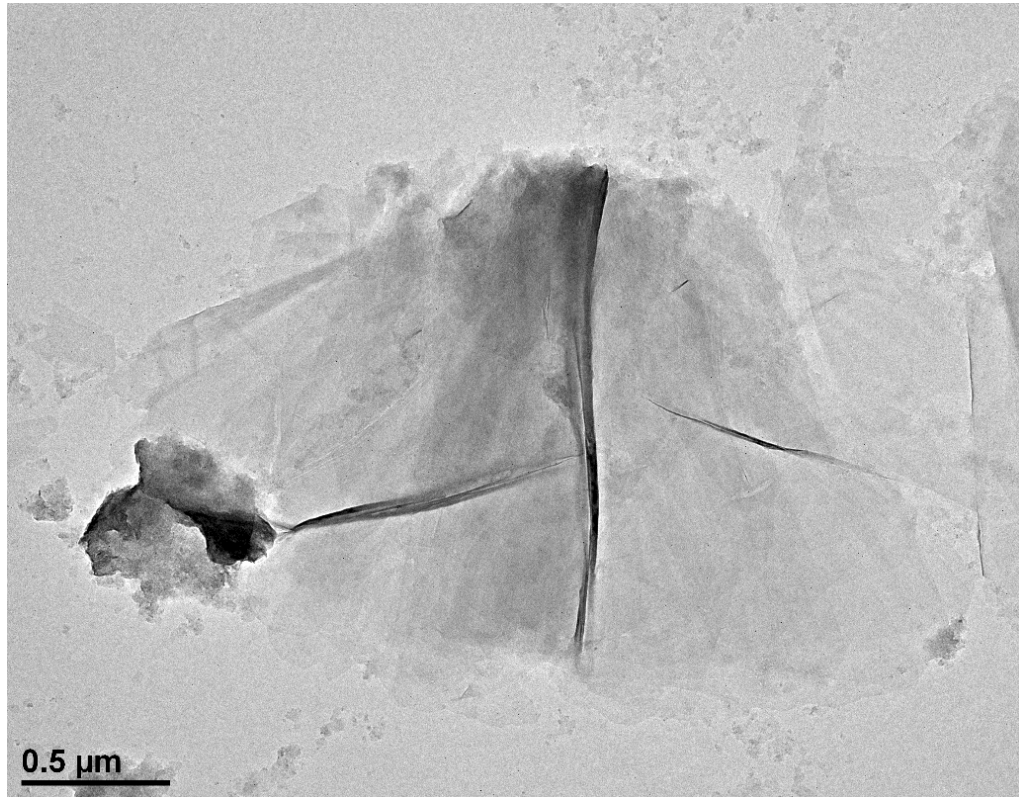


Fig. 71 TEM image of HEC prepared after 10h milling and subsequent autoclave treatment for 48h (H4).

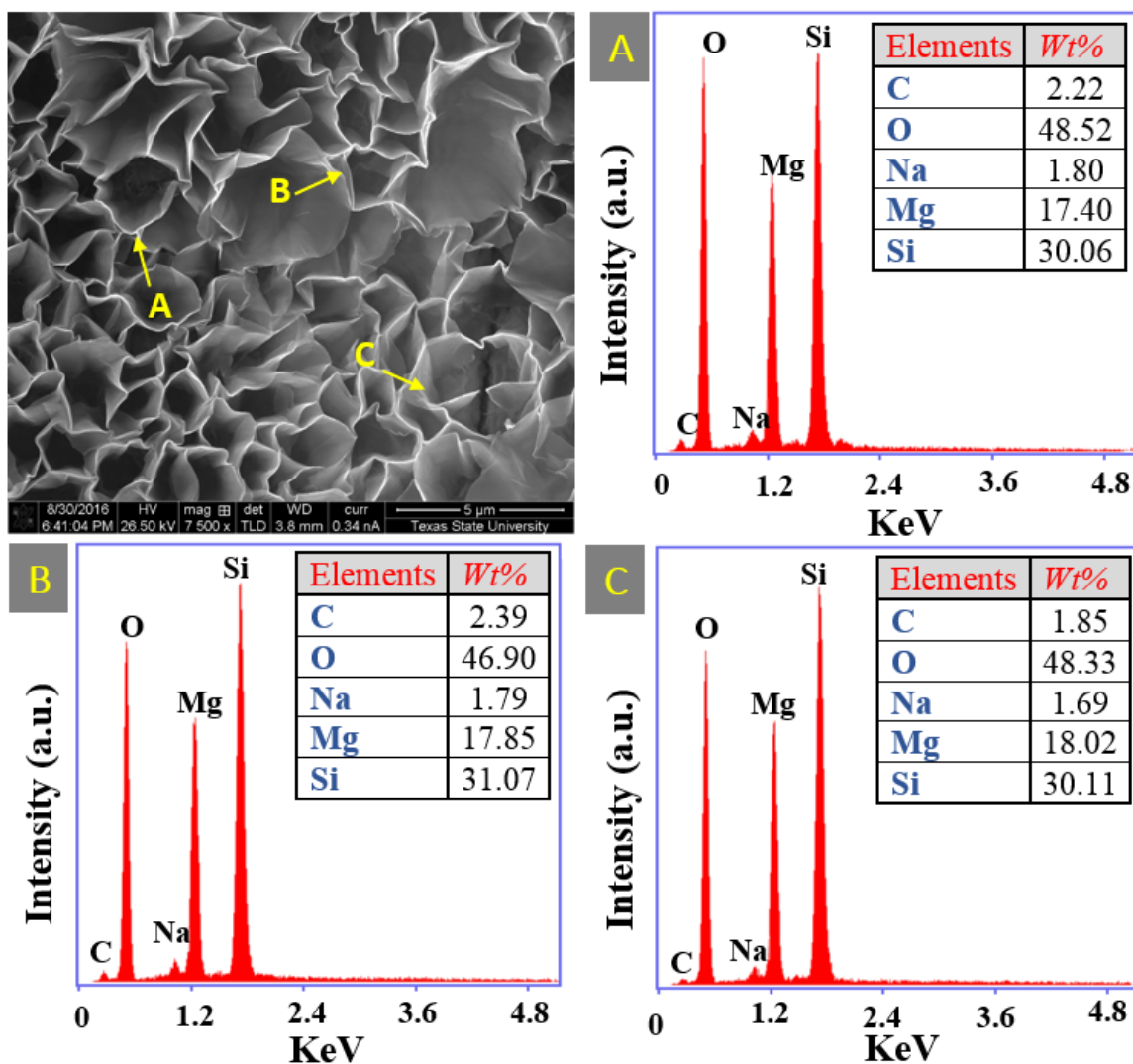
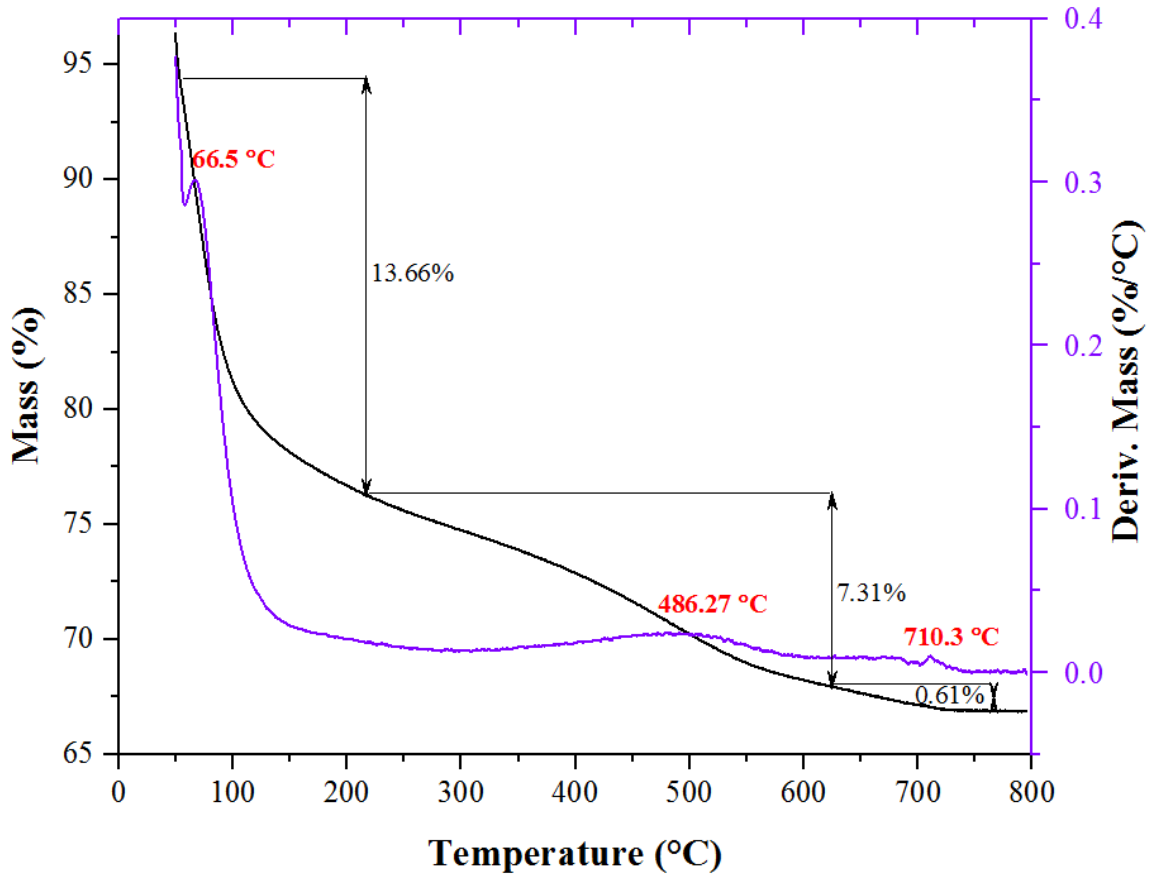


Fig. 72 EDS spectrum of HEC prepared after 10h milling and subsequent autoclave treatment for 48h (H4).

Fig. 72 shows EDS spectrum of HEC (H4) produced by MC and subsequent autoclave treatment process. According to the obtained data, the main components of the H4 sample were oxygen, sodium, magnesium, silicon, and carbon, confirming all elements present in HEC. The EDS result confirms the purity of final composition of HEC without trace of chemically stable impurities. Based on the average values of three points, the total amount of sodium, magnesium, and silicon present in HEC were obtained

as 1.76%, 17.76%, and 30.41%, respectively, which were close and similar with the accepted values (Na:1.81%, Mg:17.23%, and Si:29.49%), respectively. This confirms the successful formation of HEC produced by wet MC and following autoclave treatment.

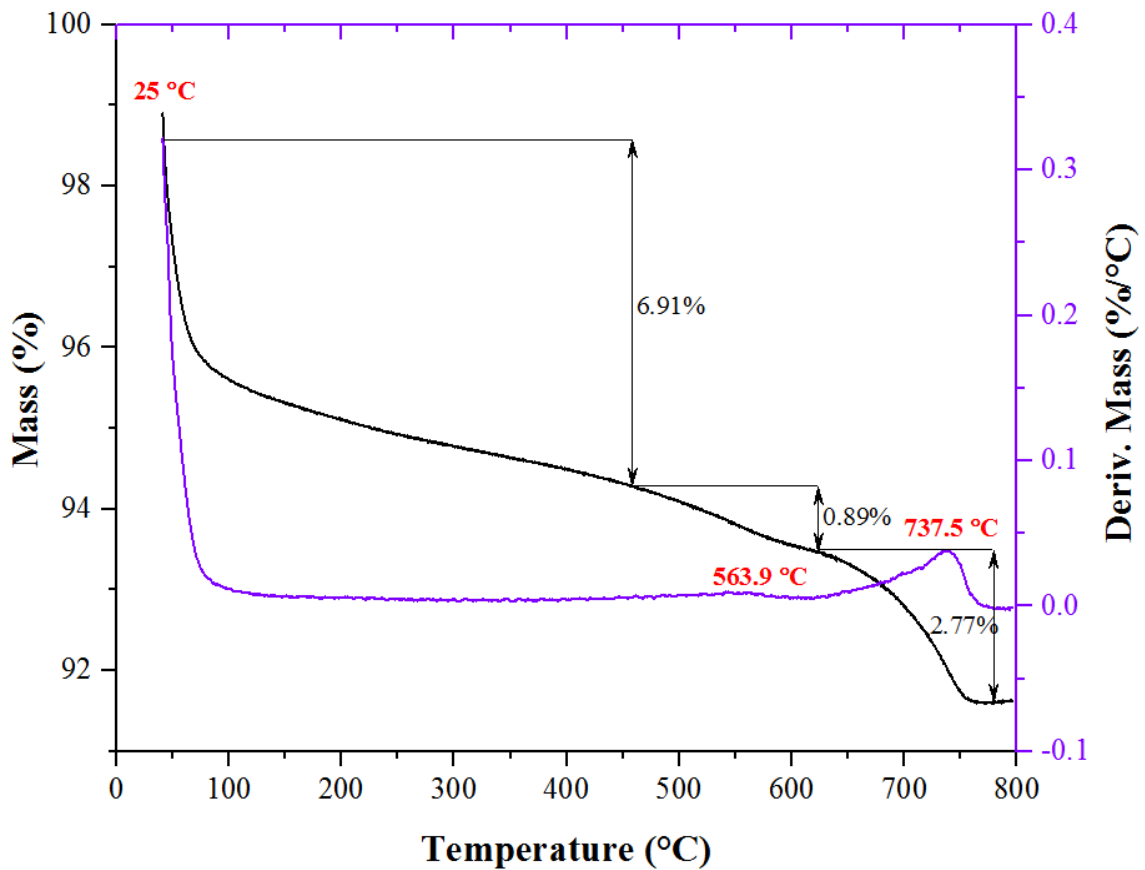


Figs. 73 DTGA curve of sample milled for 10h (H2).

7.2.4. Thermogravimetric analysis

Figs. 73 and **74** provide the differential thermogravimetric analysis (DTGA) of samples milled for 10h (H2), and subsequent autoclave treatment for 48h (H4) on the milled sample, respectively. According to **Fig. 73**, It can be seen that there were three distinct mass losses during heating of milled sample (H2). The first mass loss of 13.6%

appears between 25 to 100 °C can be assigned to the removal of adsorbed and hydration water molecules on the surface of layers [43]. The second mass loss of 7.3%, remarked in the temperature range of 350–650 °C, corresponds to the interlayer water loss of clay in the specimen. The final decomposition from 600 °C to 800 °C with a mass loss of 0.6% is attributed to the dehydroxylation of clay structure. Hence, all three mass losses represent a thermal decomposition of clay structure resembling Laponite with total mass losses of 21.6% at 800 °C [125, 126]. The results were good agreement with XRD and FTIR outcomes.



Figs. 74 DTGA graph of sample milled for 10h followed by subsequent autoclave treatment for 48h (H4).

As evident from **Fig. 74**, the thermal decomposition of H4 occurred in three consecutive steps between 25–450 °C, 450–650 °C, and 650–800 °C, which were about

6.9%, 0.9%, and 2.8%, respectively. As mentioned above, the first mass loss was associated to the loss of surface water, while the second and third ones can be assigned to the release of interlayer water and dehydroxylation of clay structure, respectively. The total mass loss for H4 at 800 °C was about 10.6%. The DTGA results indicates that the thermal degradation behavior of H4 is equivalent to HEC [127], which were previously evidenced by XRD and FTIR results.

7.3. Conclusions

This research section reports the successful preparation of poorly crystalline HEC (Laponite) through wet MC process and High crystalline HEC via following autoclave treatment. The morphology of synthetic HEC appears in the form of microlayers twisted in a large quantity of flower-like branched structure with an average leaf thickness of about 35 nm and 2 μm long. The EDS result confirms the purity of final composition of HEC without trace of chemically stable impurities. DTGA data showed three mass losses represent a thermal decomposition of clay structure resembling HEC. The synthetic HEC reported here with layered structure would provide a great potential to synthesis of new HEC based nanocomposites for many applications.

8. SUMMARY

This research focused on the synthesis, and characterization of anionic, non-ionic, and cationic clay materials via mechanochemical means, which is facile, simple, inexpensive, and solvent free method. Structural features, morphological characterization, and thermal behavior of products based on various synthesis conditions (e.g. the effect of ion substitution and synthesis parameters on the porosity and textural characteristics of synthetic clays) have been studied. The subsequent autoclaving process on the non-ionic and cationic samples were also evaluated which resulted in crystallinity growth of products and in some cases led to production of clays. The products were characterized by XRD, FTIR, FESEM, EDS, elemental mapping analysis, TEM, XRF, and DTGA. In this project, we successfully prepared anionic clays (e.g. HT, and HC), non-ionic (e.g. Talc and KAO), and cationic clays (e.g. MMT, and HEC). Our results reveal that anionic clays (e.g. HT and HC), and poor crystalline talc and HEC can be successfully produced through one pot mechanochemistry method, while high crystalline talc, HEC, and MMT were produced after subsequent autoclave process. Moreover, KAO with two distinct morphologies and proper crystallinity was obtained instead of PP and HS clays. The results presented in this dissertation provided a plethora of new information, some of which challenge old dogmas. One of the main contributions of this study was to demonstrate, for the first time, that cationic clays (MMT, HEC) can be synthesized with particle sizes around 1-2 μm . It is interesting to note that other methods like Hydrothermal and precipitation are unable to produce those clays with particle size more than 50 nm, which affects significantly their properties. These synthetic clays are 2-D layered materials of significant potential for environmental and industrial applications.

8.1. Future work

The results of this research have proved that mechanochemistry is an effective method for preparation of 2D layered materials. Therefore, this simple process will provide a great potential for synthesis of clays based nanocomposites. Further characterization of mechanically induced clays would be helpful in elucidating the basal spacing of the sheets, possibly through high resolution transmission electron microscopy (HRTEM). It would also be useful to know and calculate the minimum energy used for ion substitutions via molecular dynamics [128] and compare the results with the data obtained through other characterization techniques like XRD. Other synthesis parameters should be also examined to obtain the optimum conditions for production of clays. The properties of clays should be studied including rheology properties, barrier properties, etc. Commercialization of divers clays should also be assessed based on a comparison of the cost and availability of ball mill in industrial scale, and the starting material of clays. These analyses would be valuable for targeting potential commercial applications of clays.

APPENDIX SECTION

Section A. Publications

1. **Abbas Fahami**, Gary W. Beall, S. Enayatpour, F. Tavangarian, M. Fahami “Rapid preparation of nano hexagonal-shaped hydrocalumite via one-pot mechanochemistry method”, *Applied Clay Science*, 136 (2017) 90-95.
2. **Abbas Fahami**, Gary W. Beall, “Structural and morphological characterization of $Mg_{0.8}Al_{0.2}(OH)_2Cl_{0.2}$ hydrotalcite produced by Mechanochemistry method”, *Journal of Solid State Chemistry*, 233 (2016) 422–427.
3. **Abbas Fahami**, Gary W. Beall, “Mechanosynthesis and characterization of Hydrotalcite like Mg-Al-SO₄-LDH”, *Materials Letters*, 165, 15, (2016) 192–195.
4. **Abbas Fahami**, Gary W. Beall, Synthesis and Characterization of Hydrotalcite like Compound via a Facile Solid State Method, *MRS Advances* (2016).
5. **Abbas Fahami**, FS Al-Hazmi, AA Al-Ghamdi, WE Mahmoud, Gary W Beall, Structural characterization of chlorine intercalated Mg-Al layered double hydroxides: A comparative study between mechanochemistry and hydrothermal methods, *Journal of Alloy and Compound*, (2016) 100–107.

Section B. Letters of permission from publishers

CAMBRIDGE UNIVERSITY PRESS ORDER DETAILS

Feb 10, 2017

This Agreement between ("You") and Cambridge University Press ("Cambridge University Press") consists of your order details and the terms and conditions provided by Cambridge University Press and Copyright Clearance Center.

Order Number	501230908
Order date	Feb 02, 2017
Licensed Content Publisher	Cambridge University Press
Licensed Content Publication	MRS Advances
Licensed Content Title	Synthesis and Characterization of Hydrotalcite like Compound via a Facile Solid State Method
Licensed Content Author	Abbas Fahami, Gary W. Beall
Licensed Content Date	Jun 30, 2016
Licensed Content Volume	1
Licensed Content Issue	36
Start page	2557
End page	2562
Type of Use	Dissertation/Thesis
Requestor type	Author
Portion	Full article
Author of this Cambridge University Press article	Yes
Author / editor of the new work	No
Order reference number	
Territory for reuse	North America Only
Title of your thesis / dissertation	MECHANOCHEMICAL ACTIVATION OF SYNTHETIC NANOSIZED 2-D LAYERED MATERIALS: PREPARATION AND CHARACTERIZATION
Expected completion date	Aug 2017
Estimated size(pages)	200
Requestor Location	Abbas Fahami 101 Fenway Loop SAN MARCOS, TX 78666 United States Attn: Abbas Fahami
Publisher Tax ID	GB823847609
Billing Type	Invoice
Billing Address	Abbas Fahami 101 Fenway Loop

**ELSEVIER LICENSE
TERMS AND CONDITIONS**

Feb 02, 2017

This Agreement between Abbas Fahami ("You") and Elsevier ("Elsevier") consists of your license details and the terms and conditions provided by Elsevier and Copyright Clearance Center.

License Number	4040621030124
License date	Feb 02, 2017
Licensed Content Publisher	Elsevier
Licensed Content Publication	Applied Clay Science
Licensed Content Title	Rapid preparation of nano hexagonal-shaped hydrocalumite via one-pot mechanochemistry method
Licensed Content Author	Abbas Fahami,Gary W. Beall,Saeid Enayatpour,Fariborz Tavangarian,Mohammad Fahami
Licensed Content Date	February 2017
Licensed Content Volume Number	136
Licensed Content Issue Number	n/a
Licensed Content Pages	6
Start Page	90
End Page	95
Type of Use	reuse in a thesis/dissertation
Portion	full article
Format	both print and electronic
Are you the author of this Elsevier article?	Yes
Will you be translating?	No
Order reference number	
Title of your thesis/dissertation	MECHANOCHEMICAL ACTIVATION OF SYNTHETIC NANOSIZED 2-D LAYERED MATERIALS: PREPARATION AND CHARACTERIZATION
Expected completion date	Aug 2017
Estimated size (number of pages)	200
Elsevier VAT number	GB 494 6272 12
Requestor Location	Abbas Fahami 101 Fenway Loop SAN MARCOS, TX 78666 United States Attn: Abbas Fahami

**ELSEVIER LICENSE
TERMS AND CONDITIONS**

Feb 02, 2017

This Agreement between Abbas Fahami ("You") and Elsevier ("Elsevier") consists of your license details and the terms and conditions provided by Elsevier and Copyright Clearance Center.

License Number	4040630124232
License date	Feb 02, 2017
Licensed Content Publisher	Elsevier
Licensed Content Publication	Journal of Alloys and Compounds
Licensed Content Title	Structural characterization of chlorine intercalated Mg-Al layered double hydroxides: A comparative study between mechanochemistry and hydrothermal methods
Licensed Content Author	Abbas Fahami, F.S. Al-Hazmi, A.A. Al-Ghamdi, W.E. Mahmoud, Gary W. Beall
Licensed Content Date	25 October 2016
Licensed Content Volume Number	683
Licensed Content Issue Number	n/a
Licensed Content Pages	8
Start Page	100
End Page	107
Type of Use	reuse in a thesis/dissertation
Intended publisher of new work	other
Portion	full article
Format	both print and electronic
Are you the author of this Elsevier article?	Yes
Will you be translating?	No
Order reference number	
Title of your thesis/dissertation	MECHANOCHEMICAL ACTIVATION OF SYNTHETIC NANOSIZED 2-D LAYERED MATERIALS: PREPARATION AND CHARACTERIZATION
Expected completion date	Aug 2017
Estimated size (number of pages)	200
Elsevier VAT number	GB 494 6272 12
Requestor Location	Abbas Fahami 101 Fenway Loop

**ELSEVIER LICENSE
TERMS AND CONDITIONS**

Feb 02, 2017

This Agreement between Abbas Fahami ("You") and Elsevier ("Elsevier") consists of your license details and the terms and conditions provided by Elsevier and Copyright Clearance Center.

License Number	4040891402753
License date	Feb 02, 2017
Licensed Content Publisher	Elsevier
Licensed Content Publication	Journal of Solid State Chemistry
Licensed Content Title	Structural and morphological characterization of Mg _{0.8} Al _{0.2} (OH) ₂ Cl _{0.2} hydrotalcite produced by mechanochemistry method
Licensed Content Author	Abbas Fahami, Gary W. Beall
Licensed Content Date	January 2016
Licensed Content Volume Number	233
Licensed Content Issue Number	n/a
Licensed Content Pages	6
Start Page	422
End Page	427
Type of Use	reuse in a thesis/dissertation
Intended publisher of new work	other
Portion	full article
Format	both print and electronic
Are you the author of this Elsevier article?	Yes
Will you be translating?	No
Order reference number	
Title of your thesis/dissertation	MECHANOCHEMICAL ACTIVATION OF SYNTHETIC NANOSIZED 2-D LAYERED MATERIALS: PREPARATION AND CHARACTERIZATION
Expected completion date	Aug 2017
Estimated size (number of pages)	200
Elsevier VAT number	GB 494 6272 12
Requestor Location	Abbas Fahami 101 Fenway Loop

SAN MARCOS, TX 78666

**ELSEVIER LICENSE
TERMS AND CONDITIONS**

Feb 02, 2017

This Agreement between Abbas Fahami ("You") and Elsevier ("Elsevier") consists of your license details and the terms and conditions provided by Elsevier and Copyright Clearance Center.

License Number	4040891158665
License date	Feb 02, 2017
Licensed Content Publisher	Elsevier
Licensed Content Publication	Materials Letters
Licensed Content Title	Mechanosynthesis and characterization of Hydrotalcite like Mg-Al-SO ₄ -LDH
Licensed Content Author	Abbas Fahami,Gary W. Beall
Licensed Content Date	15 February 2016
Licensed Content Volume Number	165
Licensed Content Issue Number	n/a
Licensed Content Pages	4
Start Page	192
End Page	195
Type of Use	reuse in a thesis/dissertation
Portion	full article
Format	both print and electronic
Are you the author of this Elsevier article?	Yes
Will you be translating?	No
Order reference number	
Title of your thesis/dissertation	MECHANOCHEMICAL ACTIVATION OF SYNTHETIC NANOSIZED 2-D LAYERED MATERIALS: PREPARATION AND CHARACTERIZATION
Expected completion date	Aug 2017
Estimated size (number of pages)	200
Elsevier VAT number	GB 494 6272 12
Requestor Location	Abbas Fahami 101 Fenway Loop SAN MARCOS, TX 78666 United States Attn: Abbas Fahami
Total	0.00 USD

REFERENCES

- [1] K. A. Carrado, J. E. Forman, R. E. Botto and R. E. Winans , "Incorporation of phthalocyanines by cationic and anionic clays via ion exchange and direct synthesis," *Chemistry of Materials*, vol. 5, no. 4, pp. 472-478, 1993.
- [2] A. Sampieri, G. Fetter, M. E. Villafuerte-Castrejon, A. Tejada-Cruz and P. Bosch, "Twofold role of calcined hydrotalcites in the degradation of methyl parathion pesticide," *Beilstein J. Nanotechnol*, vol. 2, pp. 99-103, 2011.
- [3] S. J. Mills, A. G. Christy, J. MR Génin, T. Kameda and F. Colombo, "Nomenclature of the hydrotalcite supergroup: natural layered double hydroxides," *Mineralogical Magazine*, vol. 76, pp. 1289-1336, 2012.
- [4] Q. Wang, H. Tay, Z. Guo, L. Chen, Y. Liu, J. Chang, Z. Zhong, J. Luo and A. Borgna, "Morphology and composition controllable synthesis of Mg–Al–CO₃ hydrotalcites by tuning the synthesis pH and the CO₂ capture capacity," *Appl. Clay Sci.*, vol. 55, pp. 18-26, 2012.
- [5] L. Zheng, S. Xia, X. Lu and Z. Hou, "Transesterification of glycerol with dimethyl carbonate over calcined Ca-Al hydrocalumite," *Chinese J Catal*, vol. 36, pp. 1759-1765, 2015.
- [6] V. Tóth, M. Sipiczki, A. Pallagi, Á. Kukovecz, Z. Kónya, P. Sipos and I. Pálinkó, "Synthesis and properties of CaAl-layered double hydroxides of hydrocalumite-type," *Chemical Papers*, vol. 68, no. 5, pp. 633-637, 2014.

- [7] B. A. Sanderson, D. S. Sowersby, S. Crosby, M. Goss, L. K. Lewis and G. W. Beall, "Charge density and particle size effects on oligonucleotide and plasmid DNA binding to nanosized hydrotalcite," *Biointerphases*, vol. 8, p. 8, 2013.
- [8] S. Yoon, J. Moon, S. Bae, X. Duan, E. P. Giannelis and P. M. Monteiro, "Chloride adsorption by calcined layered double hydroxides in hardened Portland cement paste," *Materials Chemistry and Physics*, vol. 145, no. 3, pp. 376-386, 2014.
- [9] C. F. Linares, J. Moscoso, V. Alzurutt, F. Ocanto, P. Bretto and G. González, "Carbonated hydrocalumite synthesized by the microwave method as a possible antacid,," *Materials Science and Engineering: C*, vol. 61, pp. 875-878, 2016.
- [10] K. Dutta and A. Pramanik, "Synthesis of a novel cone-shaped CaAl-layered double hydroxide (LDH): its potential use as a reversible oil sorbent," *Chemical Communications*, vol. 49, no. 57, pp. 6427-6429, 2013.
- [11] Y. Li, B. Gao, T. Wu, W. Chen, X. Li and B. Wang, "Adsorption kinetics for removal of thiocyanate from aqueous solution by calcined hydrotalcite," *Colloids and Surfaces A: Physicochemical and Engineering Aspects*, vol. 325, no. 1, pp. 38-43, 2008.
- [12] D. Das, J. Das and K. Parida, "Physicochemical characterization and adsorption behavior of calcined Zn/Al hydrotalcite-like compound (HTlc) towards removal of fluoride from aqueous solution," *Journal of Colloid and Interface Science*, vol. 261, no. 2, pp. 213-220, 2003.

- [13] P. Zhang, G. Qian, H. Shi, X. Ruan, J. Yang and R. L. Frost, "Mechanism of interaction of hydrocalumites (Ca/Al-LDH) with methyl orange and acidic scarlet GR," *Journal of Colloid and Interface Science*, vol. 365 , pp. 110-116, 2012.
- [14] F. Kovanda, T. Grygar and V. Dorničák, "Thermal behaviour of Ni–Mn layered double hydroxide and characterization of formed oxides," *Solid State Sciences*, vol. 5, no. 7, pp. 1019-1026, 2003.
- [15] T. Hibino and H. Ohya, "Synthesis of crystalline layered double hydroxides: Precipitation by using urea hydrolysis and subsequent hydrothermal reactions in aqueous solutions," *Applied Clay Science*, vol. 45, no. 3, pp. 123-132, 2009.
- [16] S. P. Paredes, G. Fetter, P. Bosch and S. Bulbulian, "Sol-gel synthesis of hydrotalcite—like compounds," *Journal of materials science*, vol. 41, no. 11, pp. 3377-3382, 2006.
- [17] P. Benito, I. Guinea, F. M. Labajos and V. Rives, "Microwave-assisted reconstruction of Ni, Al hydrotalcite-like compounds," *Journal of Solid State Chemistry*, vol. 181, no. 5, pp. 987-996, 2008.
- [18] F. M. Labajos, V. Rives and M. A. Ulibarri, "Effect of hydrothermal and thermal treatments on the physicochemical properties of Mg-Al hydrotalcite-like materials," *Journal of materials science*, vol. 27, no. 6, pp. 1546-1552, 1992.
- [19] G. K. Williamson and W. H. Hall, "X-ray line broadening from field aluminum and wolfram," *Acta metallurgica* , vol. 1, no. 1, pp. 22-31, 1953.

- [20] A. Fahami, R. Ebrahimi-Kahrizsangi and B. Nasiri-Tabrizi, "Mechanochemical synthesis of hydroxyapatite/titanium nanocomposite," *Solid State Sciences*, vol. 13, no. 1, pp. 135-141, 2011.
- [21] A. Fahami and B. Nasiri-Tabrizi, "Mechanochemical behavior of CaCO₃-P₂O₅-CaF₂ system to produce carbonated fluorapatite nanopowder," *Ceramics International*, vol. 40, no. 9, pp. 14939-14946, 2014.
- [22] B. Nasiri-Tabrizi, A. Fahami and R. Ebrahimi-Kahrizsangi, "Effect of milling parameters on the formation of nanocrystalline hydroxyapatite using different raw materials," *Ceramics International*, vol. 39, no. 5, pp. 5751-5763, 2013.
- [23] C. Suryanarayana, "Mechanical alloying and milling," *Progress in Materials Science*, vol. 46, no. 1-2, pp. 1-184, 2001.
- [24] A. N. Ay, B. Zümreoglu-Karan and L. Mafra, "A Simple Mechanochemical Route to Layered Double Hydroxides: Synthesis of Hydrotalcite-Like Mg-Al-NO₃-LDH by Manual Grinding in a Mortar," *Zeitschrift für anorganische und allgemeine Chemie*, vol. 635, no. 91-10, pp. 1470-1475, 2009.
- [25] V. P. Isupov, L. E. Chupakhine, R. P. Mitrofanova and K. A. Tarasov, "Synthesis, Structure, Properties, and Application of Aluminium Hydroxide Intercalation Compounds," *Chemistry for Sustainable Development*, vol. 8, no. 1-2, pp. 121-127, 2000.
- [26] V. P. Khusnutdinov and V. P. Isupov, "Mechanochemical synthesis of a hydroxycarbonate form of layered magnesium aluminum hydroxides," *Inorganic Materials*, vol. 44, no. 3, pp. 263-267, 2008.

- [27] R. Chitrakar, S. Tezuka, A. Sonoda, K. Sakane, K. Ooi and T. Hirotsu, "A solvent-free synthesis of Zn–Al layered double hydroxides," *Chemistry letters*, vol. 36, no. 3, pp. 446-447, 2007.
- [28] D. French, P. Schifano, J. Cortés-Concepción and S. Hargrove-Leak, "Li–Al layered," *Catalysis Communications*, vol. 12, no. 2, pp. 92-94, 2010.
- [29] Z. Ferencz, M. Szabados, M. Ádok-Sipiczki, Á. Kukovecz, Z. Kónya, P. Sipos and I. Pálinkó, "Mechanochemically assisted synthesis of pristine Ca(II)Sn(IV)-layered double," *Journal of materials science*, vol. 49, no. 24, pp. 8478-8486, 2014.
- [30] Z. Ferencz, Á. Kukovecz, Z. Kónya, P. Sipos and I. Pálinkó, "Optimisation of the synthesis parameters of mechanochemically prepared CaAl-layered double hydroxide," *Applied Clay Science*, vol. 112, pp. 94-99, 2015.
- [31] T. Wang, P. Zhang, D. Wu, M. Sun, Y. Deng and R. L. Frost, "Effective removal of zinc (ii) from aqueous solutions by tricalcium aluminate (C3A)," *Journal of colloid and interface science*, vol. 443, pp. 65-71, 2015.
- [32] J. Qu, L. Zhong, Z. Li, M. Chen, Q. Zhang and X. Liu, "Effect of anion addition on the syntheses of Ca–Al layered double hydroxide via a two-step mechanochemical process," *Applied Clay Science*, vol. 124, pp. 267-270, 2016.
- [33] J. T. Kloprogge, S. Komarneni and J. E. Amonette, "Synthesis of smectite clay minerals: a critical review," *Clays and Clay Minerals*, vol. 47, no. 5, pp. 529-554, 1999.

- [34] R. Chalasani, A. Gupta and S. Vasudevan, "Engineering new layered solids from exfoliated inorganics: a periodically alternating hydrotalcite-montmorillonite layered hybrid," *Scientific reports*, vol. 3, p. 3498, 2013.
- [35] K. G. Satyanarayana, *Clay surfaces: fundamentals and applications*, Academic Press, 2004.
- [36] F. H. Lin, C. H. Chen, W. T. Cheng and T. F. Kuo, "Modified montmorillonite as vector for gene delivery," *Biomaterials*, vol. 27, no. 17, pp. 3333-3338, 2006.
- [37] Q. H. Zeng, A. B. Yu, G. Q. Lu and D. R. Paul, "Clay-based polymer nanocomposites: research and commercial development," *Journal of nanoscience and nanotechnology*, vol. 5, no. 10, pp. 1574-1592, 2005.
- [38] A. Ainurofiq, "Application of Montmorillonite, Zeolite and Hydrotalcite Nanocomposite clays-drugs carrier of sustained release table dosage form," *Indonesian Journal of Pharmacy*, vol. 25, no. 3, pp. 125-131, 2014.
- [39] K. A. Carrado, "Synthetic organo-and polymer-clays: preparation, characterization, and materials applications," *Applied Clay Science*, vol. 17, no. 1, pp. 1-23, 2000.
- [40] W. A. Deer, R. A. Howie and J. Zussman, *Rock Forming Minerals: Layered Silicates Excluding Micas and Clay Minerals*, Geological Society of London, 2009.
- [41] M. Catalano, E. Belluso, D. Miriello, E. Barrese and A. Bloise, "Synthesis of Zn-doped talc in hydrothermal atmosphere," *Crystal Research and Technology*, vol. 49, no. 5, pp. 283-289, 2014.

- [42] O. Y. Golubeva, "Effect of synthesis conditions on hydrothermal crystallization, textural characteristics and morphology of aluminum-magnesium montmorillonite," *Microporous and Mesoporous Materials*, vol. 224, pp. 271-276, 2016.
- [43] S. Higashi, H. Miki and S. Komarneni, "Mn-smectites: Hydrothermal synthesis and characterization," *Applied Clay Science*, vol. 38, no. 1, pp. 104-112, 2007.
- [44] R. M. Davis, M. B. and C. Koch, "Mechanical alloying of brittle materials," *Metallurgical Transactions A*, vol. 19, no. 12, pp. 2867-2874, 1988.
- [45] J. Tronto, A. C. Bordonal, Z. Naal and J. B. Valim, "Conducting polymers/layered double hydroxides intercalated nanocomposites," in *Materials Science –Ad-*, InTech, 2013, pp. 3-30.
- [46] B. Nasiri-Tabrizi, A. Fahami and R. Ebrahimi-Kahrizsangi, "A comparative study of hydroxyapatite nanostructures produced under different milling conditions and thermal treatment of bovine bone," *Journal of Industrial and Engineering Chemistry*, vol. 20, no. 1, pp. 245-258, 2014.
- [47] Y. F. Gao, M. Nagai, Y. Masuda, F. Sato, W. S. Seo and K. Koumoto, "Surface precipitation of highly porous hydrotalcite-like film on Al from a zinc aqueous solution," *Langmuir*, vol. 22, no. 8, pp. 3521-3527, 2006.
- [48] J. T. Kloprogge, L. Hickey and R. L. Frost, "Heating stage Raman and infrared emission spectroscopic study of the dehydroxylation of synthetic Mg-hydrotalcite," *Applied Clay Science*, vol. 18, no. 1, pp. 37-49, 2001.

- [49] R. Wang and Z. Yang, "Synthesis and high cycle performance of Zn–Al–In-hydroxalcalite as anode materials for Ni–Zn secondary batteries," *Rsc Advances*, vol. 3, no. 43, pp. 19924-19928, 2013.
- [50] E. Landi, A. Tampieri, G. Celotti and S. Sprio, "Densification behaviour and mechanisms of synthetic hydroxyapatites," *Journal of the European Ceramic Society*, vol. 20, no. 14, pp. 2377-2387, 2000.
- [51] J. A. Stewart, B. M. Weckhuysen and P. C. Bruijninx, "Reusable Mg–Al hydroxalcalites for the catalytic synthesis of diglycerol dicarbonate from diglycerol and dimethyl carbonate," *Catalysis Today*, vol. 257, pp. 274-280, 2015.
- [52] Z. P. Xu, T. L. Walker, K. L. Liu, H. M. Cooper, G. M. Lu and P. F. Bartlett, "Layered double hydroxide nanoparticles as cellular delivery vectors of supercoiled plasmid DNA," *International journal of nanomedicine*, vol. 2, no. 2, pp. 163-174, 2007.
- [53] H. Acharya, S. K. Srivastava and A. K. Bhowmick, "Synthesis of partially exfoliated EPDM/LDH nanocomposites by solution intercalation: structural characterization and properties," *Composites Science and Technology*, vol. 67, no. 13, pp. 2807-2816, 2007.
- [54] W. Yang, Y. Kim, P. K. Liu, M. Sahimi and T. T. Tsotsis, "A study by in situ techniques of the thermal evolution of the structure of a Mg–Al–CO₃ layered double hydroxide," *Chemical Engineering Science*, vol. 57, no. 15, pp. 2945-2953, 2002.

- [55] F. L. Theiss, S. J. Palmer, G. A. Ayoko and R. L. Frost, "Sulfate intercalated layered double hydroxides prepared by the reformation effect," *Journal of thermal analysis and calorimetry*, 107(3), , vol. 107, no. 3, pp. 1123-1128, 2012.
- [56] Z. Luo, Y. Vasquez, J. F. Bondi and R. E. Schaak, "Pawley and Rietveld refinements using electron diffraction from L1 2-type intermetallic Au₃Fe_{1-x} nanocrystals during their in-situ order-disorder transition," *Ultramicroscopy*, vol. 111, no. 8, pp. 1295-1304, 2011.
- [57] A. Fahami and G. W. Beall, "Structural and morphological characterization of Mg_{0.8}Al_{0.2}(OH)₂Cl_{0.2} hydrocalcite produced by mechanochemistry method," *Journal of Solid State Chemistry*, vol. 233, pp. 422-427, 2016.
- [58] G. Qian, L. Feng, J. Z. Zhou, Y. Xu, J. Liu, J. Zhang and Z. P. Xu, "Solubility product (K_{sp})-controlled removal of chromate and phosphate by hydrocalumite," *Chemical Engineering Journal*, vol. 181, pp. 251-258, 2012.
- [59] M. Sánchez-Cantú, S. Camargo-Martínez, L. M. Pérez-Díaz, M. E. Hernández-Torres, E. Rubio-Rosas and J. S. Valente, "Innovative method for hydrocalumite-like compounds' preparation and their evaluation in the transesterification reaction," *Applied Clay Science*, vol. 114, pp. 509-516, 2015.
- [60] L. Kumar, P. Kumar, A. Narayan and M. Kar, "Rietveld analysis of XRD patterns of different sizes of nanocrystalline cobalt ferrite," *International Nano Letters*, vol. 3, no. 1, pp. 1-12, 2013.

- [61] N. G. Jović, A. S. Masadeh, A. S. Kremenovic, B. V. Antic, J. L. Blanuša, N. D. Cvjeticanin and E. S. Božin, "Effects of thermal annealing on structural and magnetic properties of lithium ferrite nanoparticles," *The Journal of Physical Chemistry C*, vol. 113, no. 48, pp. 20559-20567, 2009.
- [62] D. Brandon and W. D. Kaplan, *Microstructural characterization of materials*, John Wiley & Sons, 2013.
- [63] A. Fahami and G. W. Beall, "Mechanosynthesis and characterization of Hydrotalcite like Mg–Al–SO₄–LDH," *Materials Letters*, vol. 165, pp. 192-195, 2016.
- [64] A. Fahami, F. S. Al-Hazmi, A. A. Al-Ghamdi, W. E. Mahmoud and G. W. Beall, "Structural characterization of chlorine intercalated Mg-Al layered double hydroxides: A comparative study between mechanochemistry and hydrothermal methods," *Journal of Alloys and Compounds*, vol. 683, pp. 100-107, 2016.
- [65] M. Islam and R. Patel, "Physicochemical characterization and adsorption behavior of Ca/Al chloride hydrotalcite-like compound towards removal of nitrate," *Journal of hazardous materials*, vol. 190, no. 1, pp. 659-668, 2011.
- [66] P. Baláž, *Mechanochemistry in Nanoscience and Minerals Engineering*, Germany: Springer Berlin Heidelberg, 2008.
- [67] G. Mi, F. Saito and M. Hanada, "Mechanochemical synthesis of tobermorite by wet grinding in a planetary ball mill," *Powder Technology*, vol. 93, no. 1, pp. 77-81, 1997.

- [68] V. V. Boldyrev, "Hydrothermal reactions under mechanochemical action," *Powder Technology*, vol. 122, p. 247–254, 2002.
- [69] A. Dumas, F. Martin, E. Ferrage, P. Micoud, C. Le Roux and S. Petit, "Synthetic talc advances: Coming closer to nature, added value, and industrial requirements," *Applied Clay Science*, vol. 85, pp. 8-18, 2013.
- [70] F. Saito, G. Mi and M. Hanada, "Mechanochemical synthesis of hydrated calcium silicates by room temperature grinding," *Solid State Ionics*, vol. 101, pp. 37-43, 1997.
- [71] G. W. Brindley, *Crystal Structure of Clay Minerals and Their X Ray Identification: Order And Disorder in Clay Mineral Structures*, London: The Mineralogical Society, 1980.
- [72] A. Dumas, M. Claverie, C. Slostowski, G. Aubert, C. Careme, C. Le Roux, P. Micoud, F. Martin and C. Aymonier, "Fast-Geomimicking using Chemistry in Supercritical Water," *Angewandte Chemie*, vol. 128, no. 34, pp. 10022-10025, 2016.
- [73] F. Martin, S. Petit, O. Grauby and M. P. Lavie, "Gradual H/D substitution in synthetic germanium bearing talcs: a method for infrared band assignment," *Clay Minerals*, vol. 34, no. 2, pp. 365-374, 1999.
- [74] V. C. Farmer, "The infrared spectra of talc, saponite and hectorite," *Mineral. Mag.*, vol. 31, no. 241, pp. 829-845, 1958.

- [75] S. A. Parry, A. R. Pawley, R. L. Jones and S. M. Clark, "An infrared spectroscopic study of the OH stretching frequencies of talc and 10-Å phase to 10 GPa," *American Mineralogist*, vol. 92, no. 4, pp. 525-531, 2007.
- [76] J. Manna, B. Roy and P. Sharma, "Efficient hydrogen generation from sodium borohydride hydrolysis using silica sulfuric acid catalyst," *Journal of Power Sources*, vol. 275, pp. 727-733, 2015.
- [77] J. Wang and P. Somasundaran, "Adsorption and conformation of carboxymethyl cellulose at solid-liquid interfaces using spectroscopic, AFM and allied techniques," *Journal of Colloid and Interface Science*, vol. 291, no. 1, pp. 75-83, 2005.
- [78] B. Nasiri-Tabrizi and A. Fahami, "Mechanochemical synthesis and structural characterization of nano-sized amorphous tricalcium phosphate," *Ceramics International*, vol. 39, no. 8, pp. 8657-8666, 2013.
- [79] B. Fiorentino, R. Fulchiron, V. Bounor-Legaré, J. C. Majesté, J. C. Leblond and J. Duchet-Rumeau, "Chemical modification routes of synthetic talc: Influence on its nucleating power and on its dispersion state," *Applied Clay Science*, vol. 109, pp. 107-118, 2015.
- [80] C. Roosz, S. Grangeon, P. Blanc, V. Montouillout, B. Lothenbach, P. Henocq, E. Giffaut, P. Vieillard and S. Gaboreau, "Crystal structure of magnesium silicate hydrates (MSH): The relation with 2: 1 Mg-Si phyllosilicates," *Cement and Concrete Research*, vol. 73, pp. 228-237, 2015.

- [81] A. Dumas, F. Martin, C. Le Roux, P. Micoud, S. Petit, E. Ferrage and M. Greenhill-Hooper, "Phyllosilicates synthesis: a way of accessing edges contributions in NMR and FTIR spectroscopies. Example of synthetic talc," *Physics and Chemistry of Minerals*, vol. 40, no. 4, pp. 361-373, 2013.
- [82] V. Balek, J. Šubrt, L. A. Pérez-Maqueda, M. Beneš, I. M. Bountseva, I. N. Beckman and J. L. Pérez-Rodríguez, "Thermal behavior of ground talc mineral," *Journal of Mining and Metallurgy B: Metallurgy*, vol. 44, no. 1, pp. 7-17, 2008.
- [83] K. Chabrol, M. Gressier, N. Pebere, M. J. Menu, F. Martin, J. P. Bonino and J. Brendle, "Functionalization of synthetic talc-like phyllosilicates by alkoxyorganosilane grafting," *Journal of Materials Chemistry*, vol. 20, no. 43, pp. 9695-9706, 2010.
- [84] F. J. Huertas, S. Fiore, F. Huertas and J. Linares, "Experimental study of the hydrothermal formation of kaolinite," *Chemical Geology*, vol. 156, no. 1, pp. 171-190, 1999.
- [85] G. J. Churchman, J. S. Whitton, G. G. C. Claridge and B. K. G. Theng, "Intercalation method using formamide for differentiating halloysite from kaolinite," *Clays and Clay Minerals*, vol. 32, no. 4, pp. 241-248, 1984.
- [86] M. J. Wilson, "Clay mineralogical and related characteristics of geophagic materials," *Journal of chemical ecology*, vol. 29, no. 7, pp. 1525-1547, 2003.
- [87] C. I. Fialips, A. Navrotsky and S. Petit, "Crystal properties and energetics of synthetic kaolinite," *American Mineralogist*, 86(3), , vol. 86, no. 3, pp. 304-311, 2001.

- [88] R. Miyawaki, S. Tomura, S. Samejima, M. Okazaki, H. Mizuta, M. S-I and Y. Shibasaki, "Effects of solution chemistry on the hydrothermal synthesis of kaolinite," *Clays and Clay Minerals*, vol. 39, no. 5, pp. 498-508, 1991.
- [89] E. Joussein, S. Petit, J. Churchman, B. Theng, D. Righi and B. Delvaux, "Halloysite clay minerals—a review," *Clay minerals*, vol. 40, no. 4, pp. 383-426, 2005.
- [90] R. L. Frost, "The structure of the kaolinite minerals— a FT-Raman study," *Clay Minerals*, vol. 32, no. 1, pp. 65-77, 1997.
- [91] R. G. Wolff, "Structural aspects of kaolinite using infrared absorption," *American Mineralogist*, vol. 48, no. 3-4, pp. 390-399, 1963.
- [92] U. O. Aroke, A. Abdulkarim and R. O. Ogubunka, "Fourier-transform infrared characterization of kaolin, granite, bentonite and barite," *ATBU Journal of Environmental Technology*, vol. 6, no. 1, pp. 42-53, 2013.
- [93] B. J. Saikia and G. Parthasarathy, "Fourier transform infrared spectroscopic characterization of kaolinite from Assam and Meghalaya, Northeastern India," *Journal of Modern Physics*, vol. 1, no. 40, p. 206, 2010.
- [94] G. Li, J. Zeng, J. Luo, M. Liu, T. Jiang and G. Qiu, "Thermal transformation of pyrophyllite and alkali dissolution behavior of silicon," *Applied Clay Science*, vol. 99, pp. 282-288, 2014.
- [95] S. Letaief, J. Leclercq, Y. Liu and C. Detellier, "Single kaolinite nanometer layers prepared by an in situ polymerization—exfoliation process in the presence of ionic liquids," *Langmuir*, vol. 27, no. 24, pp. 15248-15254, 2011.

- [96] S. Fiore, F. J. Huertas, F. Huertas and J. Linares, "Morphology of kaolinite crystals synthesized under hydrothermal conditions," *Clays and Clay Minerals*, vol. 43, no. 3, pp. 353-360, 1995.
- [97] J. Matusik, "Halloysite-like Structure via Delamination of Kaolinit," in *Nanosized Tubular Clay Minerals*, 2016, pp. 409-428.
- [98] B. Ghouil, A. Harabi, F. Bouzerara, B. Boudaira, A. Guechi, M. M. Demir and A. Figoli, "Development and characterization of tubular composite ceramic membranes using natural aluminosilicates for microfiltration applications," *Materials Characterization*, vol. 103, pp. 18-27, 2015.
- [99] Ö. I. Ece, B. Ekinçi, P. A. Schroeder, D. Crowe and F. Esenli, "Origin of the Düvertepe kaolin-alunite deposits in Simav Graben, Turkey: Timing and styles of hydrothermal mineralization," *Journal of Volcanology and Geothermal Research*, vol. 255, pp. 57-78, 2013.
- [100] K. A. A. Hadi, "The genesis and characteristics of primary kaolinitic clay occurrence at Bukit Lampas, Simpang Pulai, Ipoh," *Bulletin of the Geological Society of Malaysia*, vol. 54, pp. 9-16, 2008.
- [101] M. X. Reinholdt, J. Brendlé, M. H. Tuilier, S. Kaliaguine and E. Ambroise, "Hydrothermal synthesis and characterization of Ni-Al montmorillonite-like phyllosilicates," *Nanomaterials*, vol. 3, no. 1, pp. 48-69, 2013.
- [102] O. Prieto, M. A. Vicente and M. A. Bañares-Muñoz, "Study of the Porous Solids Obtained by Acid Treatment of a High Surface Area Saponite," *Journal of Porous Materials*, vol. 6, no. 4, pp. 335-344, 1999.

- [103] C. Bisio, G. Gatti, E. Boccaleri, L. Marchese, G. B. Superti, H. O. Pastore and M. Thommes, "Understanding physico–chemical properties of saponite synthetic clays," *Microporous and Mesoporous Materials*, vol. 107, no. 1, pp. 90-101, 2008.
- [104] A. R. Ramadan, A. M. Esawi and A. A. Gawad, "Effect of ball milling on the structure of Na⁺-montmorillonite and organo-montmorillonite (Cloisite 30B)," *Applied Clay Science*, vol. 47, no. 3, pp. 196-202, 2010.
- [105] C. Li, J. Zhang, Y. Lin, Y. Chen, X. Xie, H. Wang and L. Wang, "In situ growth of layered double hydroxide on disordered platelets of montmorillonite," *Applied Clay Science*, vol. 119, pp. 103-108, 2016.
- [106] N. Kalaivasan and S. S. Shafi, "Enhancement of corrosion protection effect in mechanochemically synthesized Polyaniline/MMT clay nanocomposites," *Arabian Journal of Chemistry*, vol. 10, no. 1, pp. 127-133, 2017.
- [107] H. V. Hoang, "Electrochemical Synthesis of Novel Polyaniline-Montmorillonite Nanocomposites and Corrosion Protection of Steel," Chemnitz University of Technology, 2006.
- [108] I. Bekri-Abbes and E. Srasra, "Effect of mechanochemical treatment on structure and electrical properties of montmorillonite," *Journal of Alloys and Compounds*, vol. 671, pp. 34-42, 2016.
- [109] L. Bailey, H. N. Lekkerkerker and G. C. Maitland, "Smectite clay–inorganic nanoparticle mixed suspensions: phase behaviour and rheology," *Soft Matter*, vol. 11, no. 2, pp. 222-236, 2015.

- [110] D. Chen, J. Zhu, P. Yuan, S. Yang, T. Chen and H. He, "Preparation and characterization of anion-cation surfactants modified montmorillonite. Journal of Thermal Analysis and Calorimetry," *Journal of Thermal Analysis and Calorimetry*, vol. 94, no. 3, pp. 841-848, 2008.
- [111] M. Xia, Y. Jiang, L. Zhao, F. Li, B. Xue, M. Sun and X. Zhang, "Wet grinding of montmorillonite and its effect on the properties of mesoporous montmorillonite," *Colloids and Surfaces A: Physicochemical and Engineering Aspects*, vol. 356, no. 1, pp. 1-9, 2010.
- [112] K. A. Carrado, P. Thiyagarajan and K. Song, "A study of organo-hectorite clay crystallization," *Clay Minerals*, 32(1), 29-40, vol. 32, no. 1, pp. 29-40, 1997.
- [113] X. Zhang, G. Dou, Z. Wang, J. Cheng, H. Wang, C. Ma and Z. Hao, "Selective oxidation of H₂S over V₂O₅ supported on CeO₂-intercalated Laponite clay catalysts," *Catalysis Science & Technology*, vol. 3, no. 10, pp. 2778-2785, 2013.
- [114] C. S. Jun, B. Sim and H. J. Choi, "Fabrication of electric-stimuli responsive polyaniline/laponite composite and its viscoelastic and dielectric characteristics," *Colloids and Surfaces A: Physicochemical and Engineering Aspects*, vol. 482, pp. 670-677, 2015.
- [115] R. R. Pawar, H. A. Patel, G. Sethia and H. C. Bajaj, "Selective adsorption of carbon dioxide over nitrogen on calcined synthetic hectorites with tailor-made porosity," *Applied Clay Science*, vol. 46, no. 1, pp. 109-113, 2009.

- [116] P. K. Paul, S. A. Hussain, D. Bhattacharjee and M. Pal, "Preparation of polystyrene–clay nanocomposite by solution intercalation technique," *Bulletin of Materials Science*, vol. 36, no. 3, pp. 361-366, 2013.
- [117] F. F. Fang, J. H. Kim, H. J. Choi and C. Am Kim, "Synthesis and electrorheological response of nano-sized laponite stabilized poly(methyl methacrylate) spheres," *Colloid and Polymer Science*, vol. 287, no. 6, pp. 745-749, 2009.
- [118] R. A. Da Silva and D. J. Guerra, " Use of natural and modified kaolinite/ilite as adsorbent for removal methylene blue dye from aqueous solution," *ournal of the Chilean Chemical Society*, vol. 58, no. 1, pp. 1517-1519, 2013.
- [119] S. J. Parikh, K. W. Goynes, A. J. Margenot, F. N. Mukome and F. J. Calderón, "Soil Chemical Insights Provided through Vibrational Spectroscopy," in *Advances in Agronomy*, 2014, pp. 1-148.
- [120] A. J. Blanch, J. S. Quinton, C. E. Lenehan and A. Pring, "The crystal chemistry of Al-bearing goethites: an infrared spectroscopic study," in *Mineralogical Magazine*, 72, 5, 2008, pp. 1043-1056.
- [121] T. Sánchez, P. Salagre and Y. Cesteros, "Ultrasounds and microwave-assisted synthesis of mesoporous hectorites," *Microporous and Mesoporous Materials*, vol. 171, pp. 24-34, 2013.
- [122] C. H. Zhou, D. Tong and X. Li, "Synthetic hectorite: preparation, pillaring and applications in catalysis," in *Pillared clays and related catalysts*, New York, Springer, 2010, pp. 67-97.

- [123] R. R. Pawar, B. D. Kevadiya, H. Brahmhatt and H. C. Bajaj, "Template free synthesis of mesoporous hectorites: Efficient host for pH responsive drug delivery," *International journal of pharmaceutics*, vol. 446, no. 1, pp. 145-152, 2013.
- [124] D. Kleshchanok, V. Meester, C. E. Pompe, J. Hilhorst and H. N. Lekkerkerker, "Effects of Added Silica Nanoparticles on Hectorite Gel," *The Journal of Physical Chemistry B*, vol. 116, no. 31, pp. 9532-9539, 2012.
- [125] N. N. Herrera, J. M. Letoffe, J. L. Putaux, L. David and E. Bourgeat-Lami, "Aqueous dispersions of silane-functionalized laponite clay platelets. A first step toward the elaboration of water-based polymer/clay nanocomposites," *Langmuir*, vol. 20, no. 5, pp. 1564-1571, 2004.
- [126] A. Giannakas, A. Giannakas and A. Ladavos, "Preparation and characterization of polystyrene/organolaponite nanocomposites," *Polymer-Plastics Technology and Engineering*, vol. 51, no. 14, pp. 1411-1415, 2012.
- [127] K. A. Carrado, R. Csencsits, P. Thiyagarajan, S. Seifert, S. M. Macha and J. S. Harwood, "Crystallization and textural porosity of synthetic clay minerals," *Journal of Materials Chemistry*, vol. 12, no. 11, pp. 3228-3237, 2002.
- [128] J. L. Suter, P. V. Coveney, H. C. Greenwell and M. A. Thyveetil, "Large-scale molecular dynamics study of montmorillonite clay: emergence of undulatory fluctuations and determination of material properties," *The Journal of Physical Chemistry C*, vol. 111, no. 3, pp. 8248-8259, 2007.

- [129] O. P. Bricker, H. W. Nesbitt and W. D. Gunter, "The Stability of Talc," *American Mineralogist*, vol. 58, pp. 64-72, 1973.
- [130] B. S. Hemingway, "Thermodynamic properties of anthophyllite and talc: corrections and discussion of calorimetric data," *American Mineralogist*, vol. 76, no. 9-10, pp. 1589-1596, 1991.
- [131] E. A. Zen, "Correlated free energy values of anthophyllite, brucite, clinochrysotile, enstatite, forsterite, quartz, and talc," *American Mineralogist*, vol. 61, pp. 1156-1166, 1976.
- [132] Y. Tardy and J. Duplay, "A method of estimating the Gibbs free energies of formation of hydrated and dehydrated clay minerals," *Geochimica et Cosmochimica Acta*, vol. 56, no. 8, pp. 3007-3029, 1992.